Study of strongly correlated spin systems using density matrix embedding theory

Klaas Gunst

Supervisor: Prof. dr. Dimitri Van Neck
Counsellors: Dr. ir. Sebastian Wouters, Ir. Pieter Claeys, Dr. Stijn De Baerdemacker

Master's dissertation submitted in order to obtain the academic degree of
Master of Science in Engineering Physics

Vakgroep Fysica en Sterrenkunde
Chair: Prof. dr. Dirk Ryckbosch
Faculty of Engineering and Architecture
Academic year 2015-2016

UNIVERSITEIT GENT

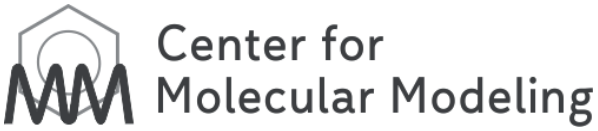

This research was conducted at the Center for Molecular Modeling.

Preface

Almost five years have passed since my first steps in the Plateau and the start of my education in physical engineering. During this period, I had, like many, moments of doubt about my study choices, but time after time interesting courses reassured me of the path I had chosen. During my education I got a particular interest in quantum mechanics. This motivated me to choose a thesis at the CMM under supervision of prof. dr. Dimitri Van Neck.

My thesis has proven to be a satisfying closure to my time as student at the UGent. The experience of a great thesis-time is of course only possible in a stimulating and relaxed environment, an environment that has been provided by the CMM and all its members for which I am grateful. Special thanks goes to my supervisor prof. dr. Dimitri Van Neck for giving me the opportunity to be part of his group and for his insightful remarks concerning my thesis. I thank also my councillors, Sebastian, Pieter and Stijn. Their remarks and revisions have been a great help for me. I especially thank Sebastian and Pieter for accepting me in their office this past year. Sebastian's expertise regarding DMET has aided me a lot and without his numerous tips for the efficient implementation of a DMET code my thesis would have been dominated with the endless waiting for results. On the other hand, Pieter's knowledge on quantum spin systems has been of great use while doing my literature study. I would also like to thank my fellow thesis-students, with whom I shared many laughs: Michiel, Yentl, Senne, Titus and Pieter.

Finally, I would like to thank my parents. Their everlasting support has helped me through the past years. Although I do not always show it, I am very grateful for this.

Klaas Gunst

Klaas Gunst

Ghent, June 1st 2016

Study of strongly correlated spin systems using density matrix embedding theory

Klaas Gunst

Supervisors: prof. dr. Dimitri Van Neck
Counsellors: dr. ir. Sebastian Wouters, ir. Pieter Claeys,
dr. Stijn De Baerdemacker

Master's dissertation submitted in order to obtain the academic degree of
Master of Science in Physical Engineering

Faculty of Engineering and Architecture – Ghent University
Center for Molecular Modeling
Academic year 2015–2016

Abstract

Although spin Hamiltonians are easy in their formulation, their behaviour can be all but trivial and numerous phases and phase transitions can occur. Spin systems are not only interesting for the emerging physics, but also for their use in quantum computing. However, the exponential scaling of the Hilbert space with system size makes the exact solution of the quantum many-body problem infeasible quickly and approximate methods are needed.

Density matrix embedding theory (DMET) is a relatively new technique for the calculation of strongly correlated systems. For this thesis, an adapted version of DMET for spin systems, the so-called cluster DMET, will be implemented and used for the study of multiple spin systems. First, the antiferromagnetic $J_1 - J_2$ model on the square lattice, which is one of the most studied models for frustration effects, will be investigated. The anisotropic Kitaev-Heisenberg model on the honeycomb lattice will also be studied through cluster DMET calculations and exact diagonalization.

A method for the calculation of spectral functions within the DMET framework has also been proposed and has been implemented. Future optimisation of the implementation will allow for the efficient calculation in larger spin systems.

Keywords: DMET, spin systems, frustration, embedding.

Study of strongly correlated spin systems using density matrix embedding theory

Klaas Gunst
Supervisor: prof. dr. Dimitri Van Neck
Counsellors: dr. ir. Sebastian Wouters, ir. Pieter Claeys, dr. Stijn De Baerdemacker

Abstract. **Density matrix embedding theory (DMET) is a relatively new technique for the calculation of strongly correlated systems. Here cluster DMET will be used for the study of spin systems such as the antiferromagnetic $J_1 - J_2$ model on the square lattice and the Kitaev-Heisenberg model on the honeycomb lattice.**

Keywords. **DMET, spin systems, frustration, embedding.**

I. Introduction

Although spin Hamiltonians are easily formulated, their behaviour can be all but trivial and numerous phases and phase transitions may occur. Spin Hamiltonians are however not only popular due to their interesting physics. The development of quantum computing has given rise to an increasing interest in spin systems. Their study is needed for many facets of quantum computing like *quantum error correction* and *topological quantum computing*.

A problem of the solution of spin systems, and many-body systems more generally, is the exponential growth of the Hilbert space with system size. Due to this unfavourable growth, the computational cost of exact diagonalization also scales exponentially. One widely investigated spin system is the $J_1 - J_2$ model on the square lattice with spin-$\frac{1}{2}$. This model has nearest neighbour (NN) and next-nearest neighbour (NNN) interactions. Exact diagonalization has been performed on a lattice up to 40 spins for this model [1]. A square lattice of 40 spins is not large enough yet for description of the bulk, as finite size effects are still present in the system. To describe the bulk better we would need to move on to larger systems. To make the description of these systems feasible, approximate methods are needed.

Recently, density matrix embedding theory (DMET) has been introduced by Knizia *et al.* [2] to solve the Hubbard model in an approximate manner. It has later also been extended to full chemical Hamiltonians [3]. For ground state energies, DMET has proven itself as a computationally cheap method with good accuracy [2, 3]. The main idea behind this method consists of splitting the total Hilbert space into two parts, an *impurity*, and an *environment*. Schmidt decomposition of an arbitrary state is of the form

$$|\Psi\rangle = \sum_{k}^{\min(N,M)} \lambda_k |\alpha_k\rangle |\beta_k\rangle , \qquad (1)$$

where $|\alpha_k\rangle$ and $|\beta_k\rangle$ are states of the impurity and environment, respectively. N and M are the dimensions of the Hilbert spaces restricted to impurity and environment, respectively. Since the impurity is typically chosen smaller than the environment, the summation is restricted to N terms. Only N states in the environment are needed to construct an arbitrary wave function. If only one singular value λ_k is nonzero, the impurity and environment are unentangled. If multiple singular values are nonzero, they are entangled. Finding the ground state is very easy if the Schmidt basis $\{|\alpha_k\rangle , |\beta_k\rangle\}$ of the impurity and environment are known. However, the Schmidt basis for the environment can only be found through a priori knowledge of the exact ground state. DMET solves this problem by embedding the

impurity A in an approximate bath B. Solving this combined impurity and bath system is called the embedded problem. Different techniques can be used to find the bath space. A Fock space of bath orbitals, which is obtained from a low-level particle-number conserving mean-field wave function, is used in the original refs. [2] and [3]. In this thesis, we will use the representation of bath states in a spin lattice system by block-product states as introduced by Fan *et al.* [4], the so-called cluster DMET method.

II. Cluster DMET

When using the cluster DMET method [4], the bath states are approximated by block-product states $\left|\beta_i^{\text{BPS}}\right\rangle$. With this approximation the wave function of the model becomes

$$|\Psi\rangle_{\text{imp}} = \sum_i a_i \left|\alpha_i\right\rangle \left|\beta_i^{\text{BPS}}\right\rangle . \tag{2}$$

To define these block-product states, we first divide the spin lattice system in different equivalent clusters. We then pick one of these clusters as the impurity. The other clusters are called the bath clusters. With this division of the lattice system, the block-product states can be defined as follows:

$$\left|\beta_i^{\text{BPS}}\right\rangle = \bigotimes_{C\in\text{bath clusters}} \sum_\beta b_{C\beta}^i \left|\beta\right\rangle_C . \tag{3}$$

Here $\{|\beta\rangle_C\}$ is a complete set of states within the Hilbert space restricted to the bath cluster C. For example, if each bath cluster is contains 3 spins with $S = \frac{1}{2}$, we have $\{|\downarrow\downarrow\downarrow\rangle, |\downarrow\downarrow\uparrow\rangle, |\downarrow\uparrow\downarrow\rangle, .., |\uparrow\uparrow\uparrow\rangle\}$.
Optimization of these block-product states is now needed so that Eq. (2) optimally represents the exact ground state. The energy of the wave function in the impurity, i.e. $E_{\text{imp}} = \langle\Psi|\hat{H}|\Psi\rangle_{\text{imp}} \,/\, \langle\Psi|\Psi\rangle_{\text{imp}}$, is minimized iteratively. In every iteration, the optimization happens in a restricted Hilbert space given by the $\{|\phi_\alpha\rangle, |\phi_\beta\rangle\}$-basis with

$$|\phi_{\alpha_i}\rangle = |\alpha_i\rangle \bigotimes_C \sum_\beta b_{C\beta}^i \left|\beta\right\rangle_C ,$$
$$\left|\phi_\beta\right\rangle = \left|\alpha_{i_0}\right\rangle \left|\beta\right\rangle_{B_0} \bigotimes_{C\neq B_0} \sum_{\beta'} b_{C\beta}^{i_0} \left|\beta'\right\rangle_C .$$

The parameters to optimize in every iteration are a_i with $i \neq i_0$ and $a_{i_0} b_{B_0\beta}^{i_0}$. By looping over the different i_0's and B_0's, i.e. the different impurity states and bath clusters, the cluster DMET-ansatz is optimized. The algorithm is guaranteed to converge to a (possibly local) minimum.

III. $J_1 - J_2$ model on the square lattice

A first system under study is the $J_1 - J_2$ model on the square lattice; this model has NN and NNN interactions. The Heisenberg Hamiltonian of this model is given by

$$\hat{H} = J_1 \sum_{\langle i,j\rangle} \hat{\mathbf{S}}_i \cdot \hat{\mathbf{S}}_j + J_2 \sum_{\langle\langle i,k\rangle\rangle} \hat{\mathbf{S}}_i \cdot \hat{\mathbf{S}}_k \tag{4}$$

with J_1, $J_2 \leq 0$ and where $\langle i,j\rangle$ sums over the nearest neighbours and $\langle\langle i,k\rangle\rangle$ sums over the next-nearest neighbours.
It is widely accepted that this model has three different phases. At low J_2/J_1, a Néel antiferromagnetic (AF) phase with long-range order (LRO) is observed, while at high J_2/J_1, the system is in a collinear phase with LRO. At intermediate J_2/J_1 a disordered nonmagnetic phase is found. The exact nature of the nonmagnetic phase is still under discussion. Spin-spin correlations are not short-range enough to effectively represent the bulk at the current attainable system sizes, hence hindering the examination of the phase in the bulk [5]. Possible candidates for the intermediate nonmagnetic phase are the columnar and staggered dimer valence-bond crystals (VBC), the plaquette resonating valence bond (RVB) and the gapped Z_2 spin liquid. The phase transitions are expected at $J_2/J_1 \approx 0.4$ and $J_2/J_1 \approx 0.6$.
Cluster DMET is executed on a 8×8 square lattice. The lattice is divided into 16 equal

2×2 clusters. When executing the DMET algorithm with random initialisation, it is found that the algorithm converges quite consistently to the same minimum in the LRO phases. However, in the nonmagnetic phase, random initialisation converges to a wide variety of different local minima. To overcome this problem *sweeps* are performed within the J_2/J_1 parameter space (i.e. the converged result for the previous parameter value is used as initial guess for the next parameter value). The results are shown in figures 1 and 2.

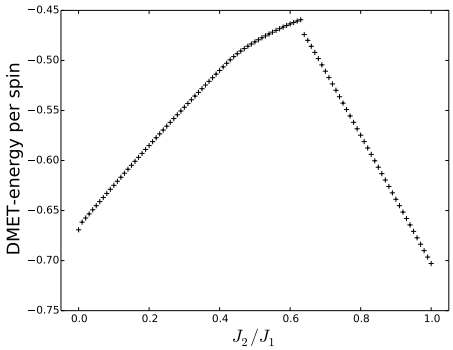

Figure 1: DMET-energy per spin for the 8×8 square lattice.

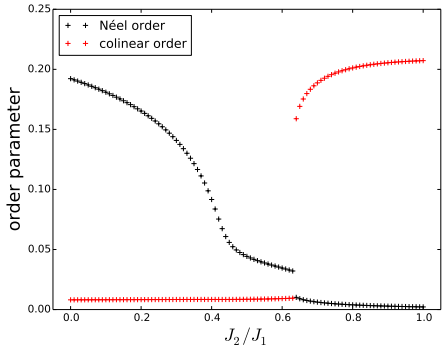

Figure 2: Order parameters for the 8×8 square lattice.

These DMET results are comparable with results obtained from other methods. There is clearly a Néel AF LRO phase detected at J_2/J_1 and a colinear LRO phase at high J_2/J_1. An intermediate phase between $J_2/J_1 \approx 0.4$ and $J_2/J_1 \approx 0.6$ is observed where the order parameters vanish or noticeably diminish. The fact that the Néel order parameter does not completely vanish in the intermediate phase can be attributed to finite size effects. Different entanglement entropies have also been calculated and the nature of this intermediate phase can be investigated further. The entanglement entropies suggest a conservation of the C_4-symmetry. This is strong evidence against the occurrence of a symmetry breaking dimer VBC phase. Furthermore, some weak evidence is found in favour of a weak plaquette RVB.

IV. The Kitaev-Heisenberg model on the honeycomb lattice

The Kitaev-Heisenberg model is built up by mixing the Kitaev and the Heisenberg model, as the name suggests, and was originally introduced in ref. [6]. The Hamiltonian for this system on the honeycomb lattice is given by

$$\begin{aligned}\hat{H} = &- J_1 \sum_{x-\text{links}} \hat{S}_j^x \hat{S}_k^x - J_1 \sum_{y-\text{links}} \hat{S}_j^y \hat{S}_k^y \\ &- J_1 \sum_{z-\text{links}} \hat{S}_j^z \hat{S}_k^z + J_2 \sum_{\langle jk \rangle} \hat{\mathbf{S}}_j \cdot \hat{\mathbf{S}}_k.\end{aligned} \tag{5}$$

The first part of the Hamiltonian is the Kitaev interaction, which is anisotropic, while the last term encompasses the Heisenberg interaction. Which bonds are exactly x-links, y-links or z-links is sketched in figure 3. The Kitaev interaction and the Heisenberg interaction are parametrized as $J_1 = 2\alpha$ and $J_2 = 1 - \alpha$. In the interval $\alpha \in [0, 1]$ three phases can be distinguished. At low α a Néel AF phase is observed, at intermediate α a stripy AF phase, and at high α a quantum spin liquid is observed. At the intermediate point, $\alpha = 0.5$, the system is exactly solvable through the use of a rotated basis. Exact diagonalization and second order perturbation theory suggest phase transitions at $\alpha \approx 0.4$ and $\alpha \approx 0.8$. A series expansion suggest that the phase transition between the two AF phases happens at $\alpha \approx \frac{1}{3}$ [7]. Exact diagonalization on the 24 spin honeycomb lattice is

performed and has been used as a benchmark for the cluster DMET calculations.

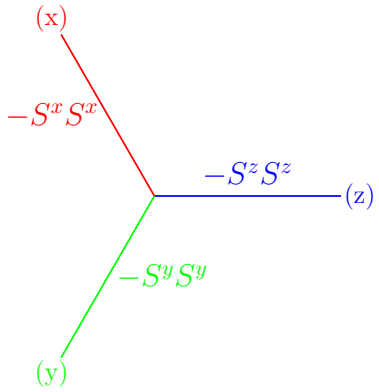

Figure 3: The different bond types in the honeycomb lattice for the Kitaev model.

The cluster-DMET algorithm is executed with different cluster types, the S-shaped and star-shaped clusters, which have 4 spins per cluster, and the hexagonal cluster which has 6 spins. Random initialisation of the DMET-algorithm has a consistent convergence in the AF phase; however, in the spin liquid phase, convergence happens to a wide variety of local minima. A sweep is again used to obtain results for the spin liquid, ensuring easily reproducible results.
When comparing the DMET results of the 24 spin system with the exact diagonalization of the 24 spin system, a clear difference is noted between the use of different clusters. All clusters describe the two AF phases fairly well. However, the S-shaped cluster does not show a phase transition towards the spin liquid. When using the star-shaped cluster a phase transition occurs at $\alpha \approx 0.8$. Although the phase transition to the spin liquid is observed, the spin liquid itself is poorly described through cluster DMET. Since the proposed DMET-ansatz can describe a larger corner of the Hilbert space with increasing cluster size, it is expected that the hexagonal cluster performs better than the 4-spin clusters. When using the hexagonal cluster, the phase transition towards a spin liquid is detected and the obtained properties of the

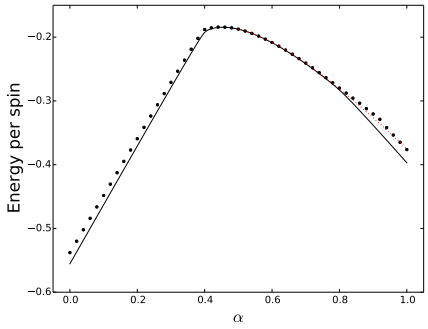

Figure 4: DMET-energy per spin for the 24 spin honeycomb lattice solved with the use of hexagonal clusters.

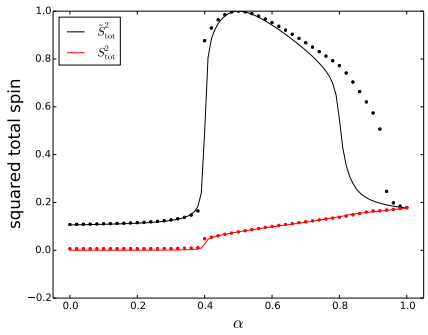

Figure 5: Squared total spin in the original and rotated basis for the 24 spin honeycomb lattice solved with the use of hexagonal clusters.

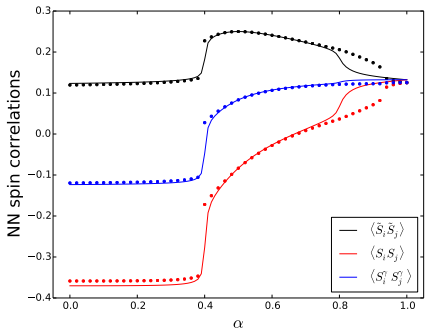

Figure 6: NN correlations for the 24 spin honeycomb lattice solved with the use of hexagonal clusters.

spin liquid are in good correspondence with the exact diagonalization. However, the phase transition happens at $\alpha \approx 0.92$, which is not the right value. The behaviour of the squared total spin in the rotated basis and of the entanglement entropy at $\alpha \approx 0.8$ are light indications of a phase transition, but the phase transition is clearly delayed to a further point. Results for the energy per spin and the different properties are given in figures 4, 5 and 6. Full lines are results obtained from exact diagonalization while the dots represent results from cluster DMET with the hexagonal cluster.

To calculate bulk properties of the Kitaev-Heisenberg model, the 96 spin honeycomb lattice is also calculated with cluster DMET, using the star shaped and the hexagonal cluster. Only small corrections to the properties and energies are found and no shifts of the phase boundaries are noticed. This is an indication that the finite size effects are already small at the 24 spin lattice and this lattice already represents bulk quite well. Furthermore, since no shift of the phase boundaries is obtained through the enlargement of the system, this is evidence in favour of a phase shift at $\alpha \approx 0.4$ and not at $\alpha \approx \frac{1}{3}$ as suggested by ref. [7].

V. Conclusion

We have implemented an efficient cluster DMET algorithm and a method for calculating properties is suggested and used to find the order parameters, DMET-energy per spin, squared total spin and NN correlations. Also a method for the calculation of the spectral function is given within the cluster DMET framework. A code has been implemented, however further optimisation is needed at this point for the efficient calculation of spectral functions in reasonably large spin systems.

The cluster DMET algorithm has been used to reproduce the results obtained in ref. [4] for the J_1/J_2 model on the square lattice. The correct LRO phases are detected in the square lattice with NN and NNN interactions, and evidence is found for the occurrence of a plaquette RVB in the intermediate region.

Furthermore, the Kitaev-Heisenberg model on the honeycomb lattice is also investigated through cluster DMET calculations and benchmarked with exact results for the 24 spin lattice. Good correspondence is found at the Néel and the stripy AF phases. For the spin liquid phase only the hexagonal cluster gives adequate results; however, the phase transition is detected at the wrong point. A larger 96 spin honeycomb lattice was also studied through DMET. The scaling effects are minor, which make us conclude that the 24 spin system is already quite successful in the description of the bulk.

Acknowledgements

This work was performed at the Center for Molecular Modeling (CMM) under the supervision of prof. dr. Dimitri Van Neck and the counselling of dr. ir. Sebastian Wouters, ir. Pieter Claeys and dr. Stijn De Baerdemacker. I wish to thank them for their support and guidance. I also would like to thank the other members of the CMM for their support. The computational resources and services used were provided by Ghent University (Stevin Supercomputer Infrastructure).

References

[1] J. Richter, J. Schulenburg The spin-1/2 J1-J2 Heisenberg antiferromagnet on the square lattice: Exact diagonalization for $N = 40$ spins. *The European Physical Journal B*, 73.1 (2009) 117-124

[2] G. Knizia, G.K.-L. Chan Density Matrix Embedding: A Simple Alternative to Dynamical Mean-Field Theory. *Phys. Rev. Lett.*, 109 (2012) 186404

[3] G. Knizia, G.K.-L. Chan Density Matrix Embedding: A Strong-Coupling Quantum Embedding Theory *Journal of Chemical Theory and Computation* 9.3 (2013) 1428-1432

[4] Z. Fan, Q.-L. Jie Cluster density matrix embedding theory for quantum spin systems *Phys. Rev. B* 91 (2015) 195118

[5] G. Misguich, C. Lhuillier Two-dimensional quantum antiferromagnets *eprint arXiv:cond-mat/0310405* (2003)

[6] J. Chaloupka, G. Jackeli, G. Khaliullin Kitaev-Heisenberg Model on a Honeycomb Lattice: Possible Exotic Phases in Iridium Oxides A_2IrO_3 *Physical Review Letters* 105.2 (2010) 027204

[7] J. Oitmaa Phase diagram of the Heisenberg-Kitaev model at $T = 0$. *Phys. Rev. B* 92 (2015) 020405

Contents

List of abbreviations

AF	Antiferromagnetic
AGP	Anti-symmetrized geminal power
CCM	Coupled cluster method
DMET	Density matrix embedding theory
DMFT	Dynamical mean-field theory
DMRG	Density matrix renormalization group
ED	Exact diagonalization
HMF	Hierarchical mean-field
LRO	Long-range order
MPS	Matrix product states
NN	Nearest neighbour
NNN	Next-nearest neighbour
PEPS	Projected entangled pair states
QP	Quantum paramagnetic
QSL	Quantum spin liquid
RVB	Resonating valence bond
SRVB	short-range valence bond states
VBC	Valence-bond crystals

1 Introduction

The biggest problem with the study of many-body systems is that obtaining an exact solution becomes infeasible for large system sizes. The dimension of the Hilbert space scales exponentially with the number of particles. This inhibits the exact simulation of bigger systems and approximate methods have to be used.
Suppose one is only interested in a small part of the whole system. This part can be a specific region in space, but any other division of the total Hilbert space of the system into subspaces is also possible. By dividing the total system into two parts, an *impurity*, *cluster* or *fragment* (which is the subsystem of interest) and an *environment*, one can use embedding theories to solve the problem approximately. The total Hilbert space of the system is now a direct product of the Hilbert spaces of the impurity and environment. A basis for this Hilbert space is given by $\{|\alpha_i\rangle \otimes |\beta_j\rangle\}$, where $|\alpha_i\rangle$ are states of the impurity and $|\beta_j\rangle$ are states restricted to the environment. Every state $|\Psi\rangle$ can be written as

$$\begin{aligned} |\Psi\rangle &= \sum_{i}^{N}\sum_{j}^{M} \Psi_{ij} |\alpha_i\rangle |\beta_j\rangle \\ &= \sum_{i}^{N}\sum_{j}^{M}\sum_{k}^{\min(N,M)} U_{ik}\lambda_k V_{kj}^{\dagger} |\alpha_i\rangle |\beta_j\rangle \\ &= \sum_{k}^{\min(N,M)} \lambda_k \left(\sum_{i}^{N} U_{ik} |\alpha_i\rangle\right)\left(\sum_{j}^{M} V_{kj}^{\dagger} |\beta_j\rangle\right) \\ &= \sum_{k}^{\min(N,M)} \lambda_k |\widetilde{\alpha}_k\rangle \, |\widetilde{\beta}_k\rangle \, . \end{aligned} \tag{1.1}$$

This is called the Schmidt decomposition of a state. Here $|\widetilde{\alpha}_i\rangle$ are states of the impurity and $|\widetilde{\beta}_i\rangle$ are states of the environment. As can be seen in the Schmidt decomposition, the summation goes over the minimum dimension of impurity and environment. Since the environment will typically be chosen larger than the impurity, the summation will be limited by the dimension of the impurity. It is thus clear that only N states in the environment are needed for the construction of the wave function. We also see that if only one of the singular

values λ_k is nonzero, the state $|\Psi\rangle$ can be factorized and impurity and environment are not entangled. However, if several singular values are nonzero, $|\Psi\rangle$ is entangled.

Embedding theories make use of this division of the system for the calculation of properties of the impurity. By replacing the environment by an approximate model, one tries to calculate the properties of the impurity accurately and cost-effectively. Possible replacements of the environment are given by solvent models or mean-field approximations. When using the mean-field approximations, there is of course no entanglement with the impurity and the Schmidt decomposition of the approximate solution has only one nonzero singular value. For many systems this will suffice. However, for systems with strong static correlation between the impurity and environment it will not. Static correlation refers to systems where a single Slater determinant is not sufficient for a qualitative description of the state of the system. So a system has static correlation whenever substantial entanglement is present in the state. Static correlation between impurity and environment therefore implies several important Schmidt values λ_k in eq. 1.1.

One of the more powerful and popular embedding theories is dynamical mean-field theory (DMFT)[1–4]. It maps the system to an impurity and a noninteracting bath in a self-consistent way. The single-particle Green's function $ig_{ij}(\omega) = \langle a_i^\dagger[\omega - (H - E)]^{-1}a_j\rangle$ is determined in a self-consistent way by fitting the frequency-dependent hybridization function. To obtain ground-state energies, one has to integrate the Green's function over a contour.

A newer embedding theory is given by the density matrix embedding theory (DMET) and was first proposed by Knizia and Chan in ref. [5] for the Hubbard model and later also extended to full chemical Hamiltonians in ref. [6]. For ground state energies, DMET is a computationally cheaper alternative to DMFT, with similar accuracy. The self-consistency for DMET is based on the density matrix $\langle a_i^\dagger a_j\rangle$ and not the Green's function. Although the original theory does not have any frequency dependency, it has been extended to calculate spectral functions as shown in ref. [7].

In DMET the entanglement between impurity and environment is explicitly kept and the wave function is of the form given by eq. 1.1. Finding the Schmidt basis for the environment $\{|\beta_k\rangle\}$ can be done if the exact wave function $|\Psi\rangle$ is known. However, since finding the approximate or exact wave function is precisely what one wants to do, this is not an option. DMET solves the lack of a priori knowledge of $|\Psi\rangle$ by embedding the impurity A in an approximate bath B. Solving this combined impurity and bath system is called the embedded problem. To find this bath space, one can use different techniques. A Fock space of bath orbitals which is obtained from a low-level particle-number conserving mean-field wave function is used in the original refs. [5] and [6] and is illustrated extensively in ref. [8]. However, one can also use single-particle states from Hartree-Fock-Bogoliubov theory [9, 10]. Anti-symmetrized geminal power (AGP) wave functions have also been used to take correlation in the bath into account and achieving a more accurate bath [11]. Extensions of DMET to coupled interacting fermion-boson systems through coherent state wavefunctions for phonon have also been described by

ref. [12]. In this thesis we will use the representation of bath states in a spin lattice system by block-product states as shown in ref. [13]. Recently, this method has been further extended by implementing DMET with the hierarchical mean-field approach [14]. This method will also be discussed in short.

An initial bath state guess can thus be obtained with one of the above methods. First, one can leave them unoptimized and calculate the wavefunction in this Schmidt basis, which is called *single-shot* DMET embedding. Another option, the one suggested in the original references [5, 6], is to introduce a DMET correlation potential $\hat{u}$ to link the *low-level* wave function in the bath with the *high-level* wave function of the impurity. The DMET correlation potential $\hat{u}$ is optimized until (parts of) the density matrices of the low- and high-level wave functions are matched, hence the name *density matrix* embedding theory (DMET). In this thesis, block product states will be chosen as Ansatz for the bath states, and the parameters of this Ansatz will be variationally optimized [13].

2 Density matrix embedding theory

In this section the original DMET algorithm will be sketched, which makes use of a Fock space of bath orbitals and a DMET correlation potential $\hat{u}$ to solve the problem self-consistently, as proposed in refs. [5, 6]. For a more thorough description we refer to these original papers and ref. [8].
First, the system is split up in an impurity and an environment, as said in the introduction. The Hilbert space of the impurity is smaller than the Hilbert space of the environment. Now from the Schmidt decomposition (eq. 1.1) we know that the impurity A can only be entangled with maximally N_A states of the environment B, where N_A is the dimension of the impurity Hilbert space. Thus the entanglement between environment and impurity can be fully represented by a bath with the same dimension as the impurity it is embedding.

2.1 Construction of bath orbitals

For the construction of the bath, we first need an initial approximate low-level state. Then we solve the embedded problem, i.e. impurity plus bath states, in a high-level treatment. We consider as first ground-state approximation a Slater determinant $|\Phi_0\rangle$, for example obtained by solving the complete system in a mean-field Hartree-Fock treatment.

$$|\Phi_0\rangle = \prod_{\mu}^{N_\mathrm{occ}} \hat{a}_\mu^\dagger \, |-\rangle \, . \tag{2.1}$$

Here, N_occ is the number of occupied spin-orbitals denoted by μ. $|-\rangle$ is the true vacuum. From here on, the L orthonormal spin-orbitals for the impurity and environment will be indexed with $klmn$ and the orthonormal impurity and bath orbitals with $pqrs$. Furthermore, there are L_A orbitals in the impurity A and we assume $N_\mathrm{occ} \geq L_\mathrm{A}$. These occupied spin-orbitals $\hat{a}_\mu^\dagger$ can be written in terms of the orthonormal spin orbitals of environment and fragment (impurity):

$$\hat{a}_\mu^\dagger = \sum_{k}^{L} \hat{a}_k^\dagger C_{k\mu}. \tag{2.2}$$

Now we construct the bath orbitals from the overlap matrix of the occupied orbitals with the impurity:

$$S_{\mu\nu} = \sum_{k}^{L_{\mathrm{A}}} C_{\mu k}^{\dagger} C_{k\nu}. \tag{2.3}$$

As shown in ref. [15], at most L_{A} eigenvalues of this overlap matrix will be nonzero. The corresponding L_{A} eigenvectors give us the bath orbitals. The other $N_{occ} - L_A$ occupied orbitals, thus the occupied orbitals that have no overlap with the impurity, yield the unentangled occupied orbitals.

Here we have assumed $N_{\mathrm{occ}} \geq L_{\mathrm{A}}$. If this is not satisfied, it is clear that there can only be maximally N_{occ} bath orbitals. This is because the bath orbitals are constructed through decomposition of the occupied orbitals that have overlap in both impurity and environment. When N_{occ} is of the order of L_{A}, problems arise since DMET will try to add low-lying core electrons of atoms in the environment into the bath states. Since these low-lying core electrons have almost no entanglement with the impurity, this is undesired. By definition of a core, valence and virtual orbital space in the impurity, this can be circumvented [15]. By only constructing bath states that couple to the valence orbital space of the impurity, the number of bath states is reduced. In ref. [15], it is shown that Knizia's intrinsic atomic orbitals [16] are suited for this method.

2.2 The embedding Hamiltonian

The considered Hamiltonian in ref. [6] of the total system is given by:

$$\hat{H} = E_{\mathrm{nuc}} + \sum_{kl}^{L} t_{kl} \hat{a}_k^{\dagger} \hat{a}_l + \frac{1}{2} \sum_{klmn}^{L} (kl|mn) \hat{a}_k^{\dagger} \hat{a}_m^{\dagger} \hat{a}_n \hat{a}_l. \tag{2.4}$$

Now we suppose the system is tiled with different impurities so that the impurities do not overlap and the complete system is covered, i.e. the complete Hilbert space of the system is divided into different non-overlapping subsystems, every subsystem being a different impurity. We now introduce for each impurity A_x a Hermitian one-particle operator $\hat{u}^x$ that acts only within the orbitals of the corresponding impurity. These impurity-specific operators are thus given by:

$$\hat{u}^x = \sum_{kl}^{L_{\mathrm{A}x}} u_{kl}^x \hat{a}_k^{\dagger} \hat{a}_l. \tag{2.5}$$

The sum of all these different $\hat{u}^x$ gives us the DMET correlation potential $\hat{u}$. The mean-field solution used for the construction of the bath orbitals makes use of this potential. To find $|\Phi_0\rangle$, the total system with Hamiltonian $\hat{H} + \hat{u}$ is solved on the mean-field level. Clearly the constructed bath orbitals and the unentangled occupied orbitals corresponding with every A_x are dependent of $\hat{u}$. By projecting the Hamiltonian $\hat{H}$ onto the embedded system, we get the

embedded Hamiltonian $\hat{H}_{\text{emb}} = \hat{P}\hat{H}\hat{P}$, where

$$\hat{P} = \sum_{ii'} |\alpha_i\rangle |\chi_{i'}\rangle \langle\alpha_i| \langle\chi_{i'}| . \tag{2.6}$$

Here $|\alpha_i\rangle$ are the impurity orbitals, $|\chi_{i'}\rangle$ are the environment states, consisting of the bath orbitals and a common determinant from the electrons in the unentangled occupied orbitals. In ref. [8] the embedded Hamiltonian is eventually given by:

$$\hat{H}^{\text{emb},x} = \sum_{pq}^{L_{\text{A}_x}+L_{\text{B}_x}} h^x_{pq} \hat{a}^\dagger_p \hat{a}_q + \frac{1}{2} \sum_{pqrs}^{L_{\text{A}_x}+L_{\text{B}_x}} (pq|rs) \hat{a}^\dagger_p \hat{a}^\dagger_r \hat{a}_s \hat{a}_q - \mu_{\text{glob}} \sum_{r}^{L_{\text{A}_x}} \hat{a}^\dagger_r \hat{a}_r, \tag{2.7}$$

where L_{A_x} is the number of impurity orbitals in the impurity A_x and L_{B_x} is the number of bath orbitals corresponding to A_x. Coulomb and exchange interactions of the impurity and bath states with the external core electrons are encapsulated in the one-particle interactions h^x_{pq}. The introduction of the global chemical potential μ_{glob} is necessary to ensure that the sum of the electrons in all separate impurities is equal to N_{occ}.
The ground state $|\Psi_x\rangle$ of the embedding Hamiltonian $\hat{H}^x_{\text{emb}}$ is found through a high-level method. For example full configuration interaction is used in ref. [5, 6], but also density-matrix renormalization group (DMRG) [9, 17] and coupled-cluster theory [18] have been used. Calculation of the one- and two-particle density matrix of the active space should be possible with the high-level method:

$$D^x_{rs} = \langle\Psi_x|\hat{a}^\dagger_r \hat{a}_s|\Psi_x\rangle , \tag{2.8}$$

$$P^x_{pq|rs} = \langle\Psi_x|\hat{a}^\dagger_p \hat{a}^\dagger_r \hat{a}_s \hat{a}_q|\Psi_x\rangle . \tag{2.9}$$

These density matrices can in turn be used to calculate expectation values for operators. Here we distinguish *local* and *nonlocal* operators. Local operators only act within one impurity, nonlocal operators do not. For local operators it is thus straightforward to get expectation values. For nonlocal operators we need to partition the Hermitian expectation values. As an example we look at the following expectation value where i (j) is part of impurity A_x (A_y):

$$\langle\hat{a}^\dagger_i \hat{a}_j + \hat{a}^\dagger_j \hat{a}_i\rangle = \langle\Psi_x|\hat{a}^\dagger_i \hat{a}_j|\Psi_x\rangle + \langle\Psi_y|\hat{a}^\dagger_j \hat{a}_i|\Psi_y\rangle . \tag{2.10}$$

Here, the density matrix of the impurity that corresponds with the first index is used by convention.

2.3 Self-consistency

The self-consistency consists out of the optimization of the global chemical potential μ_{glob} and the DMET correlation potential $\hat{u}$. The different coefficients of $\hat{u}$ to be optimized will be written in vector notation as $\vec{u}$ from now on. The DMET algorithm looks as follows:

1. The DMET algorithm is initialised with starting conditions $\vec{u} = \vec{0}$ and $\mu_{\text{glob}} = 0$
2. Now we start the optimization cycle for $\vec{u}$
   (a) The mean-field solution $|\Psi_0(\vec{u})\rangle$ is calculated and the bath orbitals are constructed.
   (b) Now we start the optimization subcycle for μ_{glob}
      i. construction of the embedded Hamiltonian $\hat{H}^{\text{emb},x}(\mu_{\text{glob}})$ and solving the embedded problem through a high level treatment gives us $|\Psi_x\rangle$.
      ii. if $||N_{\text{tot}}(\mu_{\text{glob}}) - N_{\text{occ}}|| < \epsilon$, then the subcycle is converged, else we change μ_{glob} until convergence and restart step 2b.
   (c) We minimise the mismatch between the low and high level one particle density matrix: $\min_{\vec{u}} \|D^{\text{low},x}(\vec{u}) - D^{\text{high},x}\|$
   (d) If the DMET correlation potential has converged, i.e. $\|\vec{u}_{new} - \vec{u}_{old}\| < \epsilon$, we found the DMET solution, else we restart step 2 with the newly acquired $\vec{u}$.

A few notes are at their place in step 2c. Here the DMET correlation function is being changed so the low and high level one-particle density matrices match. An exact match is however not always possible, since the low-level mean-field density matrix will always be idempotent, while this is not necessary for the high-level density matrix. Furthermore, we note again that the high-level density matrix is dependent of $\hat{u}$ and thus $\vec{u}$ through the dependency of the bath states and external core electron states of the DMET correlation potential. However, to ease the calculations, the high-level density matrix is kept fixed when minimising the mismatch. In ref. [15], the optimization with fixed high-level density matrix of the mismatch is discussed through a functional optimization.

3 Solving quantum spin systems

There exists a great variety of methods to solve quantum spin systems. The interactions between the different spins of the spin-lattice system can be modelled by the so-called Heisenberg Hamiltonian. This Hamiltonian is given by:

$$\hat{H} = \sum_{i \neq j} J_{ij}^x \hat{S}_i^x \hat{S}_j^x + J_{ij}^y \hat{S}_i^y \hat{S}_j^y + J_{ij}^z \hat{S}_i^z \hat{S}_j^z. \tag{3.1}$$

First, one can make use of exact diagonalization to find the ground state. However, since the Hilbert space of the system for spin-1/2 scales as 2^N, with N the number of spins, this quickly becomes infeasible. In ref. [19], an anti-ferromagnetic spin-1/2 square lattice with J_1- and J_2-interactions (i.e. nearest neighbour (NN) and next-nearest neighbour (NNN) interactions) has been solved for $N = 40$. In [20], the Kitaev-Heisenberg model for a honeycomb lattice is exactly solved for $N = 24$ and these results will also be reproduced in this thesis as a benchmark for the DMET-code. However, for research of infinite lattice systems, this number of spins is not sufficient for researching the bulk properties.
For larger systems, one needs to use approximate methods. Several of the most popular methods will be sketched briefly. In the next chapter the cluster-DMET method of ref. [13] and the extended cluster-DMET method of ref. [14] will be explained more thoroughly.

3.1 Spin-wave Theory

In this section the spin-wave theory will be sketched. For a more elaborate view of this theory in ferromagnets and antiferromagnets, the reader is referred to, for example, refs. [21, 22].
First we will sketch the idea of spin-wave theory with the help of a ferromagnet. The Hamiltonian of the Heisenberg ferromagnet is given by eq. 3.1 with $J_{ij}^x = J_{ij}^y = J_{ij}^z = J_{ij} \leq 0$. The ground state of a Heisenberg ferromagnet is the completely aligned state. When the positive z-axis is chosen in the aligned direction this is given by $|\psi_0\rangle = |S, \cdots, S\rangle$, with S the spin. Now we are interested in the first excited state. An obvious candidate is given by the state where one spin is reduced, for example $|\psi_1\rangle = |S-1, S, \cdots, S\rangle$ if the first spin is reduced. However, this state is no eigenstate of the Heisenberg Hamiltonian since the $S_i^+ S_j^-$ and $S_i^- S_j^+$ terms will move the reduced spin in the lattice. This can be a hint however, that the real excitation is given by a spin wave, i.e. a superposition of states with one reduced spin.

Spin-wave theory introduces so called *magnons*. These quanta are equivalent with phonons in a crystal. They are created by $S^-_{\mathbf{q}} = \frac{1}{\sqrt{N}} \sum_i e^{-i\mathbf{q}\cdot\mathbf{R}_i} S^-_i$, the Fourier transform of S^-_i. The magnon has an energy of $\hbar\omega_{\mathbf{q}} = [J(0) - J(\mathbf{q})]S$, where $J(\mathbf{q})$ is the Fourier transform of J_{ij} with J_{ij} assumed only dependent of the distance between i and j.
Spin-wave theory is also possible for antiferromagnets. Here again only some results will be given [23]. For a derivation of the spin-wave theory in antiferromagnets, the reader is referred to specialised textbooks such as [21, 22].
In antiferromagnets with nearest neighbour coupling J, the exact Néel ordered state is not known. However, by starting with the approximate classical antiferromagnetic state, corrections to the ground state can be calculated. The excitations in the harmonic approximation are described by spin-waves with frequencies

$$\omega_{\mathbf{q}} = 2J\sqrt{1-\gamma^2_{\mathbf{q}}}, \tag{3.2}$$

with

$$\gamma_{\mathbf{q}} = \frac{1}{2} \sum_{i=1,2} \cos(\mathbf{q}\cdot\mathbf{e}_i) \tag{3.3}$$

the structure factor of the lattice. Here $\mathbf{e}_i$ are the unit vectors generating the lattice. There will be two soft points within the first Brillouin zone, i.e. two points where the structure factor is zero ($\mathbf{q} = \mathbf{0}$ and $\mathbf{q} = \mathbf{q}_0$). Around these points the dispersion law will be linear in $\mathbf{q}$ and $\mathbf{q} - \mathbf{q}_0$, respectively. The energy of the magnon is then given by $\hbar\omega_{\mathbf{q}}$.
Spin-wave theory will also have small corrections on the ground state and ground state energy. The zero-point energy of the excitations will renormalize the classical energy of the ground-state. An extra term of the form $\sum_{\mathbf{q}\in \mathrm{BZ}} \frac{\omega_{\mathbf{q}}}{2}$ will be added to the ground state energy, where $\mathbf{q}$ sums over the first Brillouin zone.

3.2 Series expansions

In ref. [24] the series expansion is used to investigate the non-magnetic disordered phase in the Heisenberg model on the square lattice. Here the system with nearest neighbour, next nearest neighbour and third nearest neighbour interactions is investigated:

$$H = \sum_{\langle i,j\rangle} \mathbf{S}_i \cdot \mathbf{S}_j + \sum_{\langle\langle i,j\rangle\rangle} \mathbf{S}_i \cdot \mathbf{S}_j + \sum_{\langle\langle\langle i,j\rangle\rangle\rangle} \mathbf{S}_i \cdot \mathbf{S}_j. \tag{3.4}$$

The Heisenberg Hamiltonian is split up in an unperturbed Hamiltonian and a perturbation. In this expansion, it is assumed that the ground state exhibits a dimer covering, e.g. a staggered or columnar dimer covering as is depicted in figure 5.3 for the square lattice. A certain dimer covering is chosen, and interactions within one dimer of the chosen dimer covering belong to the unperturbed Hamiltonian, while other interactions belong to the perturbation.

$$H = \sum_{\langle i,j\rangle \in D} \mathbf{S}_i \cdot \mathbf{S}_j + \lambda \left(\sum_{\langle i,j\rangle \notin D} \mathbf{S}_i \cdot \mathbf{S}_j + \sum_{\langle\langle i,j\rangle\rangle} \mathbf{S}_i \cdot \mathbf{S}_j + \sum_{\langle\langle\langle i,j\rangle\rangle\rangle} \mathbf{S}_i \cdot \mathbf{S}_j \right). \tag{3.5}$$

At $\lambda = 0$, it is clear that the ground state is indeed the chosen dimer covering. The original model that has to be investigated is given by $\lambda = 1$. The system is now investigated with help of perturbation expansions.

3.3 Large-N expansions

In this section the large-N expansion will be sketched. For a more elaborate view of the large-N expansion, the reader is referred to ref. [25] and references therein.
To start the sketch of the large-N expansion, we look to the $su(2)$ algebra of a spin S. This algebra of the spin at one site can be represented by 2 creation operators $a_\sigma^\dagger$ with $\sigma = \uparrow, \downarrow$. Since we look at a spin with total spin S, we constrain the number of total particles at each site to $a_\uparrow^\dagger a_\uparrow + a_\downarrow^\dagger a_\downarrow = 2S$. The ladder operators S^+ and S^- of the spin can be represented by these creation and annihilation operators as $a_\uparrow^\dagger a_\downarrow$ and $a_\downarrow^\dagger a_\uparrow$ respectively. The particles corresponding to the creation and annihilation operators can be chosen to be fermions (Abrikosov fermions) or bosons (Schwinger bosons). One can calculate the magnetization of these particles through $S^z = \frac{1}{2}(a_\uparrow^\dagger a_\uparrow - a_\downarrow^\dagger a_\downarrow)$, the magnetization is thus given by $\pm\frac{1}{2}$.
It is of course also possible to write the Hamiltonian in terms of the creation and annihilation operators. Now, the idea of the large-N expansion is to generalize the Heisenberg model and the $SU(2)$ symmetry to a larger $SU(N)$ symmetry group with arbitrary N. Now, the corresponding annihilation and creation operators have instead of two *flavours* ($\uparrow$ and $\downarrow$), N flavours. The Heisenberg model is solved by solving the saddle point of the action. In the limit of $N \to \infty$, this calculation simplifies and the solution resembles a mean-field solution. In this large-N limit, the system can be examined and some ground rules have been found for the occurrence of different phases. For example, if the large N equivalent of the spin S matches the lattice coordination number z by $2S = 0 \mod z$, then a valence bond solid phase should be expected. Of course this is a conclusion made from the $SU(N)$ generalization of $SU(2)$ with N large. It is not said that because these conclusions hold for large N, they also hold for $N = 2$. But according to ref. [25] this rule has not been found erroneous up to now.

3.4 Quantum Monte Carlo method

In this section, we shortly discuss the quantum Monte Carlo method. Just like the classical Monte Carlo method, integrals describing expectation values are calculated by drawing pseudo-random generated numbers. An enormous variety of Quantum Monte Carlo methods exist and extensive documentation can also be found on these subjects. *Variational Monte Carlo* for example, is one of the standard examples of quantum Monte Carlo and uses the Monte Carlo method to calculate the expectation value of the ground state energy. A wave function is here optimized in a variational type of approach, hence the name of the method. Furthermore, also *diffusion Monte Carlo, reptation Monte Carlo, Gaussian quantum Monte*

Carlo, path integral Monte Carlo and many other methods exist [26–29].

A large problem in the calculation of fermionic systems with quantum Monte Carlo methods is the so-called sign problem. This problem arises due to the antisymmetry of the wave function under particle-exchange. The sign problem is a *NP-hard* problem, so if a generic exact solution would be found for this problem that scales *polynomially*, all NP problems would be solved in polynomial time. It is highly suspected that this is not possible and a generic solution for the sign problem would thus not be possible in polynomial time. Exact solution of fermionic systems are thus (at this time) only possible with quantum Monte Carlo methods scaling exponentially. One way to solve the sign problem approximately is by using the *fixed-node* method. Here the configuration space is split up in different parts by the nodes of the trial wave function. In variational Monte Carlo and diffusion Monte Carlo, trial wave functions are used, and the quality of the found solution depends heavily on the form of the trial wave function. Many different trial wave functions have been used, a few examples are the Hartree-Fock determinant multiplied by a Jastrow correlation factor (HF-J) and a multiconfiguration self-consistent-field function multiplied by a Jastrow function (MSCF-J) [30]. In each compartment the trial wave has a unique sign. The accuracy of the approximation depends of the guess of the nodal hypersurfaces. The better these guesses correspond with the nodal hypersurfaces of the exact ground state, the better the accuracy of the quantum Monte Carlo method will be.

3.5 Coupled cluster method

In this section a brief overview of the coupled cluster method (CCM) is given, analogous to ref. [31]. For a more general overview of this method, the reader is referred to e.g. ref. [32–35]. The main idea of the CCM is to approximate the ground state by a wave function containing an exponential excitation operator acting on a reference state.

A CCM calculation has as starting point a well-chosen reference state $|\Phi\rangle$. Next to this reference state, also a set of commuting multispin creation operators C_I^+ have to be defined, with I a complete set of many-body configurations. Furthermore, C_I^- are defined as the commuting multispin destruction operators and are given by the Hermitian adjoint of C_I^+. $\{|\Phi\rangle, C_I^+\}$ are chosen in such way that $\langle\Phi| C_I^+ = 0 = C_I^- |\Phi\rangle, \forall I \neq 0$, is valid ($C_0^+ = 1$).

Now we want to treat every spin site equivalently and propose $|\Phi\rangle = |\downarrow\downarrow\downarrow\cdots\rangle$ as reference state. It is clear that the corresponding multispin creation operators are given by $C_I^+ = \hat{S}_i^+, \hat{S}_i^+\hat{S}_j^+, \hat{S}_i^+\hat{S}_j^+\hat{S}_k^+, \cdots$, where $i, j, k, \cdots$ are arbitrary lattice sites.

The exact ket and bra ground state wave functions, $|\Psi\rangle$ and $\left\langle\tilde{\Psi}\right|$, corresponding with Hamil-

tonian H are given by:

$$\hat{H}\left|\Psi\right\rangle = E\left|\Psi\right\rangle \qquad \left\langle\tilde{\Psi}\right|\hat{H} = E\left\langle\tilde{\Psi}\right|$$

$$\left|\Psi\right\rangle = e^{S}\left|\Phi\right\rangle \qquad S = \sum_{I\neq 0}\mathcal{S}_I C_I^{+}$$

$$\left\langle\tilde{\Psi}\right| = \left\langle\Phi\right|\tilde{S}e^{-S} \qquad \tilde{S} = 1 + \sum_{I\neq 0}\tilde{\mathcal{S}}_I C_I^{-}$$

S and $\tilde{S}$ are the so-called correlation operators and contain the correlation coefficients $\mathcal{S}_I$ and $\tilde{\mathcal{S}}_I$. These coefficients are the unknowns of the problem. In this framework, the expectation value of an operator A of the ground state is given by

$$\langle A\rangle = \left\langle\tilde{\Psi}\middle|A\middle|\Psi\right\rangle. \tag{3.6}$$

Now the unknown correlation coefficients can be found by minimizing the expectation value $\langle H\rangle = \left\langle\tilde{\Psi}\middle|H\middle|\Psi\right\rangle$ with respect to the correlation coefficients.

$$\frac{\partial\langle H\rangle}{\partial\tilde{\mathcal{S}}_I} = 0 \rightarrow \langle\phi|C_I^{-}e^{-S}He^{S}|\phi\rangle = 0, \qquad I\neq 0 \tag{3.7}$$

$$\frac{\partial\langle H\rangle}{\partial\mathcal{S}_I} = 0 \rightarrow \langle\phi|\tilde{S}e^{-S}[H,C_I^{+}]e^{S}|\phi\rangle = 0, \qquad I\neq 0 \tag{3.8}$$

From equation 3.7, it is also clear that the ground state energy of the stationary point (i.e. the solution of equations 3.7 and 3.8) is given by $E_g = \langle\phi|e^{-S}He^{S}|\phi\rangle$.
It is possible to study spin systems in the thermodynamic limit $N\rightarrow\infty$ (with N number of spins) through coupled cluster method (CCM). However, it is quite obvious that the complete set of many-body configurations I will be infinite in this case and the correlation operators will be an infinite sum. To solve this problem, we make use of a truncation of the sum and the lattice symmetry. One of the most used truncation methods is the so-called LSUBn [33]. Here, only multispin correlations consisting of maximally n connected sites are taken into account. However, taking this measure will still give us an infinite number of configurations on the infinite lattice. So now we use the lattice symmetry to discard equivalent configurations, giving us a finite number of configurations.
Even though the reference state is a state with semiclassical long-range order, precise results can also be obtained with the use of this reference state in phases where semiclassical long-range order is destroyed [31].

3.6 Density matrix renormalization group

The density matrix renormalization group (DMRG) is one of the most successful methods for the study of one-dimensional quantum lattices since its invention in 1992 by Steve White [36,

37]. However, also 2D systems, like small strips or cylinders (for example in ref. [38]), can be successfully calculated.

DMRG is a variational optimization within the space of matrix product states (MPS). The decomposition of a quantum state into MPS can be seen as follows. We imagine a one dimensional lattice with L sites where each site has a d-dimensional local state space $\{\sigma_i\}$. An eigenstate of the system can then be written as

$$|\Psi\rangle = \sum_{\sigma_1 \cdots \sigma_L} c_{\sigma_1,\cdots,\sigma_L} |\sigma_1, \cdots, \sigma_L\rangle \,. \tag{3.9}$$

There are clearly d^L different $c_{\sigma_1 \cdots \sigma_L}$ coefficients and as such they grow exponentially with L. In the first step, we rearrange the d^L different coefficients into a matrix Ψ with dimension $(d \times d^{L-1})$ with $\Psi_{\sigma_1,(\sigma_2 \cdots \sigma_L)} = c_{\sigma_1 \cdots \sigma_L}$. SVD decomposition can be executed on this matrix and gives us:

$$c_{\sigma_1 \cdots \sigma_L} = \sum_{a_1}^{r_1} U[1]_{\sigma_1,a_1} S[1]_{a_1,a_1} (V[1]^\dagger)_{a_1,(\sigma_2 \cdots \sigma_L)} = \sum_{a_1}^{r_1} A[1]^{\sigma_1}_{a_1} (V[1]^\dagger)_{a_1,(\sigma_2 \cdots \sigma_L)}. \tag{3.10}$$

Here the dimensions of $U[1]$, $S[1]$ and $V[1]$ are given by $(d \times r_1)$, $(r_1 \times r_1)$ and $(r_1 \times d^{L-1})$ respectively, where r_1 is given by $\min(d, d^{L-1})$. After successive SVD decomposition of $V[k]$ we finally get

$$c_{\sigma_1 \cdots \sigma_L} = \sum_{\{a_k\}} A[1]^{\sigma_1}_{a_1} A[2]^{\sigma_2}_{a_1;a_2} A[3]^{\sigma_3}_{a_2;a_3} \cdots A[L]^{\sigma_L}_{a_{L-1}}. \tag{3.11}$$

The wave function is thus now represented by a matrix product state, where except for the first and last site, every site is represented by a rank-3 tensor. One index (i.e. σ_k) of every tensor represents the physical index, while the other two (or one for the two border sites) indices are called the *virtual* indices (i.e. a_{k-1} and a_k). The dimension of the virtual indices is given by $\dim(a_k) = \min(d^k, d^{L-k})$. These tensors and their contractions are represented in figure 3.1(a) by a MPS graph. It is clear that the dimension of the virtual bonds grows exponentially to the center of the one-dimensional chain. This exponential growth of the tensor dimension makes solving for the exact ground state in the MPS form not feasible for larger systems. However, by truncating its dimension with a *virtual* dimension D, i.e. $\dim(a_k) = \min(d^k, d^{L-k}, D)$, the MPS ansatz can be solved. The truncation of the maximal dimension within MPS has consequences for correlations between the sites. All correlation functions between two sites decrease exponentially with the distance between the two sites when truncating the maximal dimension. The MPS-ansatz will fail to accurately solve critical systems, since critical systems are characterized by correlation functions that decrease as a power law. For one-dimensional critical systems, the multiscale entanglement renormalization ansatz (MERA) can be used instead [39]. The optimization of the MPS ansatz happens by sweeping through the one-dimensional lattice and optimizing rank-3 MPS tensors of two neighbouring sites simultaneously (for the two-site DMRG algorithm). For further details, the reader is referred to articles specificly about DMRG [40, 41].

3.7 Projected entangled pair states

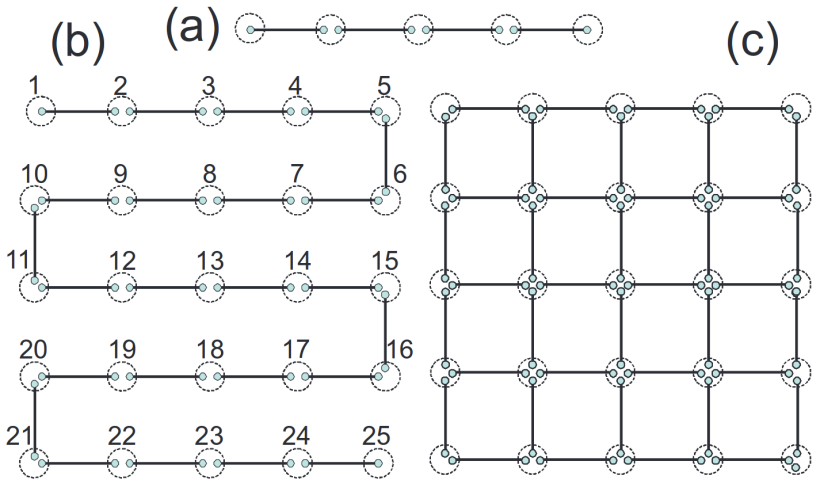

Figure 3.1: Graphical representation of a MPS in one dimension (a) and in two dimensions on a square lattice (b) and of a PEPS on a two-dimensional square lattice (c). The large circles represent the physical sites while the small circles represent the sites of the auxiliary systems. The full lines are the bonds, i.e. the maximally entangled states in the auxiliary systems. [42]

In ref. [43] it is shown that the MPS of a physical system can be written in terms of two auxiliary systems. Every site k (with Hilbert space dimension d) of the system is replaced by two auxiliary sites a_k and b_k, each with maximal dimension D (the truncation dimension). At the boundaries of the chain, there is only one auxiliary system. This is schematically represented in figure 3.1(a) and 3.1(b). Now systems b_k and a_{k+1} are assumed to be in a maximal entangled state i.e. $|\phi\rangle = \sum_{n=1}^{D} |n,n\rangle$, these are the solid bonds in figure 3.1(a) and 3.1(b). Now the state of the physical system is obtained by applying linear operators Q_k to each pair a_k, b_k mapping the auxiliary systems to the physical system.

$$\begin{aligned} |\Psi\rangle &= Q_1 \otimes Q_2 \otimes \cdots Q_L \, |\phi\rangle \cdots |\phi\rangle \\ &= \sum_{\sigma_1,\cdots,\sigma_L=1}^{d} \mathrm{F}_1(A_1^{\sigma_1}, \cdots, A_L^{\sigma_L}) \, |\sigma_1, \cdots, \sigma_L\rangle \,, \end{aligned} \tag{3.12}$$

where F_1 takes appropriate traces of the matrices A_k^s, i.e. it contracts the matrices along the bonds. The matrices A_k^s are the same matrices as in eq. 3.11.
However, without choosing the truncation dimension D very large, only systems with short range interactions will be simulated accurately. Thus, when applying the MPS ansatz to a two-dimensional system like in figure 3.1(b), some nearest-neighbour sites such as site 6 and 15 will not be nearest-neighbour in the MPS ansatz. The interactions between these two

sites will not be represented correctly by the MPS ansatz if D is not chosen large enough. Unfortunately, the computational cost also grows as $\mathcal{O}(D^3)$.
In ref. [42] F. Verstraete and J. I. Cirac introduce the so called projected entangled pair states (PEPS). It is a generalisation of the MPS to higher dimensions and makes use of more than two auxiliary systems. In figure 3.1(c) PEPS is shown for a two-dimensional square lattice. For this case PEPS makes use of four auxiliary systems (except two at the corners and three at the sides). There is one auxiliary system for every direction of the lattice i.e. up, down, left and right and appropriate auxiliary systems on different sites are maximally entangled as schematically shown in the figure. Now the state $|\Psi\rangle$ is again obtained by applying of an appropriate linear operator Q on every site on the product of all the maximal entangled states (the bonds). This linear operator projects the auxiliary systems on the physical system. Eventually we get:

$$|\Psi\rangle = \sum_{\sigma_1,\cdots\sigma_N=1}^{d} \mathrm{F}_2(\{A_n^{\sigma_n}\})\,|\sigma_1,\cdots,\sigma_N\rangle\,, \tag{3.13}$$

where F_2 contracts the different tensors A_n^s along the bonds. It is clear that this different ansatz preserves better the short-range interactions between neighbouring sites compared to the MPS when truncated.

4 Cluster density matrix embedding theory

In this chapter the derivation of the modified cluster density matrix embedding theory [13] is given. We start by dividing the total spin lattice system into an impurity cluster and an environment. Through Schmidt decomposition we know that the exact ground state can be decomposed as:

$$|\Psi\rangle = \sum_i a_i \, |\alpha_i\rangle \, |\beta_i\rangle \, . \tag{4.1}$$

Here $|\alpha_i\rangle$ and $|\beta_i\rangle$ are wavefunctions in the Hilbert spaces restricted to the impurity and environment respectively. The set $\{|\alpha_i\rangle\}$ denotes the complete basis of the impurity spin sites and the set $\{|\beta_i\rangle\}$ hass the same dimension. Finding the set $\{|\alpha_i\rangle\}$ is easy as it is just the basis of the impurity spin sites; the difficult part is finding the set $\{|\beta_i\rangle\}$.
Following the recipe for DMET given by Knizia *et al.* [5], i.e. replacing the bath states with a one-particle mean-field state, would give a hierarchical mean-field. This give no advantage compared to mean-field solutions [13]. Fan *et al.* [13] propose a replacement of the exact embedding bath states $|\beta_i\rangle$ by a set of block-product states $\left|\beta_i^{\mathrm{BPS}}\right\rangle$. With this approximation the wave function of this impurity model becomes:

$$|\Psi\rangle_{\mathrm{imp}} = \sum_i a_i \, |\alpha_i\rangle \left|\beta_i^{\mathrm{BPS}}\right\rangle . \tag{4.2}$$

To define these block-product states, we first divide the spin lattice system in different equivalent clusters. We then pick one of these clusters as the impurity. The other clusters are called the bath clusters. With this division of the lattice system, the block-product states can be defined as follows:

$$\left|\beta_i^{\mathrm{BPS}}\right\rangle = \bigotimes_{C \in \text{bath clusters}} \sum_\beta b^i_{C\beta} \, |\beta\rangle_C \, . \tag{4.3}$$

Here $\{|\beta\rangle_C\}$ is a complete set of states within the Hilbert space restricted to the bath cluster. For example, if each bath cluster contains 3 sites with spin-$1\frac{1}{2}$, we have $\{|\downarrow\downarrow\downarrow\rangle \, , |\downarrow\downarrow\uparrow\rangle \, , |\downarrow\uparrow\downarrow\rangle \, , .. , |\uparrow\uparrow\uparrow\rangle\}$. These block-product states now have to be optimized so that eq. 4.2 optimally represents the exact ground state wave function. The dimension of the complete Hilbert space is, as

said before, given by dim $= 2^N$ with N the number of spins and hence, grows exponentially with the number of spins. The number of degrees of freedom of the cluster DMET-ansatz is given by $2^{N_s}(2^{N_s}-1)(N_C-1)+2^{N_s}$, with N_s the number of spins in a cluster and N_C the number of clusters. When the cluster size is kept fixed, the degrees of freedom scale linearly with the number of spins (or the number of cluster N_C). This is clearly the big advantage of the cluster DMET-ansatz.

4.1 Optimizing the wavefunction

Optimization of the block-product states and finding the ground state of the impurity model given by eq. 4.2 proceeds by the linear iteration optimization algorithm [44, 45]. The goal is to minimize the energy of the wave function in the impurity model: $E_{\text{imp}} = \langle\Psi|\hat{H}|\Psi\rangle_{\text{imp}} \,/\, \langle\Psi|\Psi\rangle_{\text{imp}}$. The iterative optimization happens by keeping a large number of coefficients of th variational wave function fixed, and only optimizing a restricted number of coefficients at a time. First of all, the variational wave function within the impurity model can be written as

$$|\Psi\rangle_{\text{imp}} = \sum_i a_i \,|\alpha_i\rangle \left(\bigotimes_{C\in\text{bath clusters}} \sum_\beta b^i_{C\beta}\,|\beta\rangle_C \right), \tag{4.4}$$

with C being the different bath clusters. For every possible wave function of this form, we can take

$$\sum_\beta b^{i*}_{C\beta} b^i_{C\beta} = 1, \tag{4.5}$$

by absorbing appropriate factors in the a_i's. Even more, when the wave function is normalized,

$$\sum_i a_i^* a_i = 1 \tag{4.6}$$

will also be satisfied.

The coefficients of the variational wave function are obtained with a restricted optimization. All coefficients are fixed, except for the a_i's and $b^{i_0}_{B_0\beta}$ (The b-coefficients corresponding with a certain impurity state and bath cluster). By looping over the different i_0's and bath-clusters we optimize the DMET wave function iteratively.

We now rewrite the wave function given by eq. 4.4 as

$$|\Psi\rangle_{\text{imp}} = \sum_{i\neq i_0} a_i\,|\alpha_i\rangle \prod_C \sum_\beta b^i_{C\beta}\,|\beta\rangle_C + \sum_\beta a_{i_0} b^{i_0}_{B_0\beta}\,|\alpha_{i_0}\rangle\,|\beta\rangle_{B_0} \prod_{C\neq B_0} \sum_{\beta'} b^{i_0}_{C\beta'}\,|\beta'\rangle_C\,. \tag{4.7}$$

Since optimization happens over a_i with $i \neq i_0$ and $a_{i_0} b^{i_0}_{B_0\beta'}$, every iteration optimizes in the $\{|\phi_\alpha\rangle\,, |\phi_\beta\rangle\}$-basis with

$$|\phi_{\alpha_i}\rangle = |\alpha_i\rangle \prod_C \sum_\beta b^i_{C\beta}\,|\beta\rangle_C\,,$$

$$|\phi_\beta\rangle = |\alpha_{i_0}\rangle\,|\beta\rangle_{B_0} \prod_{C\neq B_0} \sum_{\beta'} b^{i_0}_{C\beta}\,|\beta'\rangle_C\,.$$

From here on, the parameters to optimize, i.e. a_i with $i \neq i_0$ and $a_{i_0} b^{i_0}_{B_0\beta'}$, will be represented by pm.
To find the optimal solution with every iteration, the following Lagrangian is minimized within this restricted Hilbert space:

$$\mathcal{L} = \langle \Psi_0(\mathrm{pm}) | \hat{H} | \Psi_0(\mathrm{pm}) \rangle - \lambda \langle \Psi_0(\mathrm{pm}) | \Psi_0(\mathrm{pm}) \rangle , \tag{4.8}$$

which yields the following linear eigenvalue problem:

$$\frac{\partial \mathcal{L}}{\partial \mathrm{pm}^*} = \left\langle \frac{\partial \Psi_0}{\partial \mathrm{pm}^*} \middle| \hat{H} \middle| \Psi_0 \right\rangle - \lambda \left\langle \frac{\partial \Psi_0}{\partial \mathrm{pm}^*} \middle| \Psi_0 \right\rangle = 0 \tag{4.9}$$

Within every iteration, the solution corresponding to the smallest λ is chosen. It is clear that the solution of the previous iteration can still be chosen within the freedom of the parameters in the current iteration. Because of this, the minimal λ-value chosen in the current iteration has to be at least as small as the λ value of the previous iteration. Since λ decreases with every two consecutive iterations, we converge to a minimal λ value. It is possible that convergence happens to a relative minimum, and not to the absolute minimum of the DMET-wave function. The complexity of a major iteration (i.e. an iteration over all i-values and over all bath-clusters) is of the order $\mathcal{O}(N_C^2)$ with N_C the number of clusters. The number of iterations needed up to convergence can increase when increasing the number of clusters. The scaling of the problem when enlarging the number of spins is more favourable than the exponential scaling of the exact diagonalization, as long as the size of the clusters does not change. In appendix A, the details of the calculations are investigated in more depth.

4.2 Calculating expectation values

In this section, the calculation of expectation values within the cluster DMET framework is discussed. The method of calculation is equivalent to the method used in DMET as discussed in section 2.2. In the cluster DMET, we divide our lattice into different clusters and choose one cluster as our impurity cluster. In this thesis the clusters are chosen in such way that they are all equivalent with respect to the lattice symmetry. All clusters can be transformed in another by using a translation or rotation for which the lattice is invariant. Thus by picking one cluster as impurity and calculating its corresponding DMET wave function $|\Psi_C\rangle$, we immediately know all the DMET wave functions corresponding with the other clusters picked as impurity. This is a great advantage for the computational time.
In section 2.2 we noted the existence of *local* and *nonlocal* operators. Local operators act within one impurity and nonlocal operators do not. Just like in the original DMET framework expectation values for local operators are quite straightforward, while expectation values for nonlocal operators require some inventiveness to calculate. When a local operator $\hat{A}$ only acts upon cluster C, its expectation value can be calculated by: $\left\langle \hat{A} \right\rangle = \langle \Psi_C | \hat{A} | \Psi_C \rangle$. Note

however that also operators consisting of summations of local operators impose no problem. For example, the expectation value of the total spin in the z-direction is given by:

$$\left\langle \hat{S}^z_{\text{tot}} \right\rangle = \sum_C \langle \Psi_C | \hat{S}^z_{\text{tot}_C} | \Psi_C \rangle = N_C \langle \Psi_C | \hat{S}^z_{\text{tot}_C} | \Psi_C \rangle \,, \tag{4.10}$$

where $\hat{S}^z_{\text{tot}_C}$ is the total spin in the z-direction restricted to sites belonging to cluster C. Since all $|\Psi_C\rangle$ are equivalent, the summation over the different clusters is simplified in the last step and N_C is the number of clusters of the system.
For nonlocal operators the original DMET framework suggests splitting these operators as denoted in equation 2.10. The expectation values of interest for the spin lattice systems will be given by a summation of scalar products of spin operators. The expectation value can thus be written as the sum of the expectation values of the different terms $\left\langle \hat{\mathbf{S}}_i \cdot \hat{\mathbf{S}}_j \right\rangle$. When both i and j are sites within one impurity this expectation value is then an expectation value of a local operator. However, when this is not the case, this expectation value is an expectation value of a nonlocal operator and in equivalence with equation 2.10 will be calculated as:

$$\left\langle \hat{\mathbf{S}}_i \cdot \hat{\mathbf{S}}_j \right\rangle = \frac{1}{2} \langle \Psi_{C_i} | \hat{\mathbf{S}}_j \cdot \hat{\mathbf{S}}_i | \Psi_{C_i} \rangle + \frac{1}{2} \langle \Psi_{C_j} | \hat{\mathbf{S}}_i \cdot \hat{\mathbf{S}}_j | \Psi_{C_j} \rangle \,, \tag{4.11}$$

where $|\Psi_{C_i}\rangle$ and $|\Psi_{C_j}\rangle$ are the cluster-DMET solutions with the impurity chosen to be the cluster of site i or site j, respectively. Since the solutions of the cluster DMET for different impurity clusters are equivalent, the calculation of expectation values of operators that respect the lattice symmetry can be simplified, examples of these are the Hamiltonian $\hat{H}$ and the squared total spin $\hat{\mathbf{S}}^2_{\text{tot}}$. These will be given by:

$$\left\langle \hat{H} \right\rangle = N_c \sum_{i \in \text{C},\, j} J_{ij} \left\langle \Psi_C \middle| \hat{\mathbf{S}}_i \cdot \hat{\mathbf{S}}_j \middle| \Psi_C \right\rangle , \tag{4.12}$$

$$\left\langle \hat{\mathbf{S}}^2_{\text{tot}} \right\rangle = N_c \sum_{i \in \text{C},\, j} \left\langle \Psi_C \middle| \hat{\mathbf{S}}_i \cdot \hat{\mathbf{S}}_j \middle| \Psi_C \right\rangle . \tag{4.13}$$

Here, N_C is the number of clusters in the system. We note that the local parts of the summation (i.e. those that act within one impurity) are counted double, while the interactions between impurity and bath are taken into account only once.

4.3 Green's function

Apart from the ground state we also want to calculate dynamic properties of the system. In this section the calculation of the Green's function (and the related spectral function) is sketched. First the Green's function is defined as

$$G(\omega, \hat{X}) = \sum_{i \in \text{spins}} \langle \Psi_0 | \hat{X}_i^\dagger \frac{1}{\omega - (\hat{H} - E_0) + i\eta} \hat{X}_i | \Psi_0 \rangle \,. \tag{4.14}$$

As $\hat{X}_i$, we take one of the spin operators at a certain spin, e.g. $\hat{S}_i^+$. Finally the spectral functions are defined as $A(\omega) = -\frac{1}{\pi}\Im[G(\omega)]$. We now look at how to calculate the part of the spectral function corresponding with one summation term of eq. 4.14. Since $\hat{X}_i |\Psi_0\rangle$ is a wave function with only real coefficients, the following holds:

$$\begin{aligned} &-\frac{1}{\pi}\Im \langle\Psi_0|\hat{X}_i^\dagger \frac{1}{\omega - (\hat{H} - E_0) + i\eta}\hat{X}_i|\Psi_0\rangle \\ =&\frac{\eta}{\pi}\langle\Psi_0|\hat{X}_i^\dagger \frac{1}{\Big(\omega - (\hat{H} - E_0) - i\eta\Big)}\frac{1}{\Big(\omega - (\hat{H} - E_0) + i\eta\Big)}\hat{X}_i|\Psi_0\rangle \end{aligned} \tag{4.15}$$

To find the spectral function, we first calculate

$$|\Psi_1\rangle = \frac{1}{\omega - (\hat{H} - E_0) + i\eta}\hat{X}_i |\Psi_0\rangle . \tag{4.16}$$

Eq. 4.15 is now given by

$$\frac{\eta}{\pi}\langle\Psi_1|\Psi_1\rangle . \tag{4.17}$$

To find eq. 4.16 within the block product state ansatz of eq. 4.4, we minimise the 2-norm of the residue within the parameter space:

$$\begin{aligned} &\min_{|\Psi_1\rangle}||(\omega + E_0 - \hat{H} + i\eta)|\Psi_1\rangle - \hat{X}_i|\Psi_0\rangle||_2 \\ =&\min_{|\Psi_1\rangle}\{\langle\Psi_1|(\omega + E_0 - \hat{H} - i\eta)(\omega + E_0 - \hat{H} + i\eta)|\Psi_1\rangle + \langle\Psi_0|\hat{X}_i^\dagger\hat{X}_i|\Psi_0\rangle \\ &-\langle\Psi_0|\hat{X}_i^\dagger(\omega + E_0 - \hat{H} + i\eta)|\Psi_1\rangle - \langle\Psi_1|(\omega + E_0 - \hat{H} - i\eta)\hat{X}_i|\Psi_0\rangle\}. \end{aligned} \tag{4.18}$$

The minimum within a certain parameter space can be found by solving

$$\frac{\partial}{\partial \mathrm{pm}^*}||(\omega + E_0 - \hat{H} + i\eta)|\Psi_1(\mathrm{pm})\rangle - \hat{X}_i|\Psi_0\rangle|| = 0. \tag{4.19}$$

Eventually, this gives us

$$\begin{aligned} &[(\omega + E_0)^2 + \eta^2]\left\langle\frac{\partial\Psi_1}{\partial\mathrm{pm}^*}\middle|\Psi_1\right\rangle - 2(\omega + E_0)\left\langle\frac{\partial\Psi_1}{\partial\mathrm{pm}^*}\middle|\hat{H}\middle|\Psi_1\right\rangle + \left\langle\frac{\partial\Psi_1}{\partial\mathrm{pm}^*}\middle|\hat{H}^2\middle|\Psi_1\right\rangle = \\ &(\omega + E_0 - i\eta)\left\langle\frac{\partial\Psi_1}{\partial\mathrm{pm}^*}\middle|\hat{X}_i\middle|\Psi_0\right\rangle - \left\langle\frac{\partial\Psi_1}{\partial\mathrm{pm}^*}\middle|\hat{H}\hat{X}_i\middle|\Psi_0\right\rangle . \end{aligned} \tag{4.20}$$

4.4 Verification of the implementation

Now we want to check the implemented algorithm for finding the ground state and the spectral function. We recall the variational wave function for the cluster DMET method given by eq. 4.4. When the system is only divided into two clusters this wave function is reduced to

$$|\Psi\rangle_{\mathrm{imp}} = \sum_\alpha a_\alpha |\alpha\rangle \sum_\beta b_\beta^\alpha |\beta\rangle \tag{4.21}$$

It is clear that in this case, the restricted Hilbert space of the variational wave function is given by the complete Hilbert space of the system. It is thus possible to write every wave function, and more particular the ground state wave function, in the form of the proposed variational wave function.

Now, to test our implemented algorithm, we look at the $J_1 - J_2$ model on the square lattice (i.e. nearest neighbour and next nearest neighbour interactions) for 8 spins. By dividing the 8-spin lattice into two clusters of equal size, the cluster DMET algorithm should be able to find the exact ground state. Exact diagonalization of this 8-spin system is certainly feasible and thus a comparison of the cluster DMET solution with the exact solution is possible. When comparing the two wave functions, we notice that they correspond to each other, up to a possible phase difference and within a small deviation due to the convergence criterion of the cluster DMET code and the finite precision of the computer. The norm of the difference between the DMET and the ED wave solution is given in figure 4.1, the possible phase difference has been taken into account. The DMET-algorithm finds the same ground state as ED, as can be seen by the small differences in figure 4.1.

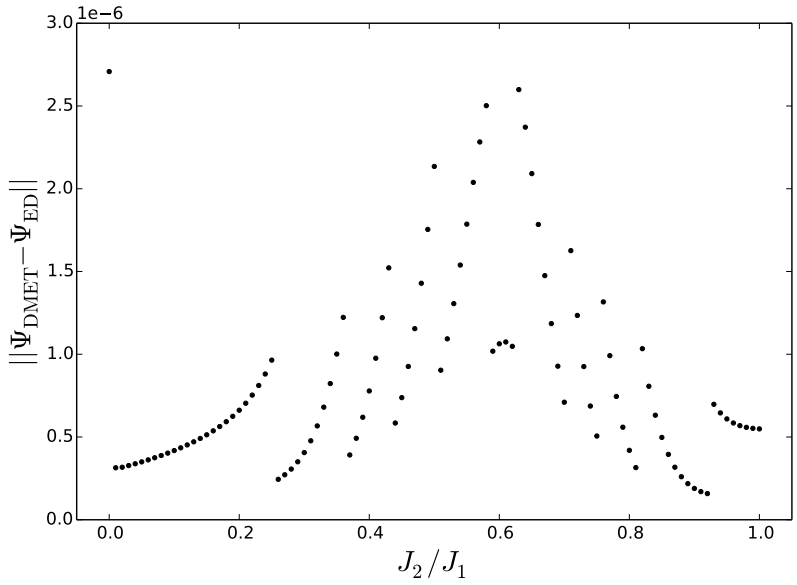

Figure 4.1: The norm of the difference between the DMET and the ED wave solution.

To check the cluster DMET algorithm for the spectral function, we can also compare it with the corresponding exact diagonalization algorithm. Again correspondence between the two solutions is found within a very small deviation due to the convergence criterion of the cluster DMET code and the finite precision of the computer.

4.5 Extension of the cluster DMET method

Recently, J. Qin, Q. Jie and Z. Fan proposed an extension of the DMET method on spin lattices [14]. In ref. [13], it is noted that the impurity has strong correlations with spins in the nearby environment while the correlation for the spins further away is relatively weak and approximately corresponds with a mean-field approximation (see figure 3 of ref. [13]). Because of this result, the suggestion is made to solve the impurity and nearby surroundings in a high level method while treating the environment further away in a mean-field approximation. The DMET method is reformulated in analogy with the hierarchical mean-field (HMF) method [46]. To do this, the lattice is split up in a superblock, consisting of the impurity and nearby surroundings, and the further environment. The wave function of the superblock is formulated in equivalence with cluster DMET and the total wave function of the lattice is given by a translational invariant wave function constructed out of the superblock wave function, i.e. if the wave function of the superblock is given by $|\Psi_{\text{superblock}}\rangle$ then the total wave function of the system is given by $|\Phi\rangle = \prod_b |\Psi_{\text{superblock}}\rangle_b$, where b is the index of superblocks. The lattice is thus covered by translationally invariant superblocks. Since the environment is treated in a mean-field way and since the total wave function consists of translational invariant superblocks, the infinite lattice can be investigated.

Now $|\Psi_{\text{superblock}}\rangle$ still has to be found. The calculation of the superblock wave function happens quite analogous to the cluster-DMET algorithm. As previously stated, the superblock consists of an impurity and a nearby surrounding. In ref. [14] a 6×6 superblock is divided into a 2×2 impurity and 8 surrounding 2×2 bath clusters. Now the variational wave function $|\Psi_{\text{superblock}}\rangle$ can be chosen equivalent with eq. 4.4 and optimized in the same way (but instead of periodic boundary conditions, the superblock is surrounded by an infinite environment). Qin *et al.* also further extended this wave function by proposing a wave function of the following form:

$$|\Psi_{\text{superblock}}\rangle = \sum_{\tau}^{T} |\alpha_\tau\rangle \left(\lambda_\tau^1 |\beta_\tau\rangle_{\text{BPS}}^1 + \cdots + \lambda_\tau^K |\beta_\tau\rangle_{\text{BPS}}^K\right). \tag{4.22}$$

where $|\beta_\tau\rangle_{\text{BPS}}^k$ are block-product states as defined in eq. 4.3. For $K = 1$ this variational wave function is the same as the one in the original cluster DMET algorithm. Optimization of this new variational wave function happens equivalently with the cluster DMET but with an additional iteration over K.

5 $J_1 - J_2$ model on the square lattice

The square lattice system with antiferromagnetic nearest neighbour (NN) and next-nearest neighbour (NNN) interactions has been widely studied over the years and is a model example of a frustrated quantum spin system. This is also the spin system that is studied in the original paper of Fan *et al.* introducing cluster DMET for the spin lattice [13]. In this model J_1 is the NN interaction strength while J_2 is the NNN interaction strength. When the NNN interaction is turned off, there is no frustration in the system, and the ground state is the Néel antiferromagnetic (AF) ground state. The NNN interaction introduces frustration. The square lattice and interactions are depicted in figure 5.1.

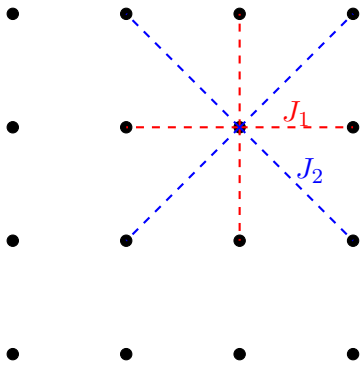

Figure 5.1: Square lattice with nearest neighbour and next nearest neighbour interactions.

The Hamiltonian in this $J_1 - J_2$ model is given by

$$\hat{H} = J_1 \sum_{\langle i,j \rangle} \hat{\mathbf{S}}_i \cdot \hat{\mathbf{S}}_j + J_2 \sum_{\langle\langle i,k \rangle\rangle} \hat{\mathbf{S}}_i \cdot \hat{\mathbf{S}}_k \tag{5.1}$$

with J_1, $J_2 \leq 0$ and where $\langle i,j \rangle$ sums over the nearest neighbours and $\langle\langle i,k \rangle\rangle$ sums over the next-nearest neighbours. The Hamiltonian given by eq. 5.1 has been widely used and examined. This partly because of its fundamental interest in its simplicity, but also for its use in describing cuprates, Fe-based superconductors, and other materials. High-T_c superconductivity in iron pnictide (or oxypnictides) have been discovered recently with LaOFeAs being the first [47]. The Fe atoms form a square lattice in these iron pnictides and they exhibit NN and NNN superexchange interactions that can be described with this $J_1 - J_2$ model (however with

$S = 1$ or 2). When the crystal is doped, ref. [48] suggests an effective model with a $t - J_1 - J_2$ Hamiltonian, introducing a kinetic component. This should give rise to superconductivity. Also the properties of Li_2VOSiO_4 have been investigated through the $J_1 - J_2$ model [49].
This model has been extensively examined and it is widely accepted that the model exhibits three phases, of which two exhibit long-range order (LRO). There is a Néel AF ordered phase at low J_2/J_1, then a phase transition to a disordered nonmagnetic phase at $J_2/J_1 \approx 0.4$, and a second phase transition from nonmagnetic phase to an ordered collinear phase at $J_2/J_1 \approx 0.6$. In the next paragraphs the different phases will be discussed extensively, starting with the Néel AF phase at low J_2/J_1 values.

5.1 Phases of the $J_1 - J_2$ model on the square lattice

5.1.1 Classical ground state of the $J_1 - J_2$ model ($S \to \infty$)

When looking at a translation invariant classical Heisenberg model with

$$\mathcal{H} = J_1 \sum_{\langle ij \rangle} \vec{S}_i \cdot \vec{S}_j + J_2 \sum_{\langle\langle ij \rangle\rangle} \vec{S}_i \cdot \vec{S}_j \tag{5.2}$$

on a Bravais lattice, it is easy to find *a* classical ground state. Minimization of the energy is always possible by imposing a planar helix of the form

$$\vec{S}_{\mathbf{r}} = \vec{e}_1 \cos(\mathbf{q} \cdot \mathbf{r}) + \vec{e}_2 \sin(\mathbf{q} \cdot \mathbf{r}) \tag{5.3}$$

where $\mathbf{q}$ minimizes the Fourier transform $J(\mathbf{q})$ of the coupling [23]. For a square lattice $J_1 - J_2$ model this is given by [23]

$$J(\mathbf{q}) = J_1(\cos(q_x) + \cos(q_y)) + J_2(\cos(q_x + q_y) + \cos(q_x - q_y)) \tag{5.4}$$

For $J_2 < 0.5J_1$, $J(\mathbf{q})$ has a minimum at (π, π). Eq. 5.3 is then given by the Néel AF LRO state depicted left in figure 5.2. For $J_2 > 0.5J_1$, $J(\mathbf{q})$ has minima at $(0, \pi)$ and $(\pi, 0)$. These correspond with the horizontal and vertical collinear states. However, these are not the only ground states in the classical picture and other ground states can be found by rotating all the spins of one sublattice with respect to the other. This costs no energy for classical spins at $T = 0$, but configurations where the staggered magnetizations of both sublattices are collinear are selected when introducing thermal or quantum fluctuations [23]. At $J_2 = 0.5J_1$, the classical ground state is highly degenerate and the minimized $\mathbf{q}$ runs along the edges of the Brillouin zone. In this situation eq. 5.2 can be rewritten as $\mathcal{H} = \text{cst} + J_2 \sum (S_1 + S_2 + S_3 + S_4)^2$, where the sum goes over all the square plaquettes in the system [23]. As long as the squared total spin of all the plaquettes is zero, the energy is minimized.
When looking at the states corresponding to (π, π) and $(\pi, 0)$ and using them as variational states for the Hamiltonian in eq. 5.1, the energies per site are $E_{\pi,\pi} = -J_1 + J_2$ and $E_{\pi,0} = -J_2$ respectively.

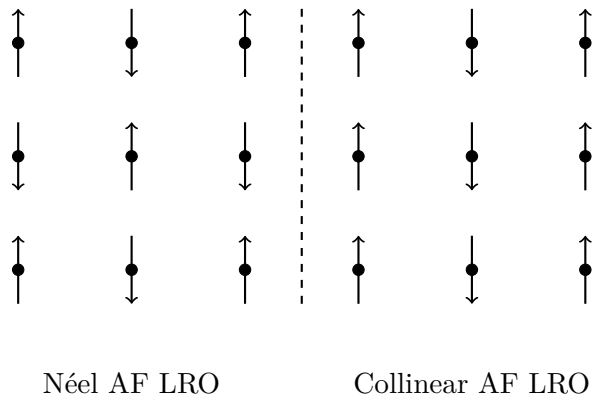

Figure 5.2: Classical depiction of the Néel antiferromagnetic long range order (left) and the collinear antiferromagnetic long range order in vertical direction (right)

A covering of dimers is also possible. Here we cover the lattice with first-neighbour singlets, i.e. every spin forms a singlet with one of its neighbours. In this completely *dimerized* state, the expectation value of the energy per site is given by $E_{\text{dimer}} = -3/4J_1$ when turning of interaction between dimers, which is below the two other states. This is clearly no longer a classical solution, but they suggest that the LRO solutions might not be the ground state solution in the whole J_2/J_1 domain for the quantum system. However it is not said which of these trial states will be lowered most by quantum fluctuations.

5.1.2 Néel AF LRO phase

It has been already long established that the $J_1 - J_2$ model exhibits a Néel AF LRO phase at low J_2/J_1. First of, we look at the classical Ising model equivalent for the square lattice with NN and NNN interactions. It is clear when NNN interactions are turned of that the ground state of the Ising model is given by a classical Néel antiferromagnetic ordered state. This is sketched in figure 5.2. However, when going from the classical system to the quantum system (with Heisenberg Hamiltonian), quantum fluctuations are introduced. These can possibly break the Néel AF ordered state and it is not immediately clear if this is also the ground state for the quantum system. In the late 80's and early 90's however, it became established that the antiferromagnetic Heisenberg model with nearest neighbour interaction on the square lattice shows a Néel AF order at $T = 0$ [50–53].
One of the most important properties that can suggest semi-classical ground state magnetic ordering are order parameters corresponding with the ordering at hand (so here Néel LRO). Following Schulz [54], we use the so-called $\mathbf{Q}$-dependent susceptibility

$$M_N^2(\mathbf{Q}) = \frac{1}{N(N+2)} \sum_{ij} \langle \mathbf{S}_i \cdot \mathbf{S}_j \rangle \, e^{i\mathbf{Q}(\mathbf{R}_i - \mathbf{R}_j)}, \tag{5.5}$$

where $\mathbf{Q}$ is the magnetic wave vector and is given by $\mathbf{Q}_0 = (\pi, \pi)$ for the Néel magnetic LRO. For $\mathbf{Q} = (0, 0)$ clearly this gives the squared total spin with a normalisation factor. Another

important property for Néel AF LRO is the so-called staggered magnetisation m_{stag}. This magnetisation is calculated by dividing the total lattice into two square sublatices. On one sublatice we measure $\hat{S}_z$, on the other $-\hat{S}_z$, and we average out. The sublattices are of course created in such way that the staggered magnetisation is the maximal value of $m_{\text{stag}} = \frac{1}{2}$ for the classical Néel AF state. This can of course be again expressed in function of the magnetic wave vector $\mathbf{Q}$. Due to the quantum fluctuations in the quantum system, the Néel AF order ground state will have a deviation of this maximal value. In the 50's this staggered magnetisation has been calculated by P.W. Anderson with spin-wave theory to be $m_{\text{stag}} = 0.303$ [50]. A perturbation expansion away from the Ising limit has been used by Huse in 1988 in ref. [51] and $m_{\text{stag}} = 0.313$ was obtained. Quantum Monte Carlo simulations in the late 80's and early 90's re-enforced these results and enlarged the recognition of the Néel AF ordered state in the J_1 model [52, 53].
Multiple calculations have shown that the order parameter for the Néel AF LRO survives for J_2/J_1-values up to approximately 0.4 and the LRO order is not yet destroyed by quantum fluctuations at these values. Most of the applied techniques use extrapolation to an infinite lattice. This has been done with for example DMRG [38], CCM [31] and exact diagonalization [19]. Earlier on, also spin wave theory [55], series expansions [56] and others, were used.

5.1.3 Collinear AF LRO phase

In section 5.1.1 we discussed the classical system and we showed that the ground state for $J_2/J_1 > 0.5$ was given by a magnetic wave vector $\mathbf{Q} = (\pi, 0)$ or $(0, \pi)$. An arbitrary global rotation of the spins of one of the sublattices with respect to the other sublattice gave no energy change in the classical ($S \to \infty$) limit. We noted however that the introduction of quantum fluctuations favours the states where the staggered magnetisations of the two sublattices is parallel and thus favours the horizontal or vertical collinear LRO phase as shown in the right side of figure 5.2. At large J_2/J_1 we can thus expect a *collinear AF LRO phase*. As expected, the characteristic order parameter is given by eq. 5.5 where $\mathbf{Q} = (\pi, 0)$ (or $(0, \pi)$).
However, it is also noted in section 5.1.1, that the order parameters disappear around $J_2/J_1 = 0.5$ and that even a possible dimerized state can be a better representation of the ground state around this point. The disappearance is again confirmed by simulations executed in, for example, DMRG [38], CCM [31] and exact diagonalization [19]. Also spin wave theory [55] and series expansions [56] provide the same results and show a phase transition at $J_2/J_1 \approx 0.6$ to the collinear LRO phase.

5.1.4 The nonmagnetic disordered intermediate region

Although the phases for small and large J_2/J_1 are well understood, the phase in the nonmagnetic disordered intermediate region is not. We have seen that the phase transitions to the

ordered states happen at $J_2/J_1 \approx 0.4$ and 0.6. The phase between these values is stills up to debate. Two different phases are in the running. First a valence bond state, like columnar valence bond crystals and plaquette states, was suggested, and this seems to be backed up by series expansions [24], large-N expansions [57], CCM [31] and PEPS [58]. However, DMRG [38] and spin-wave calculations [55] hint to a spin liquid state as intermediate state. For the interested reader, a good and more thorough description of these phases is given by C. Lhuillier in ref. [23].

Valence-bond crystals (VBC)

The VBC are the simplest way to overcome frustration in the quantum system. Here, neighbouring spins are arranged in singlets. Possible singlets are dimers, quadrumers or $2n$-mers, where $S = 0$ on the plaquette. Its stability originates from the stability of the $(S = 0)$-plaquette clusters individually. We recall that for example the singlet of two spin-1/2 (thus a dimer) has an energy of $-3/4$ in the AF case, while the energy of two classical spins opposite only has an energy of $-1/4$. In the VBC, there is no $SU(2)$ symmetry breaking (in contrary to the ordered LRO states). Furthermore, spin-spin correlations are not long-range, but singlet-singlet correlations (correlations between the plaquettes) are.
We now distinguish two kinds of VBC, *spontaneous* VBC and *explicit* VBC. In spontaneous VBC the wavefunction breaks the lattice symmetry spontaneously and enlarges the unit cell of the lattice, while in explicit VBC this does not happen. Explicit VBC can occur when the Hamiltonian has inequivalent bonds and an integer spin in the unit cell (e.g. an even number of spin-1/2). Then the VBC-solution can take advantage of the stronger of the inequivalent bonds to form its singlets. Here the explicit VBC is the intuitive strong-coupling solution. Now we look at the strong-coupling limit. When we turn off the weak coupling (i.e. the coupling between different singlets), the exact solution of the Hamiltonian is given by the product of the different singlets. Furthermore, the original lattice symmetry is clearly preserved. When we now look at models where the unit cell has a non-integer number of spin (e.g. an odd number of spin-1/2), then the VBC cannot be realized without enlarging its unit cell *spontaneously*. In this case the singlet covering is not unique and a symmetry breaking in the lattice symmetry occurs to form a VBC and the VBC is thus degenerate.
Clearly the possible valence-bond crystal in the square $J_1 - J_2$ model would be of the spontaneous type, since covering of singlets cannot occur without lattice symmetry breaking. The VBC under consideration in this model are the *columnar* and *staggered* dimer VBC. Numerical evidence at the moment favours the columnar VBC over the staggered VBC [59].

Resonating Valence Bond (RVB) spin liquid

In 1973 P.W. Anderson introduced the Resonating Valence Bond Spin Liquid in ref. [60]. Anderson was inspired for this RVB spin liquid by Paulings *resonating valence bond* theory

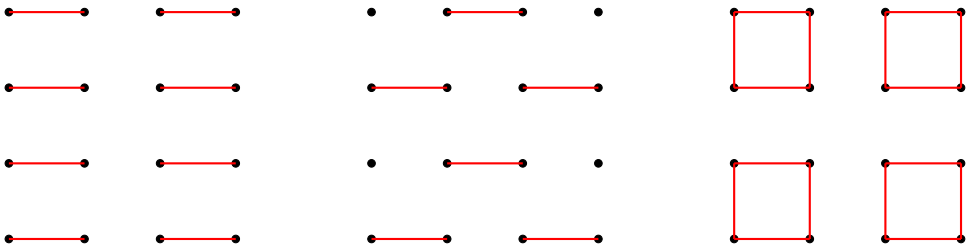

Figure 5.3: Columnar (left), staggered (middle) dimer VBC and plaquette (right) RVB on the square lattice

of metals, where the electron gas nature of the metallic state was ignored and the binding energies were related to valence bond concepts. Anderson compares the Néel state to a solid, where the system has condensed into a spin lattice, while the RVB spin liquid has mobile valence bonds. These valence bonds are pairs of spins correlated together into singlets (for example dimers). He further speculated that the system became energetically more favourable through quantum resonances between the great number of possible dimer coverings. Any long range-order (also singlet-singlet correlation) is absent, hence the name spin *liquid*.
We now look at the complete set of possible dimer coverings (not restricted to the length of the dimers). This is an overcomplete basis of the $S = 0$ subspace [23]. So now, let us assume we instead created a family $\mathcal{E}$ of linearly independent dimer coverings $\mathcal{C}_i$, then a RVB wave function can be written as:

$$|\text{RVB}\rangle = \sum_{\mathcal{C}_i \in \mathcal{E}} A(\mathcal{C}_i) \, |\mathcal{C}_i\rangle \tag{5.6}$$

Here $|\mathcal{C}_i\rangle$ are of course products of the different singlet wave-functions. Most of the time in variational calculations, the amplitude $A(\mathcal{C}_i)$ is given by a product of amplitudes $h(k,l)$ for each dimer (k,l) in the valence bond state $\mathcal{C}_i$. Long range RVB wave functions are given when $h(k,l)$ is algebraically dependent on the distance r_{kl}:

$$h(k,l) = \frac{\text{Cst}}{r_{kl}^{\sigma}} \tag{5.7}$$

These long-range RVB wave functions can represent Néel long range order in the Heisenberg model on the square lattice if $\sigma < 5$.
On the other hand, short-range RVB wave functions are given when the amplitudes decrease at least exponentially with the distance between k and l (and thus also if only nearest neighbour dimers are included). Obviously this wave function cannot represent Néel long range order, since Néel has long range correlations between spins. The valence bond crystals can be seen as a short-range RVB where one amplitude $A(\mathcal{C}_i)$ dominates. However, it is also possible to choose the amplitudes in such way that lattice symmetry is conserved in the wave function. RVB wave functions where there is no lattice symmetry breaking (and also no $SU(2)$ symmetry breaking) are the *pure* RVB spin liquids. When referring to quantum spin liquids,

we mean these wave functions that resist $SU(2)$ and lattice symmetry breaking even at zero temperature.
An RVB that is no pure spin liquid is given by the plaquette RVB. This RVB is sketched schematically in figure 5.3 on the right. This RVB restores the rotational symmetry of the lattice but there is clearly still a translational symmetry breaking and hence this is no spin liquid. Here the plaquettes resonate between dimers ordered horizontally and vertically, thus the wave function of such plaquette is given by:

$$|\square\rangle = ||\,|\rangle \pm |=\rangle\,, \tag{5.8}$$

where $||\,|\rangle$ and $|=\rangle$ are the product of two dimers in respectively vertical and horizontal direction.

Current results on the nonmagnetic intermediate region

Currently, there is still discussion about the nature of the nonmagnetic intermediate region in the thermodynamic limit ($N \to \infty$). Whether it is a lattice symmetry breaking columnar dimer VBC or plaquette RVB or a symmetry preserving spin liquid is not yet clear. Different investigations point to different directions, due to the bias of the used method or due to the small system size that can be treated at the moment. In contrast to the $J_1 - J_3$ model on the square lattice and the $J_1 - J_2$ model on the hexagonal lattice, the spin-spin correlations of the $J_1 - J_2$ model on the square lattice in this region are not short-range enough to effectively represent the bulk at the current attainable system sizes, thus hindering the examination of the phase in bulk [25].
In ref. [58] Murg *et al.* discussed the $J_1 - J_2 - J_3$ model with the PEPS algorithm. In this paper, the exact diagonalization in the short-range valence bond states (SRVB) subspace is calculated. Overlap between the PEPS and SRVB solution is investigated, and a maximum overlap of 70% is found at $J_2/J_1 = 0.5$. Since the PEPS ground state energy is also lower than the SRVB ground state energy, it is clear that the true ground state will not be completely in the SRVB subspace, but a large overlap can still be expected. In the PEPS calculations there is also faint evidence for a columnar dimer state as seen in figure 12 of ref. [58]. In ref. [31] several generalized susceptibilities are calculated through CCM and exact diagonalization (ED). The divergence or enhancement of the susceptibilities corresponding with the columnar dimer VBC and the plaquette RVB show evidence in favour of these states and thus spatial symmetry breaking occurs.
In ref. [38] DMRG calculations are used to support the idea of a quantum spin liquid (QSL) with no spatial symmetry breaking. The dimer order parameter and plaquette order parameter are calculated for different system sizes and extrapolated to the thermodynamic limit. The results obtained show a vanishing dimer and plaquette order parameter for all J_2/J_1. Also bulk excited states are extracted and the first singlet and triplet excited state are found

gapped for the intermediate nonmagnetic phase. Furthermore, they calculate the entanglement entropy $S(A)$. The system is divided into two subsystems A and B, and the reduced density matrix $\rho_A = \mathrm{Tr}_B \left|\psi_0\right\rangle \left\langle\psi_0\right|$ is calculated. Now the entanglement entropy is defined as $S(A) = \mathrm{Tr}_A(\rho_A \ln \rho_A)$. For systems with gapped bulk excitations and a smooth boundary between the two subsystems A and B, the entanglement entropy scales as follows:

$$S(A) \sim \sigma L - \gamma + \cdots . \tag{5.9}$$

This is known as the area law, where L is the length of the boundary between the subsystems. σ is a measure for the local entanglement across the boundary and the omitted terms vanish with large L. In ref. [38] it is further argued that two scenarios can cause a non-zero constant term γ. It is possible to have a topological contribution that decreases the entropy (thus positive γ) or a symmetry-breaking origin that increases the entropy. Their calculations find a $\gamma = 0.72 \pm 0.04$ extrapolated to the thermodynamic limit, and thus suggesting a topological origin and not a symmetry-breaking origin. A symmetry-preserving spin liquid can be the origin of this constant decrease in the entropy.

5.2 Result of the cluster DMET calculations

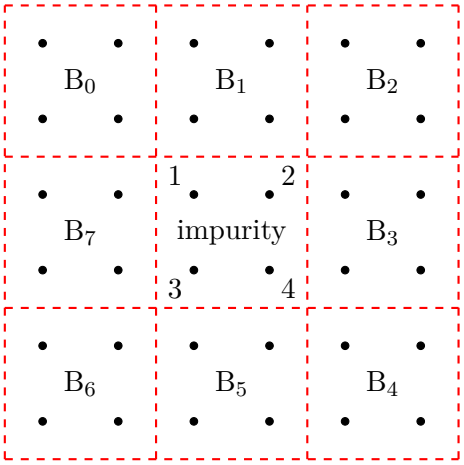

Figure 5.4: Division of a 6×6 square lattice into 8 bath clusters and one impurity cluster of size 2×2. The spins of the impurity cluster are also numbered.

In this section the results of the cluster DMET algorithm on the $J_1 - J_2$ model will be discussed. First, the main results of the original cluster-DMET paper (ref. [13]) will be reproduced, including the total energy per spin and the entanglement entropies (figures 2 and 4 in ref. [13]). Furthermore, we will calculate several other properties and try to detect the different phases in the model, with most importantly the intermediate nonmagnetic phase.
We will investigate the 8×8 square lattice with periodic boundary conditions. The lattice is divided into 16 equivalent 2×2-clusters (an exemplar division is shown in figure 5.4 for a 6×6

spin system). One of these clusters is chosen as impurity. Since all the clusters are equivalent, the DMET solution can be mapped throughout the lattice. The convergence criterion for the cluster DMET algorithm is given by the convergence of the DMET-energy, i.e. the energy per spin calculated within the DMET framework. For the total energy of the system eq. 4.12 is used and not the total energy λ given in eq. 4.9. Energies *per spin* are presented in the plots. The convergence criterion is satisfied at $\left|\frac{E_{\text{old}}-E_{\text{new}}}{E_{\text{new}}}\right| < 10^{-7}$ for our calculations.

The initialisation of the DMET algorithm can happen in several manners and since the DMET algorithm can converge to local minima, the obtained converged solution is dependent of the initialisation of the problem. To test how big a problem the optimization to local minima can be, 40 calculations with random initialisation at every 0.05 interval of J_2/J_1 are executed. The calculations converged in maximally 10^3 iterations. The results are shown in figure 5.5. The DMET-energy per spin, the λ-energy per spin, the normalized Néel order parameter, and the normalized collinear order parameter are shown. The order parameters are given by eq. 5.5 with $\mathbf{Q} = (\pi, \pi)$ for the Néel order parameter and $\mathbf{Q} = (\pi, 0)$ or $(0, \pi)$ for the collinear order parameter. For the collinear order parameter, we note that collinearity can be in horizontal and vertical direction and with every found ground state, one will be large and the other small in the collinear phase. Here we plot only the largest of the two collinear order parameters for every simulation, which is also the useful one to detect the phase transition. When looking at the DMET-energy, we see that most calculations converge to the same value with some exceptions (e.g. in the region with J_2/J_1 from 0.15 up to 0.6 there are two minima the algorithm converges to). At values between 0.6 and 0.8, we see that the lowest DMET-energy value is not always the most often found solution. Selecting the right ground state can happen by selecting the lowest DMET-energy or the lowest λ-value. In figure 5.5 there is no ambiguity yet, but in further results it will be shown that the lowest DMET-energy does not always correspond with the lowest λ-value found and vice versa. From the plotted order parameters its is also clear that the calculations converge to quite different wave functions for J_2/J_1 between 0.6 and 0.8. This is visible in the great differences in the values of the order parameters.

In the next step we try to solve these problems by using *sweeps*. We notice at maximal and minimal NNN interaction that the calculations do not show such a large variety of local minima. Now by starting a first calculation at $J_2/J_1 = 0\,(1)$, and using the converged result as initialisation for the next calculation right (left) on the J_2/J_1-axis, we bias the calculation to converge in a similar state. By repeating this step in the right (left) direction we perform a *right (left) sweep*. This could solve continuity problems obtained with random initialisation and mitigate getting stuck in local minima.

The results of the left and right sweep are presented in figure 5.6 together with the results of the random initialisation. As can be seen readily, the sweeps have found more optimal states for the DMET-energy and the λ-value, especially in the troublesome region given between $J_2/J_1 = 0.6$ and 0.8.

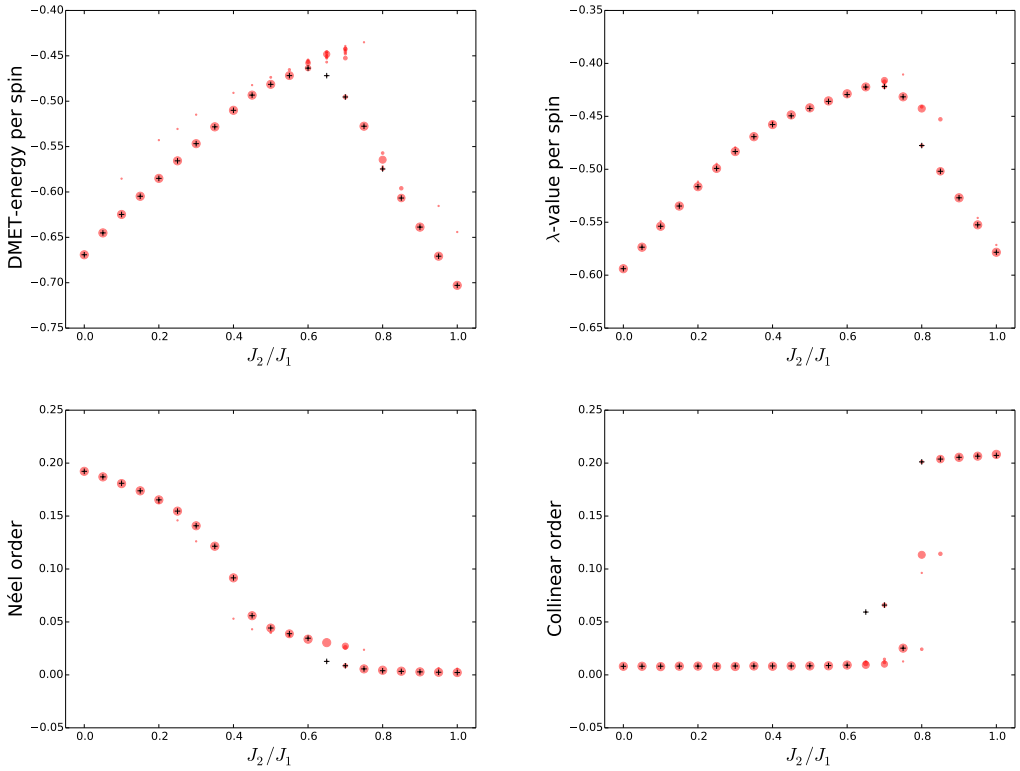

Figure 5.5: Calculations executed with random initialisation. The size of the markers scale with the number of calculations that yielded the corresponding value. Top left is the DMET-energy per spin, top right is the λ-value divided by number of spins. Bottom left is the Néel order parameter, bottom right is the collinear order parameter. The + markers represent the solutions with the lowest DMET-energy (and also the lowest λ-value).

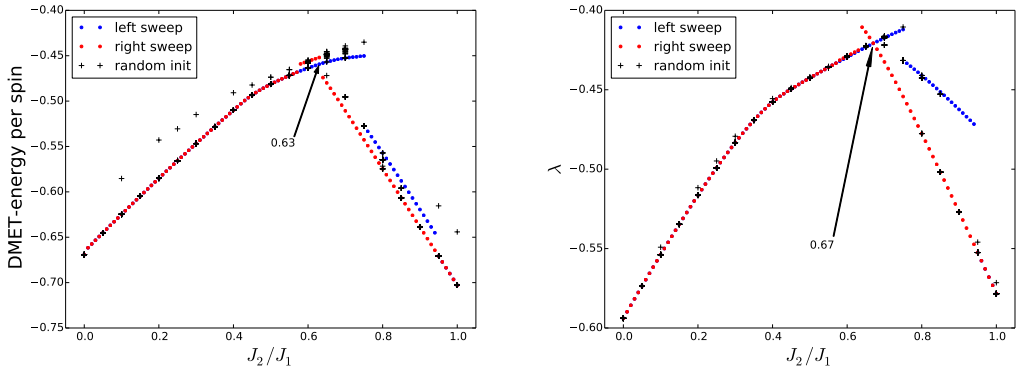

Figure 5.6: Results for the DMET-energy and λ-energy per spin for the left and right sweep and the random initialisation.

Some ambiguity in the selection of the ground state starts to arise. New solutions with more optimal DMET-energy and λ-values are found through left and right sweep. When executing the left sweep, we see in figure 5.6 that the solution found is clearly a local minimum from ≈ 0.6 onwards and a more optimal solution is found by the right sweep. However, the transition where the right sweep solution gets more optimal than the left sweep depends on the method of selection of the optimal state. In figure 5.6, one can see that this transition happens at $J_2/J_1 \approx 0.63$ when selecting on DMET-energy grounds, but when selecting on λ-value grounds, this transition happens at $J_2/J_1 \approx 0.67$. In the original paper of Fan [13], selection happens through choosing the minimal DMET-energy per spin. This way, a more continuous DMET-energy plot is found. There is however still a small energy jump at $J_2/J_1 = 0.63$, and when extrapolating the straight trend of the DMET-energy in the interval $J_2/J_1 \in [0.64, 1]$, the maximum of the DMET-energy would be expected at 0.62 approximately. It is possible that these solutions are not found since the λ-values corresponding with them are too large in comparison with the absolute minimum of the λ-values. The results with the optimal selected DMET-energies are given in figure 5.7. The obtained results for the DMET-energy per spin are the same as the ones found in ref. [13]. We see also a good qualitative correspondence with the results of the exact diagonalization in ref. [19] of the 40 spin lattice. The energy per spin exhibits a maximum around $J_2/J_1 = 0.63$. The energies for the exact diagonalization are however a bit lower, possibly because of the smaller system studied. Exact diagonalization of a 32 spin system has also been executed in ref. [31], here the energy per spin exhibits also the same qualitative behaviour, but the energies are even lower due to the even smaller system size.

When looking at the order parameters, we see the expected behaviour. In the low NNN interaction regime, Néel order is detected while in the large NNN interaction regime collinear order is detected. In fig. 2 in ref. [38], the order parameters obtained through DMRG for different system sizes are plotted, with $L \times 2L$ system sizes. This makes direct quantitative comparison not possible. Despite the different geometries, we see qualitative correspondence. We see that DMET has a steeper Néel order breakdown at the expected phase transition at $J_2/J_1 \approx 0.4$, even at finite system sizes. Some Néel order however survives in the non-magnetic intermediate phase, which is not the behaviour we have hoped for. This is due to the finite system size, DMRG calculations and exact diagonalizations have also non-vanishing order parameters in the intermediate nonmagnetic phase on finite lattices. There is also a steep increase of collinear order at approximately 0.62. This is again in correspondence with the exact diagonalization of ref. [19] and the DMRG-solution in ref. [38]. The maximal collinear order obtained in these results is a lot smaller than our obtained value. A possible explanation for this is the degeneracy of the ground state in the collinear phase. Collinear order can happen horizontally and vertically, and both results are equally favourable. In the exact diagonalization and DMRG calculations, it is possible that a superposition of these two orders is found as ground state. For the cluster DMET solution, it is found that only one

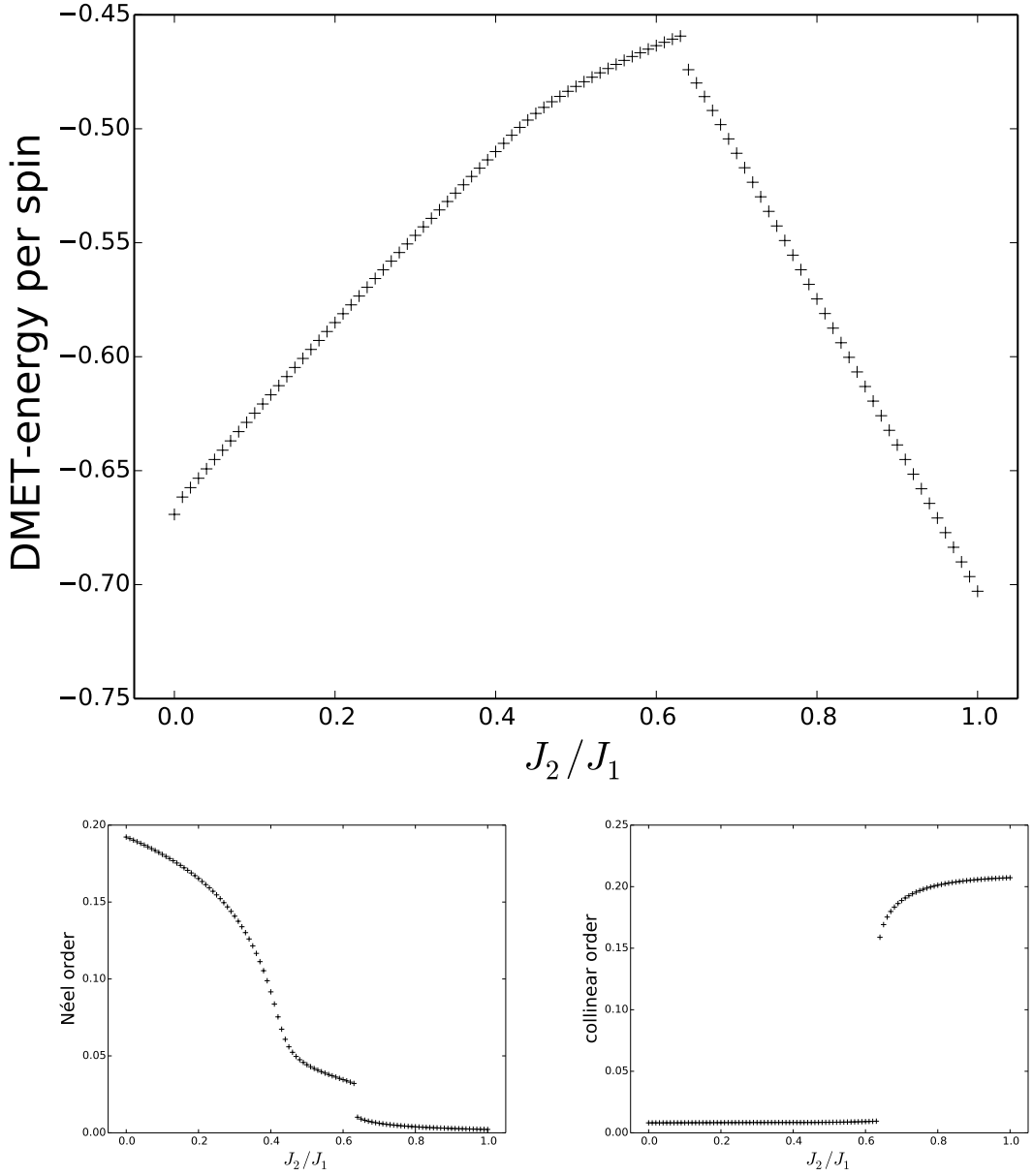

Figure 5.7: Properties for the optimal solutions selected through minimal DMET-energy. Top is the DMET-energy, bottom left is the Néel order parameter, bottom right is the collinear order parameter.

collinear order parameter in one direction is large while the other stays negligibly small. The DMET algorithm finds a ground state with collinear order dominant in one direction and no mixing of the two directions.

Last, different Von Neumann entropies are calculated in correspondence with ref. [13]. The Von Neumann entanglement entropy is a measure for the entanglement between two subsystems A and B. The total system is divided into two subsystems A and B. The reduced density matrix $\rho_A = \mathrm{Tr}_B \left|\Psi_0\right\rangle \left\langle\Psi_0\right|$ is calculated by tracing out the subsystem B. The Von Neumann entropy is now defined by

$$S(\rho_A) = -\,\mathrm{Tr}(\rho_A \ln \rho_A). \tag{5.10}$$

The subsystem A is chosen to be one or multiple spins in the impurity. The entanglement entropy is given in figure 5.8. These are the same results as obtained by ref. [13], and according to this article, a discontinuity in the entanglement entropy indicates a first-order quantum phase transition, while a peak in the derivative of the entanglement indicates a continuous quantum phase transition. From figure 5.8, a first order quantum phase transition is thus visible at $J_2/J_1 \approx 0.6$ and a continuous quantum phase transition is visible at $J_2/J_1 \approx 0.4$. From these results, the C_4 symmetry breaking of the ground state is visible in the collinear LRO phase. $S(\rho_{12})$ and $S(\rho_{13})$ are equivalent for the rotationally symmetric solution, and it is visible that they preserve this rotational equivalence up to the phase transition at $J_2/J_1 =\approx 0.63$. From this point onward, their equivalence is lifted and rotational symmetry is broken, as expected in the collinear LRO phase.

The choice of a 2×2-impurity will show bias towards the columnar dimer VBC and the plaquette RVB, while being less biased towards a staggered dimer VBC. Between the two dimer VBC coverings, previous numerical evidence has shown favour towards the columnar dimer VBC [59], thus this negative bias towards staggered dimer VBC should impose no problem. The fact that rotational symmetry is not yet broken in the nonmagnetic phase within the DMET-framework, is proof against the existence of a dimer VBC, since this breaks rotational symmetry and is evidence in favour of a plaquette RVB or a spin liquid. Finally, according to ref. [13], there is also some evidence towards a weak plaquette RVB. From figure 5.8, we see that the entanglement between impurity and bath ($S(\rho_{1234})$) decreases from $J_2/J_1 \approx 0.4$ onward, although the other entanglement entropies increase in this regime. This increase of the other entropies should thus explain a large increase of entanglement between the spins in the impurity itself, while impurity-bath entanglement decreases. This suggests a plaquette valence bond. However, since the survival of Néel order has been detected in this phase (fig. 5.7), which is unwanted in the nonmagnetic phase, it is clear that the 8×8 square lattice is not sufficient to represent the bulk square lattice in this phase. Hence, it is not clear in which extent conclusions can be made from entanglement entropy results in this region.

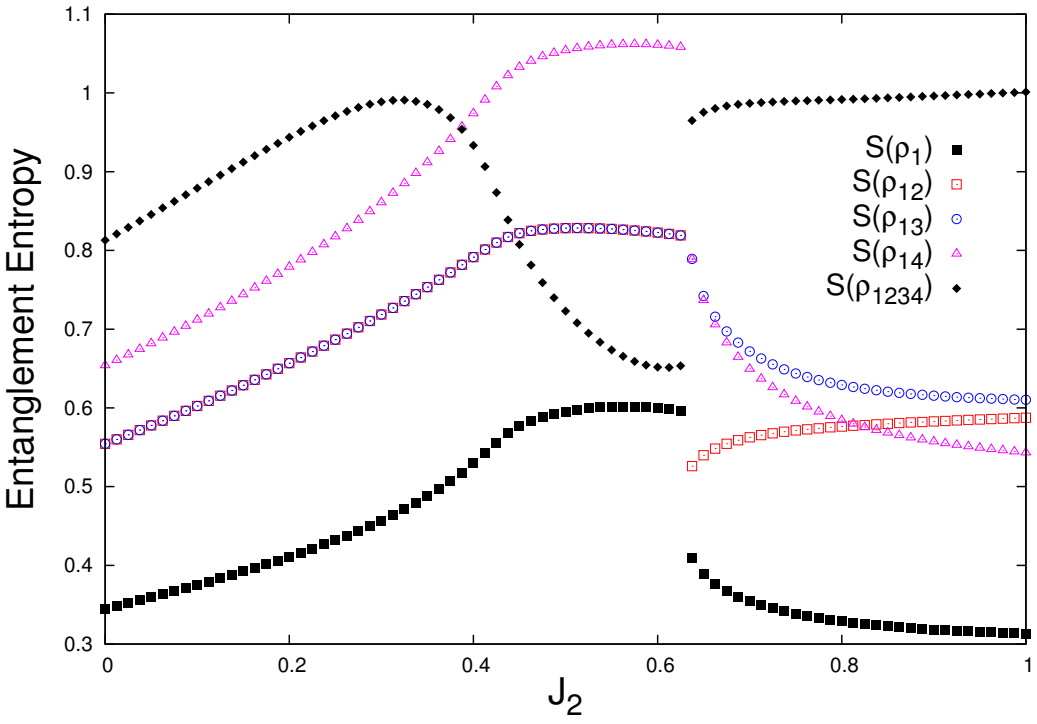

Figure 5.8: Different Von Neumann entanglement entropy for the DMET-solutions. The subsystem A is chosen as one or multiple spin sites of the impurity. The subscripted numbers denote which spin sites are part of subsystem A. The numbering of the spins is done cfr. figure 5.4

5.3 The spectral function

In section 4.3, a method for the calculation of the spectral function within the DMET framework is given. A corresponding implementation was developed. However, the calculation of $\left\langle \frac{\partial \Psi_1}{\partial \mathrm{pm}^*} \middle| \hat{H}^2 \middle| \Psi_1 \right\rangle$ in eq. 4.20 is very time consuming. Optimization of the code is still needed for the efficient calculation of spectral functions for meaningful system sizes.
For the verification of the implementation, a 2×4 square lattice with NN interaction ($J_2 = 0$) is studied. The spectral function is given by

$$A(\omega) = -\frac{1}{\pi} \Im[G(\omega, \hat{X})], \tag{5.11}$$

where $G(\omega, \hat{X})$ is given by eq. 4.14. Here, we will calculate the spectral function with $\hat{X} = \hat{S}^+$ and $\eta = 0.01$. This spectral function can be easily calculated through exact diagonalization for such small system sizes. The DMET algorithm for the calculation of the spectral function is also executed. For the execution of DMET, the 4×2 square lattice is split up into two equivalent 2×2 clusters. As shown in section 4.4, the DMET algorithm is able to find the exact results when only one bath cluster is present. An exact correspondence with the exact diagonalization, within a small error due to the imposed convergence criterion, is indeed observed as can be seen in fig. 5.9. We notice three large peaks and three very small peaks. The values of these peaks correspond, as expected, with excitation energies of the system, which can be calculated quite easily through exact diagonalization. It is observed that the rate of convergence slows down when approaching a peak. This and the fact that the calculation of the $\left\langle \frac{\partial \Psi_1}{\partial \mathrm{pm}^*} \middle| \hat{H}^2 \middle| \Psi_1 \right\rangle$ in eq. 4.20 is quite time consuming are the largest problems for the calculation of the spectral function within the DMET framework. Data for the spectral function through DMET are clearly incomplete in fig. 5.9 due to the lack of optimization of the code at this moment.

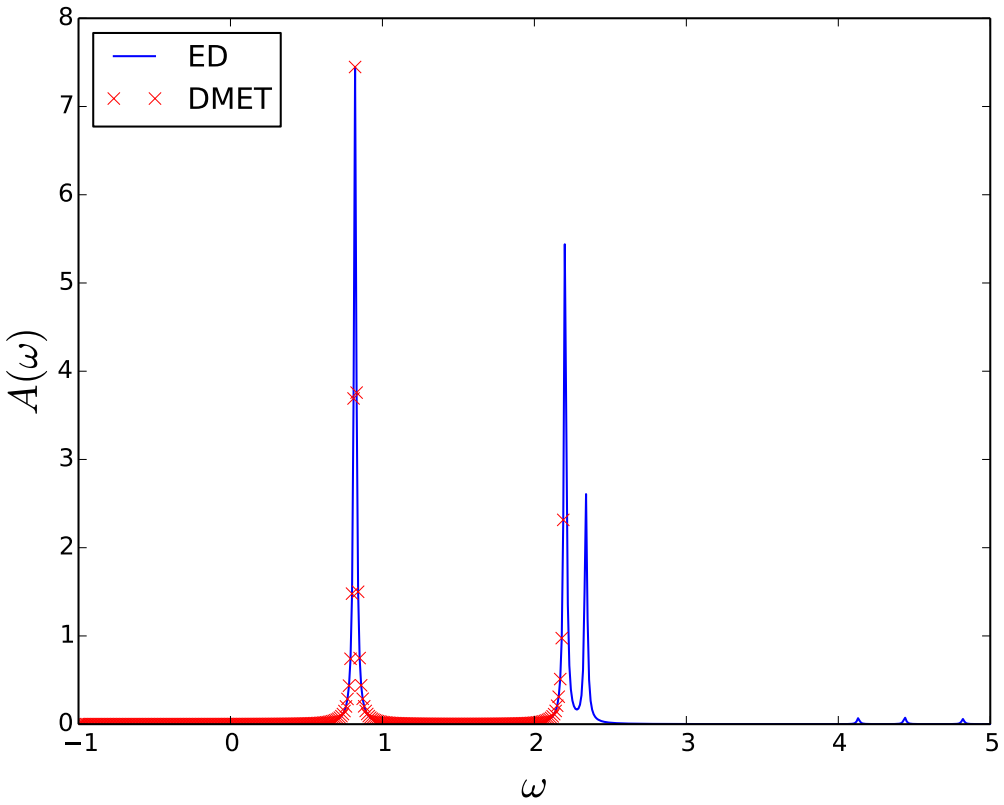

Figure 5.9: The spectral function for a 2×4 square lattice with NN interaction. The full line are the results obtained through ED, the crosses are the results obtained through DMET.

6 The Kitaev-Heisenberg model on the honeycomb Lattice

6.1 The Kitaev model

Spin-liquid states have been quantitatively studied by Kitaev through the introduction of an exactly solvable model [61]. This so-called Kitaev model treats interacting spins ($S^z = \pm 1/2$) on a honeycomb lattice. The nearest-neighbour interactions are Ising-like, meaning every bond depends on only one spin component. However, the spin component changes with different bonds, as can be seen in figure 6.1a. This introduces frustration in the model. The Hamiltonian for the Kitaev model is as follows:

$$\hat{H} = -J_{xx} \sum_{x-\text{links}} \hat{S}_j^x \hat{S}_k^x - J_{yy} \sum_{y-\text{links}} \hat{S}_j^y \hat{S}_k^y - J_{zz} \sum_{z-\text{links}} \hat{S}_j^z \hat{S}_k^z, \tag{6.1}$$

where J_{xx}, J_{yy} and J_{zz} are model parameters which denote the bond strengths. Depending

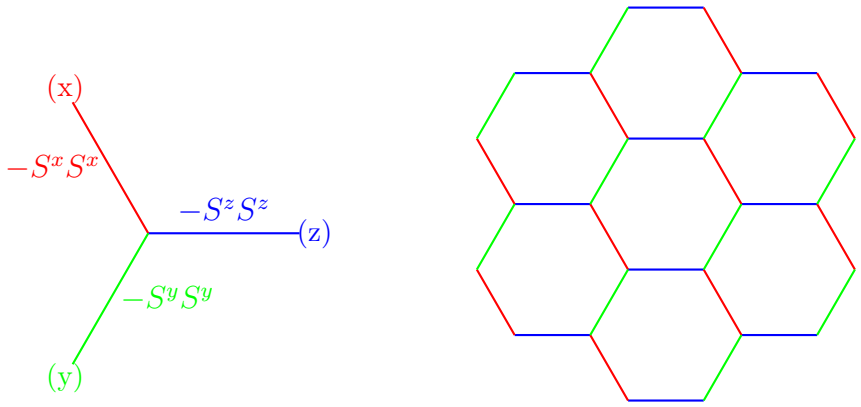

(a) The different bond types in the honeycomb lattice for the Kitaev model.

(b) The Kitaev Honeycomb lattice for 24 spins

on the values of the system parameters (J_{xx}, J_{yy} and J_{zz}) the model exhibits different phases [61]. In figure 6.2 the phase diagram of the $J_{xx} + J_{yy} + J_{zz} = 1$ plane in the first octant (i.e. all parameters positive) is given. A_x, A_y and A_z are gapped phases carrying abelian anyons while B is a gapless phase carrying non-abelian anyons.

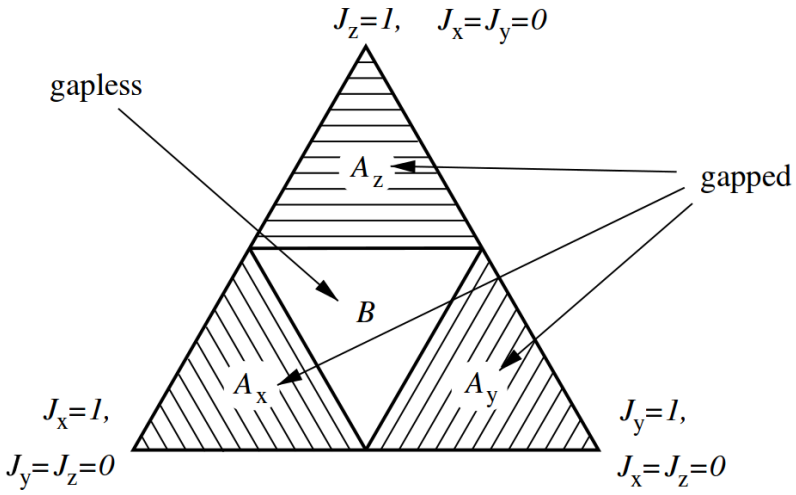

Figure 6.2: Phase diagram of the Kitaev model in the $J_{xx} + J_{yy} + J_{zz} = 1$ plane in the first octant [61]

.

In the gapless phase, this model has a spin-disordered ground state according to ref. [61]. It has also been shown that spin-spin correlation vanishes for this model for all spins separated by more than one lattice constant [62]. This extremely short-range correlation of the Kitaev model suggests a form of stability of the disordered ground state when applying spin perturbations. When the Kitaev model is perturbed with an isotropic Heisenberg exchange, it has been shown by Tsvelik that the spin liquid state remains stable for a small window of perturbation strengths [20]. Exact diagonalization and the spectrum of this Kitaev model is given in ref. [61, 62].

This model is useful due to the emergence of abelian and non-abelian anyons depending of the model parameters [61]. These particles are useful for *topological quantum computing*. It has been shown that universal quantum computing is possible with the aid of certain types of non-abelian anyons [63–65]. Furthermore, excitations that are abelian anyons imply a degeneracy of the ground state on the torus [66]. There arises a *topological order* for the ground state in this model. Due to the high quantum entanglement and the non-local encoding, storage of quantum information is immune to errors caused by local perturbations [65]. The search of physical realisations is difficult but highly attractive due to its usefulness. One way to engineer this Kitaev model is suggested by Jackeli and Khaliullin through the use of Mott insulators [67].

6.2 The Kitaev-Heisenberg model

The Kitaev-Heisenberg model is built up by mixing the Kitaev and the Heisenberg model, as the name suggests. From now on we assume that the bond strengths in eq. 6.1 are equal for

all different bonds and are given by J_1, thus fixing the phase of the pure Kitaev model in the gapless phase. The Hamiltonian for this system is given by

$$\hat{H} = -J_1 \sum_{x-\text{links}} \hat{S}_j^x \hat{S}_k^x - J_1 \sum_{y-\text{links}} \hat{S}_j^y \hat{S}_k^y - J_1 \sum_{z-\text{links}} \hat{S}_j^z \hat{S}_k^z + J_2 \sum_{\langle jk \rangle} \hat{\mathbf{S}}_j \cdot \hat{\mathbf{S}}_k, \tag{6.2}$$

where the first three terms are clearly the Kitaev interaction, and the last term is the Heisenberg interaction between nearest neighbours. We assume that J_1 and J_2 are positive and therefore we have an antiferromagnetic Heisenberg interaction. The interaction between two neighbouring spins is given by

$$\hat{H}_{ij}^{(\gamma)} = -J_1 S_i^\gamma S_j^\gamma + J_2 \hat{\mathbf{S}}_i \cdot \hat{\mathbf{S}}_j, \tag{6.3}$$

where γ is given by x, y or z depending on the bond. The bond type is again given in the same way as the pure Kitaev model and is depicted in figure 6.1a. Chaloupka, Jackeli and Khaliullin opted to use this model for the theoretical examination of iridium oxides of the form $A_2\text{IrO}_3$, with A = Li, Na [20]. Herein, Ir^{4+} ions form honeycomb-like lattice planes and have an effective spin one-half moment. According to ref. [20], the interaction consists of a ferromagnetic Kitaev and an antiferromagnetic Heisenberg part, of the form of eq. 6.2. Depending on the parameters of the iridium oxide crystal, the Hamiltonian varies between a purely antiferromagnetic Heisenberg Hamiltonian and a pure Kitaev Hamiltonian. The high anisotropy (the Kitaev part of the interaction) of the coupled spin-orbit angular momentum arises since this is predominantly of orbital origin [20].
The couplings are now parametrized as $J_1 = 2\alpha$ and $J_2 = 1 - \alpha$ cf. ref. [20]. When varying α between 0 and 1, different phases occur. It is clear that at $\alpha = 0$ the system is reduced to an AF Heisenberg system, which exhibits a Néel order [68]. At the limit $\alpha = 1$ the system is reduced to the exactly solvable Kitaev-model. Here the system has a spin liquid ground state with short-range spin-spin correlations, as said in section 6.1. Intermediary, at $\alpha = 1/2$, the system is also exactly solvable as shown by Khaliullin [69]. The bond interaction (eq. 6.3) for $\gamma = z$, for example, is now reduced to

$$\hat{H}_{ij}^z = \frac{1}{2}(\hat{S}_i^x \hat{S}_j^x + \hat{S}_i^y \hat{S}_j^y - \hat{S}_i^z \hat{S}_j^z). \tag{6.4}$$

To find the exact solution at $\alpha = 1/2$, a mapping of the anisotropic Hamiltonian to an isotropic ferromagnetic Heisenberg Hamiltonian is executed through appropriate rotations of the spin operators. To complete this rotation, one has to work in a super-cluster of 24 spins and divide it in 4 different sublatices (see figure 6.3). We now rotate the spin operator $\hat{\mathbf{S}}$ differently on every sublattice. A possible rotated spin operator $\hat{\tilde{\mathbf{S}}}$ is for example given in figure 6.3. In terms of these rotated spin operators eq. 6.3 becomes:

$$\hat{H}_{ij}^{(\gamma)} = -2(2\alpha - 1)\hat{\tilde{S}}_i^\gamma \hat{\tilde{S}}_j^\gamma - (1 - \alpha)\hat{\tilde{\mathbf{S}}}_i \cdot \hat{\tilde{\mathbf{S}}}_j, \tag{6.5}$$

where J_1 and J_2 are substituted by their parametrized value in α. It is clear that at $\alpha = 1/2$ eq. 6.5 reduces to the bond interaction of a ferromagnetic system. The system thus reduces

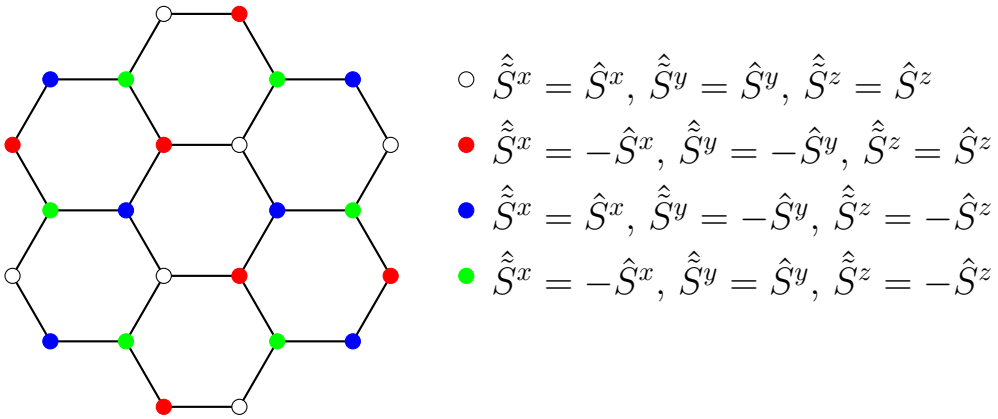

Figure 6.3: Division of the honeycomb supercluster of 24 spins in 4 sublatices.

to a simple ferromagnetic Heisenberg Hamiltonian in the rotated spin operators. Its ground state has a maximal total spin $\tilde{S}_{\text{tot}} = NS = \frac{N}{2}$ and is $(2NS+1)$-fold degenerate. We note that the total rotated spin $\tilde{S}_{\text{tot}}$ is not a constant of motion, except when $\alpha = 1/2$.
To study the ground state in the unrotated basis we look at one of these $N+1$ ground states, for example where $\left\langle \hat{\tilde{S}}^z \right\rangle = \frac{1}{2}$. This gives in the unrotated basis a stripy antiferromagnetic phase as depicted in figure 6.4. We note that the stripy antiferromagnetic phase is the exact

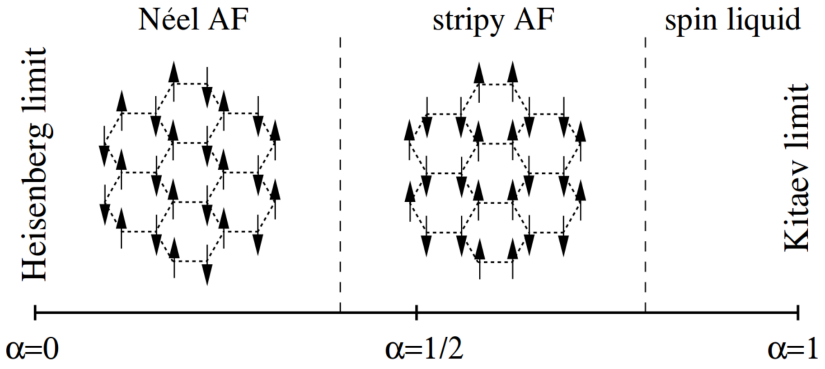

Figure 6.4: A schematic phase diagram for the Kitaev-Heisenberg model [20].

ferromagnetic phase in the rotated basis, and thus in this basis has maximal total spin. The stripy AF order parameter is thus fully saturated at $\alpha = 1/2$ and the phase is fluctuation free, despite being of AF-type.
From this discussion it is clear that the Kitaev-Heisenberg model has at least three phases on the Honeycomb lattice. At $\alpha = 0$, we have an anti-ferromagnetic Néel ordered phase, at $\alpha = 1/2$ we have a second ordered state, a stripy antiferromagnetic phase, and finally, at $\alpha = 1$, we have a disordered spin liquid phase. These phases are sketched in figure 6.4.
First, we look at the classical system. The energy per spin is for the Néel AF state $E = -\frac{3}{8} + \frac{5}{8}\alpha$, while the energy per spin for the stripy AF state is given by $E = -\frac{1}{8} - \frac{1}{8}\alpha$. The

phase transition thus happens at $\alpha = \frac{1}{3}$. However, when going to the quantum mechanical system, and introducing quantum fluctuations, the phase transition moves to a larger α-value. Second-order perturbation theory gives an estimate for the Néel energy of $e_1 \approx -\frac{3}{16}(3 - 5\alpha)$ and for the stripy energy an estimate of $e_2 \approx -\frac{1}{8}(5\alpha - 3 + \frac{1}{\alpha})$ per spin [20]. For the derivation of these results, see appendix B. From this, it is clear that the boundary shifts to larger α-values ($\alpha \approx 0.4$) compared to the classical phase boundary. The quantum fluctuations have a stabilizing effect on the Néel AF state [20]. This value is in correspondence with the results obtained from the exact diagonalization of a 24 spin lattice. However, series expansion executed on the Kitaev-Heisenberg model suggest a phase transition at $\alpha = \frac{1}{3}$ [70].

Second, we look at the phase transition from stripy AF to the spin liquid. Both the anisotropic and the Heisenberg interactions are purely ferromagnetic in the rotated basis at $\alpha \geq 0.5$ (see eq. 6.5). Because of this, the only ordered state that can compete with the spin liquid state is the stripy AF state (or the ferromagnetic state in the rotated basis). Furthermore, we know that the exact solution of the pure Kitaev-model is stable under small Heisenberg perturbations, so there has to be a phase transition from stripy AF to the spin liquid at $\alpha < 1$. To estimate the phase transition point, we use again second order perturbation energy for the stripy AF phase. For the spin liquid, the energy per spin is approximated by taking $\left\langle \hat{S}_i^\gamma \hat{S}_j^\gamma \right\rangle = 0.13$ and the other correlations are equal to zero, which is the exact solution at $\alpha = 1$ [20]. Using these expectation values gives us $e_3 \approx \frac{3}{2}(1 - 3\alpha) \left\langle \hat{S}_i^\gamma \hat{S}_j^\gamma \right\rangle$ and thus a phase transition between spin liquid and stripy AF at $\alpha \approx 0.86$.

6.3 Exact diagonalization

Additional insight in the Kitaev-Heisenberg model can be obtained with exact diagonalization. Since the computational cost of exact diagonalization scales exponentially with the number of spins, we restrict the study to a cluster with 24 spins, cf. fig. 6.1b. Periodic boundary conditions are imposed. Results of exact diagonalization are given in ref. [20], but we have also reproduced the results to have a benchmark for our DMET calculations. From figure 6.5 it is clear that the different approximations given in section 6.2 are accurate for the 24 spin-lattice. The least accurate approximation is the one in the Néel antiferromagnetic phase. This could be expected since for the other two perturbative approximations an exact solution was used at $\alpha = 1/2$ and $\alpha = 1$. In figure 6.6 we see the squared total spin in both the rotated and unrotated basis. As expected, we see full saturation of the stripy AF order parameter (or squared total spin in the rotated basis) at $\alpha = 0.5$. Note that the squared total spin is normalized to its maximum obtainable value, i.e. $S(S + 1)$ with $S = N/2$. The normalized value of the squared total spin in the original basis is given by $\frac{1}{\frac{N}{2}+1} = \frac{1}{13}$ at this point. This can also be deduced easily algebraically. First of all, we look at the expectation value of the

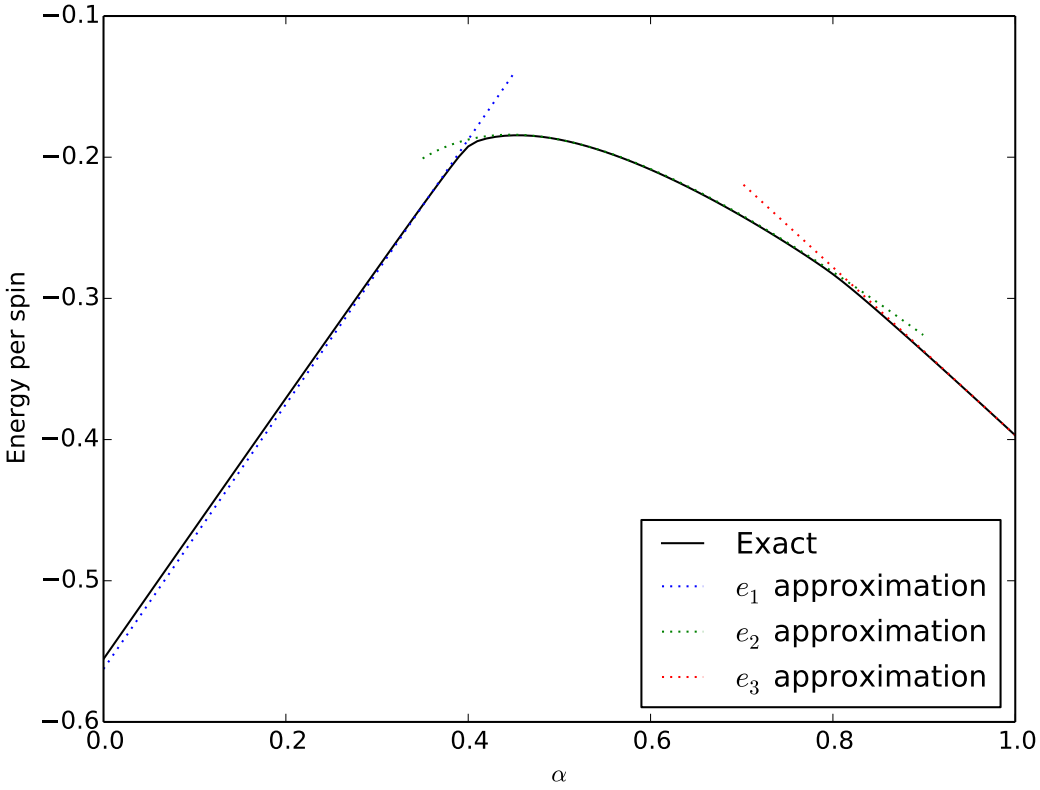

Figure 6.5: Exact energy per spin of the Kitaev-Heisenberg model on the honeycomb lattice for 24 spins (full line). Approximate values for the three phases given in section 6.2 are depicted as dotted lines.

total square spin at $\alpha = 0.5$.

$$\left\langle \hat{\mathbf{S}}^2_{tot} \right\rangle = \langle \downarrow\downarrow .. \downarrow\downarrow | U^\dagger (\sum_i \hat{\mathbf{S}}^2_i + \sum_{i \neq j} \hat{\mathbf{S}}_i \cdot \hat{\mathbf{S}}_j) U | \downarrow\downarrow .. \downarrow\downarrow \rangle \tag{6.6}$$

where U is the transformation between the unrotated and rotated basis. We now rotate the spin operators to their rotated basis, according to the sublattices given in figure 6.3. The transformation is responsible for a sign change in the scalar product $\hat{\mathbf{S}}_i \cdot \hat{\mathbf{S}}_j = \hat{S}^x_i \hat{S}^x_j + \hat{S}^y_i \hat{S}^y_j + \hat{S}^z_i \hat{S}^z_j$. If $i = j$ no sign change occurs and the first term is unchanged in the rotated basis yielding a value of $\frac{3}{4}N$. If $i \neq j$ the scalar product terms in the x- and y-direction will have no influence on the expectation values, since they consist of ladder operators. Only the terms in the z-direction are of importance. If i is part of a certain sublattice, there will be a sign change if j is part of two of the other three sublattices. We assume that we can subdivide our total system in the supercluster depicted in figure 6.3 of 24 spins. For every i there are $(\frac{N}{2} - 1)$ j's that give rise to no sign change (since i is excluded from the j summation) and

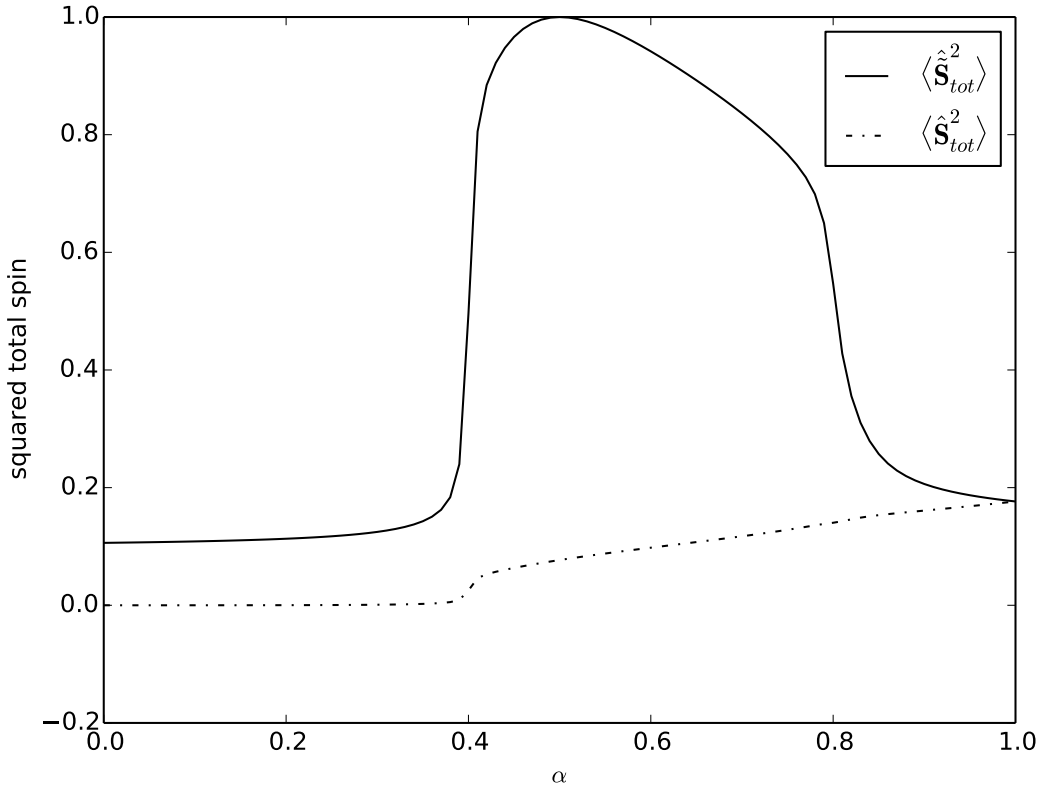

Figure 6.6: squared total spin of the 24-spin honeycomb lattice *normalized* to a maximal value of 1 at the stripy AF phase at $\alpha = 0.5$. To squared total spin in the unrotated and rotated basis are given.

$\frac{N}{2}$ j's that give rise to a sign change in the $\hat{S}^z\hat{S}^z$ part. Therefore we find

$$\left\langle \hat{\mathbf{S}}^2_{\text{tot}} \right\rangle = \frac{\frac{3}{4}N + N((\frac{N}{2}-1)\frac{1}{4} + \frac{N}{2}(-\frac{1}{4}))}{\frac{N}{2}(\frac{N}{2}+1)} = \frac{1}{\frac{N}{2}+1} \tag{6.7}$$

Here the expectation value is normalized. It yields a value of $\frac{1}{13}$ for 24 spins, and vanishes for $N \to \infty$.

The squared total spin in both bases is easily calculated in the Kitaev limit ($\alpha = 1$). It is known that spin-spin correlations vanishes for all spins seperated more than one lattice constant in the Kitaev model [62]. Furthermore, it is also known that only spin-spin correlations in the bond direction (γ) are non-vanishing for neighbouring spins. This gives us

$$\left\langle \hat{\tilde{\mathbf{S}}}^2_{\text{tot}} \right\rangle = \left\langle \hat{\mathbf{S}}^2_{\text{tot}} \right\rangle = \frac{\frac{3}{4}N + 3N\left\langle \hat{S}^\gamma \hat{S}^\gamma \right\rangle}{\frac{N}{2}(\frac{N}{2}+1)}, \tag{6.8}$$

where $\left\langle \hat{S}^\gamma \hat{S}^\gamma \right\rangle \approx 0.13$ for the Kitaev limit. The expectation value is again normalized.

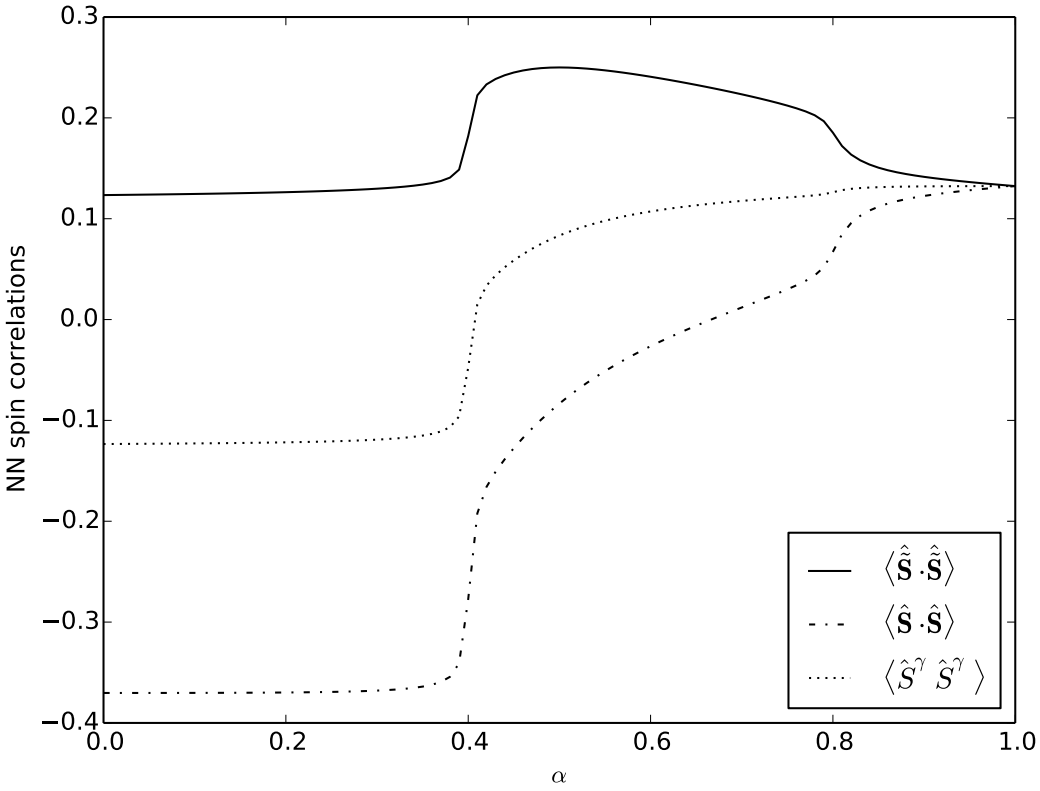

Figure 6.7: Nearest neighbour spin correlations. The solid and dot dashed line correspond to spin spin correlations of the scalar product of respectively the rotated and original basis. The dotted line corresponds with the correlation of the spin in the bond direction, this is the same in the rotated as the unrotated basis.

As expected, the squared total spin and the nearest neighbour correlation indeed fulfil this equality for the ED of 24 spins.

Furthermore two phase transitions are clear at $\alpha \approx 0.4$ and $\alpha \approx 0.8$. These values correspond well with the estimated values given in section 6.2. At the AF Néel phase, we also see that the squared total spin has an expectation value of zero, which can be expected in this phase. These phase transitions are also visible in figure 6.7. Here the nearest neighbour spin correlations are shown. First of all, the spin correlations at $\alpha = 0.5$ are given by $\left\langle \hat{\tilde{\mathbf{S}}} \cdot \hat{\tilde{\mathbf{S}}} \right\rangle = \frac{1}{4}$ and $\left\langle \hat{S}^{\gamma} \hat{S}^{\gamma} \right\rangle = \frac{1}{12}$, which is expected, since the exact solution is given at this point by the FM state in the rotated basis. We also notice that the spin-spin correlation in the bond-direction is given by $\left\langle \hat{S}^{\gamma} \hat{S}^{\gamma} \right\rangle = 0.13$ in the pure Kitaev limit, as theoretically shown [61]. It is also this direction that is the only contributor to the NN spin correlation of the scalar product. In a small region around the quantum spin liquid phase, this situation stays approximately like that. The spin-spin correlation in the bond direction remains the largest contributor of

the total spin-spin correlation of the scalar product and remains largely constant. This is a justification for the approximation of e_3 executed in section 6.2. However, the large tail of the NN spin correlations in the spin liquid region is noticeable. It shows that there is a deeper penetration of the AF stripy phase into the spin liquid phase. The tail is much smaller in the AF stripy to AF Néel transition, which indicates that this transition is more abrupt.

6.4 Results of the cluster-DMET calculations

In this section the results for the cluster DMET algorithm for the Kitaev-Heisenberg model on a honeycomb lattice are presented. We will look at the 24 spin system depicted in fig. 6.1b that was also used for the exact diagonalization. This allows us to compare the DMET solution with the exact diagonalization results.
For the honeycomb lattice, the choice of the cluster shape is not as straightforward as it was for the square lattice. Some suggested coverings are shown in fig. 6.8. The found results are dependent of the used cluster geometry. First, we will look at results obtained from the S-shaped clusters (fig. 6.8a).

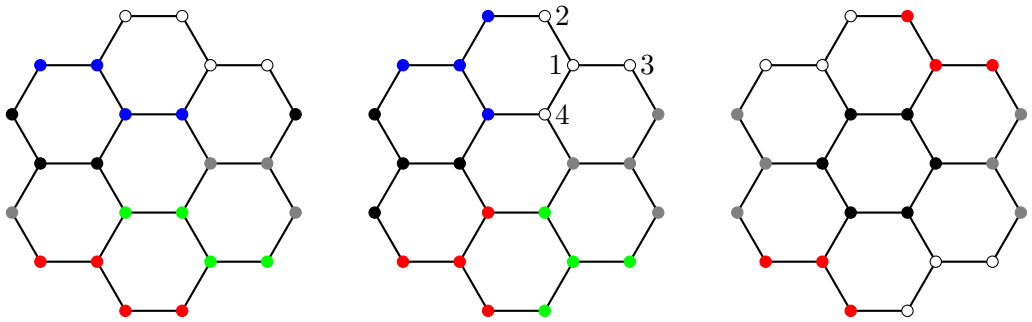

(a) S-shaped clusters **(b)** star-shaped clusters **(c)** hexagonal clusters

Figure 6.8: Different possible cluster-coverings for the hexagonal lattice.

Just as in the previous model, we first perform the calculation with random initialisation to detect possible problematic regions. The calculations are done in steps of 0.05 in the $\alpha \in [0, 1]$ interval. 20 simulations are executed in the unrotated basis and 20 in the rotated basis for every α-value. The results are given in figure 6.9. We note no real difference between the solutions found in the rotated and the original basis. This could be expected, since the restricted Hilbert space spanned by the DMET-ansatz is the same in the rotated and unrotated basis.
To see this, we first look at the structure of the block-product states. These are given by eq. 4.3. Within every bath cluster, such a state is given; the block product state is given through direct product of the states of each bath cluster. The possible states that the block-product state can represent within one bath cluster spans the Hilbert space restricted to this bath cluster. The basis transformation from original to rotated basis is local, i.e. works in on every

spin separately. This also means the basis transformation of the Hilbert space restricted to one bath cluster will give us the same restricted Hilbert space. It is thus clear that the original and the rotated basis can represent exactly the same block product states.

For the DMET-ansatz to be able to represent the same corner of the complete Hilbert space in the rotated and original basis, the basis states of the impurity used in the approximate Schmidt decomposition for the original basis (eq. 4.2) should transform into the basis states used in the approximate Schmidt decomposition for the rotated basis, which is of the same form. A basis transformation from the original to the rotated basis is not readily obtained, however, the transformation of the spin operator is. The transformation is as such, that depending on the position of the spin, $\hat{S}^x$, $\hat{S}^y$ and/or $\hat{S}^z$ will change sign (see figure 6.3). To illustrate that the basis states of the impurity transform as needed, we look at a 4-site impurity cluster. When transforming the basis $\hat{S}^z$ changes sign for the third and fourth spin in the cluster, for example. We look at an arbitrary basis state in the original basis, e.g. $|\uparrow\downarrow\downarrow\uparrow\rangle$. This is the only state with quantum numbers $S_1^z = \frac{1}{2}$, $S_2^z = -\frac{1}{2}$, $S_3^z = -\frac{1}{2}$ and $S_4^z = \frac{1}{2}$. In the rotated basis, the quantum numbers are clearly $\tilde{S}_1^z = \frac{1}{2}$, $\tilde{S}_2^z = -\frac{1}{2}$, $\tilde{S}_3^z = \frac{1}{2}$ and $\tilde{S}_4^z = -\frac{1}{2}$. There is only one state in the rotated basis that has these quantum numbers, i.e. $|\uparrow\downarrow\uparrow\downarrow\rangle$. The transformation of the original basis state will thus give us this basis state up to a phase difference. This is one of the basis states used in the approximate Schmidt decomposition for the rotated basis. For this basis state, the transformation is thus as wanted. It is clear that for other basis states, a similar transformation will happen and that every basis state will be transformed in another basis state of the rotated basis. The possible phase difference can be absorbed in a_i. Calculations in the original basis should thus give the same result as calculations in the rotated basis. The speed of convergence can however differ between the two bases.

Now we look further to the results obtained from random initialisation. All calculations are done in maximally a few hundred iterations. The convergence criterion is again set at $\left|\frac{E_{\text{old}} - E_{\text{new}}}{E_{\text{new}}}\right| < 10^{-7}$ for the calculations. A rather minimal spread of the calculations is found in the Néel AF phase region. Most of the calculations converge to the same minimum, however, a small fraction of the calculations converge to a less optimal minimum. In the stripy AF phase region, spread is even smaller, but when the α-parameter is entering the spin liquid phase, a great variety of different converged wave functions are found. Although the energy of the wave functions are all almost the same, the wave functions themselves are rather different, as can be seen in the spread of the properties. Careful selection of the right wave function will thus be of importance. The most optimal wave functions in terms of energy found by random initialisation are not the wave functions desired in this region, as can be seen in figure 6.9. It is possible that a more optimal wave function exists, which is hard to get starting from random initialisation. Another possibility is that the spin liquid phase can not be found sufficiently well through cluster DMET calculations. Just as in the previous studied $J_1 - J_2$ model on the square lattice, calculations in the nonmagnetic phase impose some problems.

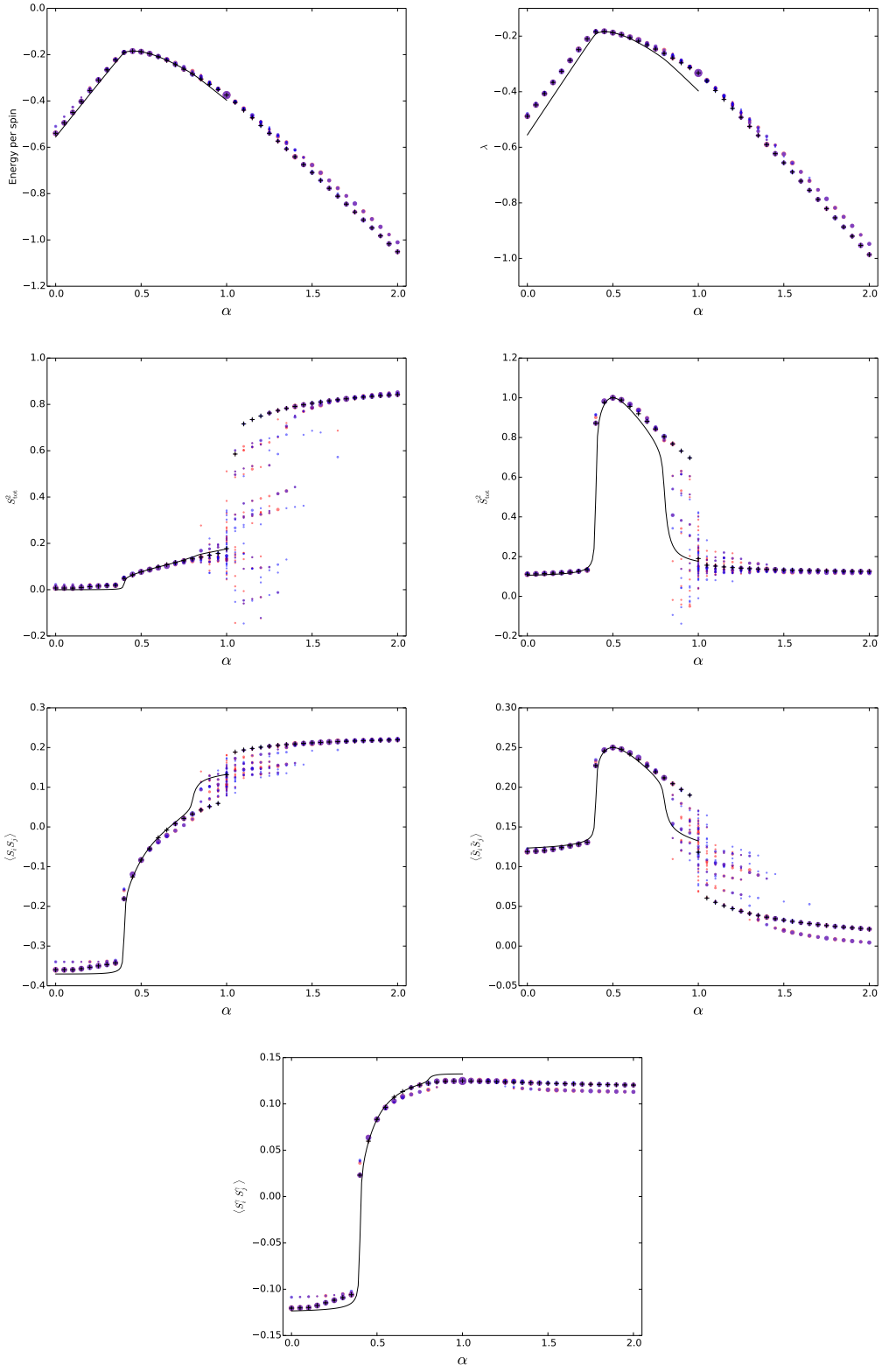

Figure 6.9: Calculations executed with random initialisation in the original (blue markers) and rotated basis (red markers). The magnitude of the markers scale with the number of calculations that yielded the corresponding values. The + markers represent the lowest DMET-energy (and also the lowest λ-value). The full lines are results obtained from exact diagonalization. The used cluster shape is the S-shaped cluster, see fig. 6.8a

In figure 6.9, the system is also calculated for $\alpha > 1$. The large spread of the properties of the found ground state continues up to $\alpha \approx 1.5$, after this, the DMET-algorithm converges to one of two almost equivalent solutions, as can be seen in e.g. the plot for the spin-spin correlation in the rotated basis $\left\langle \hat{\tilde{S}}_i \cdot \hat{\tilde{S}}_j \right\rangle$. If we want to use sweeps, that are easily reproducible, we would want to commence the sweep at a point that converges consistently to the same wave function with random initialisation. A right running sweep could be started at at α before the spin liquid phase and a left running one at $\alpha > 1.5$, following one of the two found solutions in that region.

Further, it is easily noted that in the rotated basis DMET can represent some of the degenerate ground states at $\alpha = 0.5$, for example $|\downarrow\downarrow .. \downarrow\downarrow\rangle$ and $|\uparrow\uparrow .. \uparrow\uparrow\rangle$. The degenerate ground states at $\alpha = 0.5$ have $\left\langle \hat{\tilde{S}}^2_{\text{tot}} \right\rangle$ maximal as necessary and sufficient condition. The DMET-ansatz in the rotated basis can represent ground states at this point, which means that the DMET-ansatz in the original basis should also be able to represent them. If we look at the values for $\left\langle \hat{\tilde{S}}^2_{\text{tot}} \right\rangle$ obtained through DMET calculations, it is clear that an exact solution is found.

There are only problems for the convergence in the spin liquid phase, thus a sweep is suggested from the LRO phases to the spin liquid phase. A sweep is started at $\alpha = 0$, in the Néel AF phase where calculations with random initialisation show a consistent convergence. A sweep introduces a bias towards a solution that is similar to the previous converged wave function. This is clearly visible in fig. 6.10. The measured properties in the spin liquid phase follow the trend of the properties in the stripy AF phase and fail to detect the spin liquid properties. In the region of the spin liquid, the right sweep gives us stripy AF-like solutions. Extra evidence for this, is the fact that the calculated DMET-energies follow the estimated energy through second-order perturbation $e_2 \approx -\frac{1}{8}(5\alpha - 3 + \frac{1}{\alpha})$. Although the other properties do not follow the estimates obtained through second order perturbation in appendix B quantitatively well, they follow qualitatively the same trend (dotted lines in figure 6.10). This could be an indication that the stripyness of the solution can be adequately found in the DMET framework. The problem phase is the spin liquid phase. When the solution deviates from the exact stripy solution and tends to a spin liquid, DMET fails to capture the ground state accurately.

A left sweep starting from the region $\alpha \in [1.5, 2.0]$ is also an option, since the randomly initialized calculations with this system parameter converge to one of two different solutions. Results are given in figure 6.11. There is some improvement in the NN spin correlations which indicate a phase transition near $\alpha = 0.8$. However, the squared total spin shows an irregular behaviour. Also, the DMET-energy for the left sweep is higher than the DMET-energy found for the right sweep in the spin-liquid phase. Without a priori knowledge of the exact solution, this left sweep solution would not be selected on grounds of minimal DMET-energy.

A method to improve the calculations and possibly detect the spin-liquid phase more accurately is by choosing another cluster. In figure 6.8 two other alternatives for the cluster division are given.

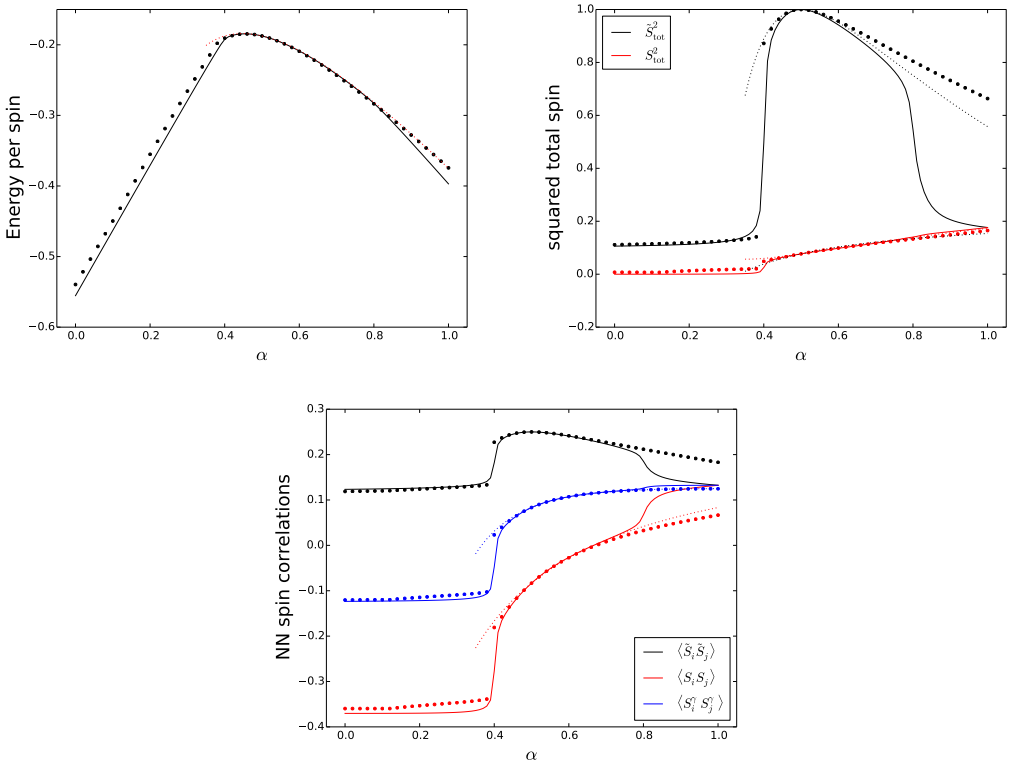

Figure 6.10: Results for a right sweep of the DMET-algorithm with S-shaped clusters, see fig. 6.8a. The dotted lines represent the results obtained through second order perturbation in appendix B, the full lines are ED results.

First, the star shaped cluster will be applied (see fig. 6.8b). In figure 6.12, the results of a random initialisation are given. Just like in the previous case, the random initialisation converges quite consistently to the same results in the two AF phases. In the spin liquid phase, there is again a large spread on the calculated properties. A right and left sweep are again executed and the results are shown in figure 6.13. A very good correspondence in the Néel AF phase with the exact solution is found when using the starshaped cluster. The DMET-energy and the properties correspond almost exactly with the ED calculations in the Néel AF phase. In the stripy AF phase, the DMET solution deviates more and more from the exact diagonalization when approaching the spin liquid phase. When looking at the left sweep, results in the spin liquid have improved a bit. However, the DMET-energy is again higher compared to the right sweep, hence this improvement is again of no use without a priori knowledge. Also, we know that the converged properties are inconsistent for different random initialisations at $\alpha = 1$. The results of the left sweep are dependent on the first initialized value, hence for every left sweep different results can be obtained. However, the trend of the results stays the same for the different left sweeps, showing a steeper change of the properties around $\alpha = 0.8$.

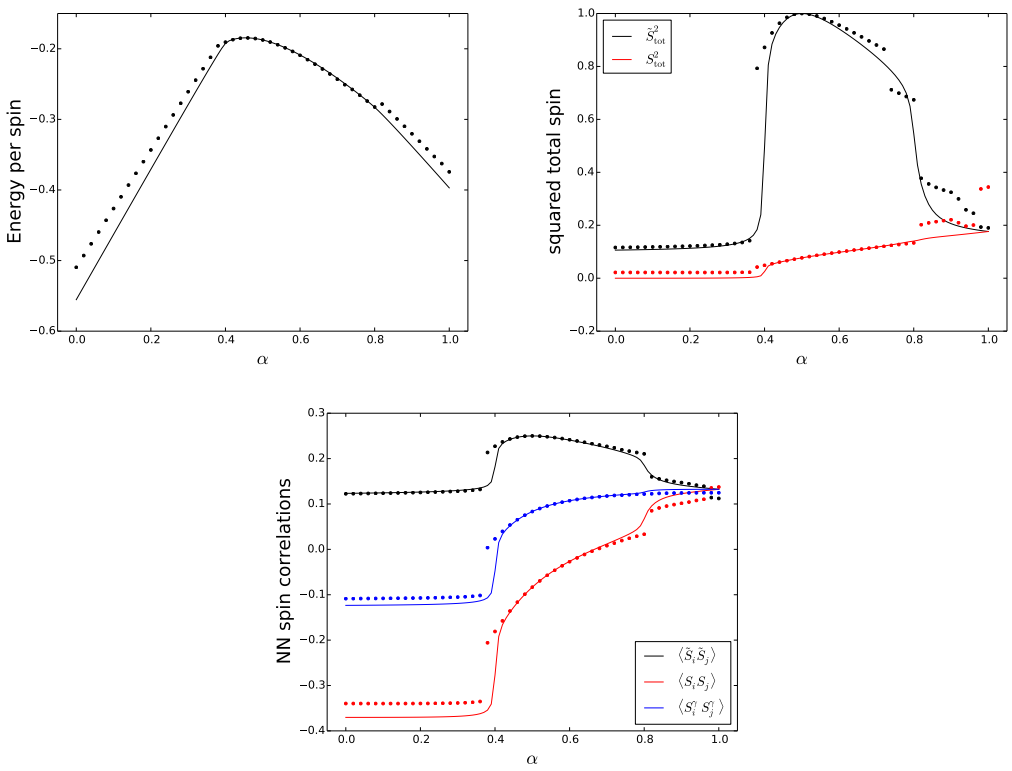

Figure 6.11: Results for a left sweep of the DMET-algorithm with S-shaped clusters, see fig. 6.8a. The full lines are ED results.

It is noteworthy that in contrast to the S-shaped cluster, the phase transition to the spin liquid is visible here using the right sweep results. These are also the optimal results in terms of DMET-energy. There is clearly a discontinuity of the derivative at $\alpha = 0.8$ for the rotated squared total spin. This indication for a phase transition is absent in the S-shaped cluster.

Different entanglement entropies are also calculated for the starshaped cluster and are shown in figure 6.14. Since the rotational basis is achieved by a local basis transformation per site, the entanglement entropy should be the same in both bases. A ground state of the system at $\alpha = 0.5$ is given, as said before, by $|\uparrow\uparrow \cdots \uparrow\rangle$ in the rotated basis. This wave function is clearly unentangled between every two sites, hence all entanglement entropies of subsystems consisting of sites should vanish. This is clearly visible in figure 6.14. Furthermore, we see that $S(\rho_{12}) = S(\rho_{13}) = S(\rho_{14})$ at $\alpha = 0$. This is as expected, since C_3 rotational symmetry of the lattice is not broken when there is no anisotropic Kitaev-interaction. From the moment we introduce the Kitaev-interaction into our lattice, these three entanglement entropies are not equal any more and rotational symmetry is broken. In the right side of figure 6.14 the first derivatives of the entanglement entropies are given. We note a discontinuity at $\alpha = 0.4$, indicating the phase transition from the Néel AF phase to the stripy AF phase. A maximum in the derivatives is also visible at $\alpha = 0.8$. As said in ref. [13], this indicates a phase

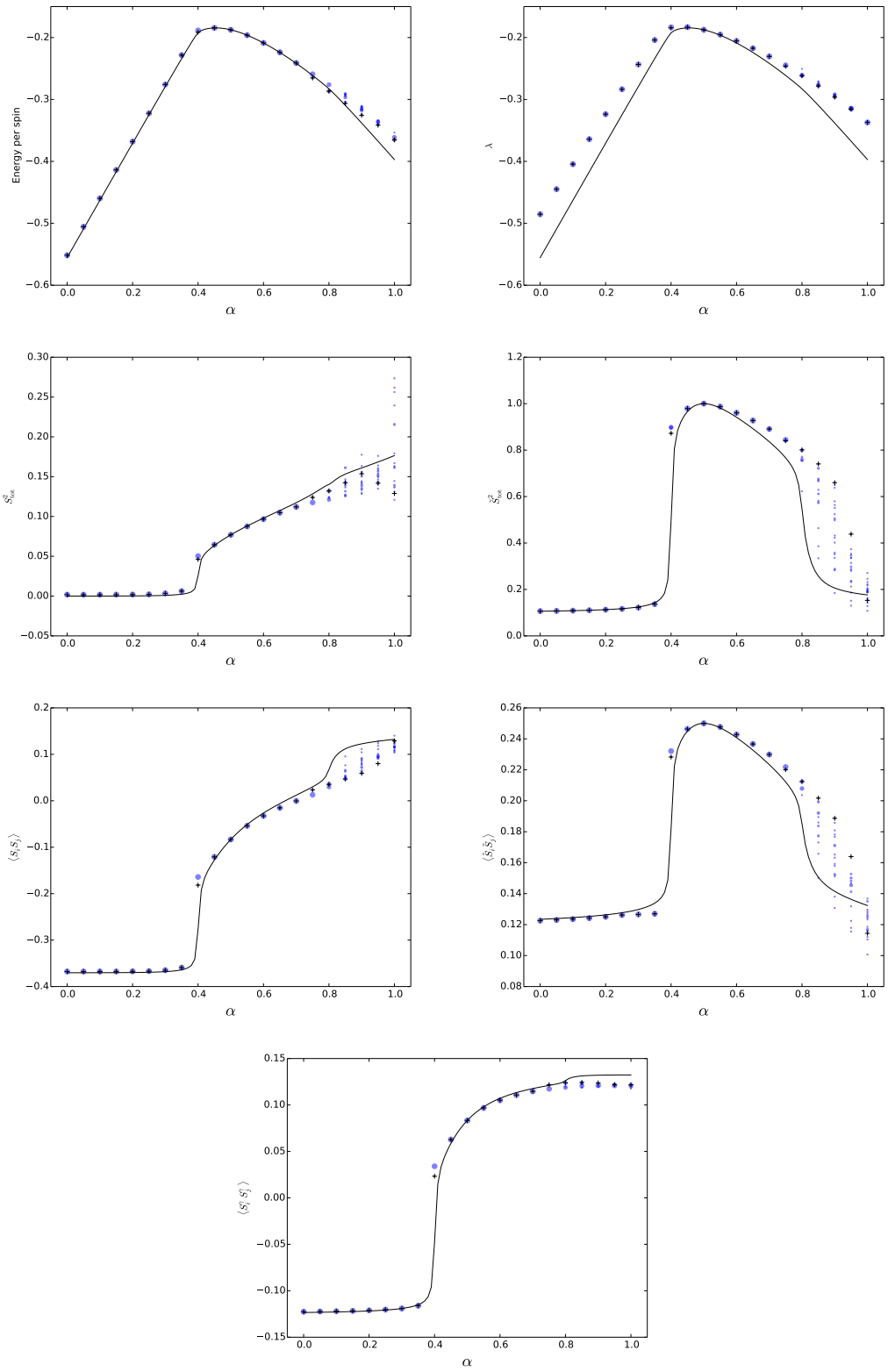

Figure 6.12: Calculations executed with random initialisation in the original (blue markers) and rotated basis (red markers). The magnitude of the markers scale with the number of calculations that yielded the corresponding values. The + markers represent the lowest DMET-energy (and also the lowest λ-value). The full lines are results obtained from exact diagonalization. The used cluster shape is the star shaped cluster, see fig. 6.8b.

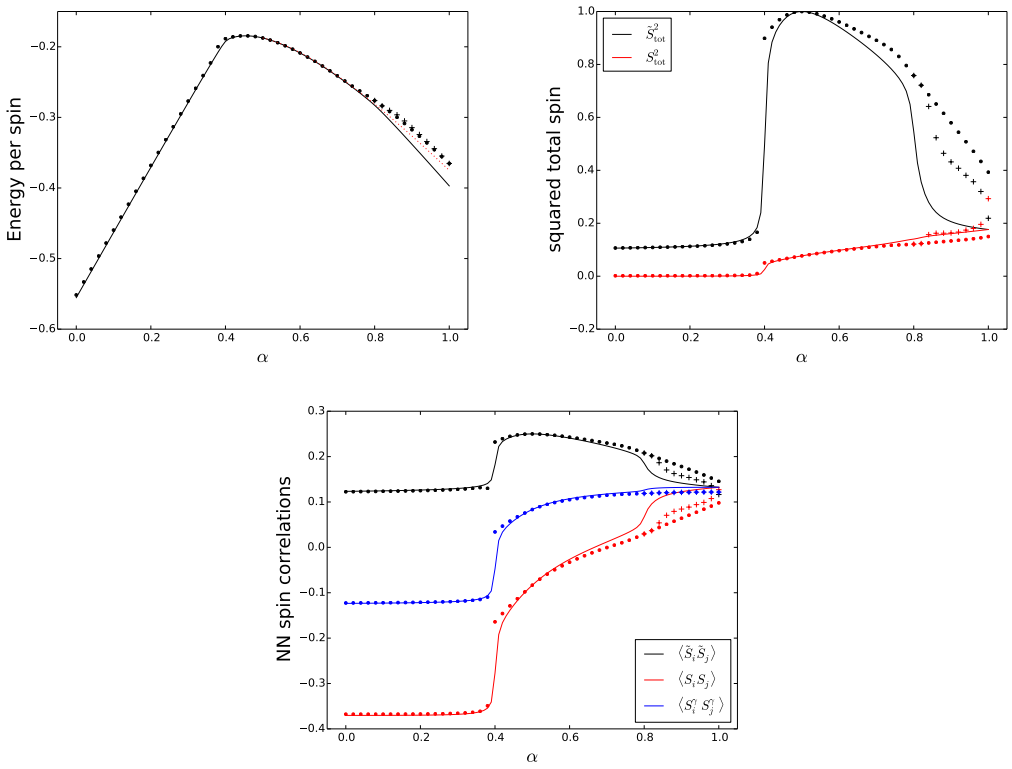

Figure 6.13: Results for a right sweep (dots) and left sweep (crosses) of the DMET-algorithm with starshaped clusters, see fig. 6.8b. The full lines are ED results. The dotted line is a result obtained from second order perturbation theory.

transition, more particularly the transition to a spin liquid.

For the star-shaped cluster, there are thus different indications for a phase transition to the spin liquid. A very inconsistent convergence from $\alpha = 0.8$ onwards indicates a different behaviour (which is hard to capture in the DMET-algorithm) of the system. Discontinuity of the derivative of the total squared rotated spin is an indication of a phase transition. Finally, the maximum found in the entanglement entropy indicates a transition as well.

Finally, it is also possible to use the hexagonal 6-spin cluster shown in figure 6.8c. Results for a right sweep of the 24-spin system with this cluster is given in figure 6.15. It is expected that the precision of the calculations increase with increasing cluster size, since the corner of the Hilbert space the DMET-ansatz can represent enlarges. In the Néel AF phase, the correspondence with the ED results is worse than the results obtained by a star shaped cluster (fig. 6.13). The geometry of the star shaped cluster is clearly well fit for the description of the Néel AF phase, which even the larger Hilbert space dimension of the hexagonal cluster can not make up for. In the stripy AF phase, a good correspondence with the exact results is found. The hexagonal cluster is, together with the S-shaped cluster, better at representing the stripy AF phase. A last improvement of the results we see with the hexagonal cluster

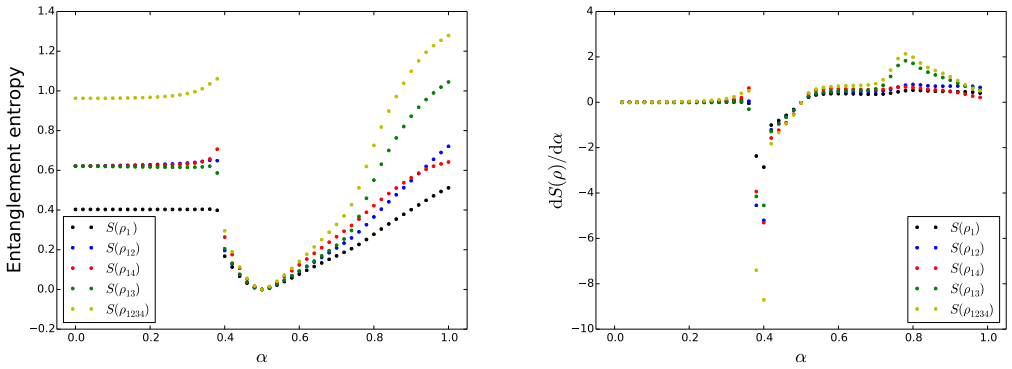

Figure 6.14: Different entanglement entropies calculated from the DMET-algorithm with starshaped clusters are given in the left figure. In the right figure the first derivative of the entanglement entropies are given. See fig. 6.8b for the numbering of the spins.

is that the right sweep shows a transition to the spin liquid state. When looking at the properties, the transition happens at $\alpha \approx 0.92$, which is not the expected value of $\alpha \approx 0.8$. Although the transition happens at a wrong α-value, we notice that the different properties at $\alpha = 1$ have values corresponding well with the ED. Also, when looking at the squared total spin in the rotated basis at $\alpha \approx 0.8$, we notice some sudden change in the tangent of the property. Although this is not enough evidence for the real phase transition, it is an indication that something happens at this point. When finally looking at the entanglement entropies in figure 6.16, a clear phase transition is noticeable at $\alpha = 0.4$ and a second phase transition at $\alpha = 0.92$. This is again the delayed phase transition to a spin liquid we noted before in the properties. A sudden increase in the first derivative of the entanglement entropy can be seen at $\alpha \approx 0.8$. This is the point where the phase transition to the spin liquid should happen. Although the phase transition is obtained at a larger α with the hexagonal cluster, this can be considered another indication for odd behaviour at this point.

Larger honeycomb lattice

In the previous section, the Kitaev-Heisenberg model is discussed for a honeycomb lattice of 24 spins through the cluster DMET algorithm. When we want to calculate the bulk material, we could move on to larger lattices. In ref. [70], it is suggested that the phase transition from the Néel AF phase to the stripy AF phase happens at $\alpha = \frac{1}{3}$ and not at $\alpha = 0.4$ as suggested from exact diagonalization and second order perturbation. By enlarging the lattice system, we can obtain extra information on the phase transition in the bulk. Improving the calculations can also be done by enlarging the cluster size. However, since the computational cost scales exponential with enlarging cluster size, cluster DMET with the 6-spin cluster is already quite costly.

In this section, the honeycomb lattice with 96 spins is used. When expanding the 24 spin

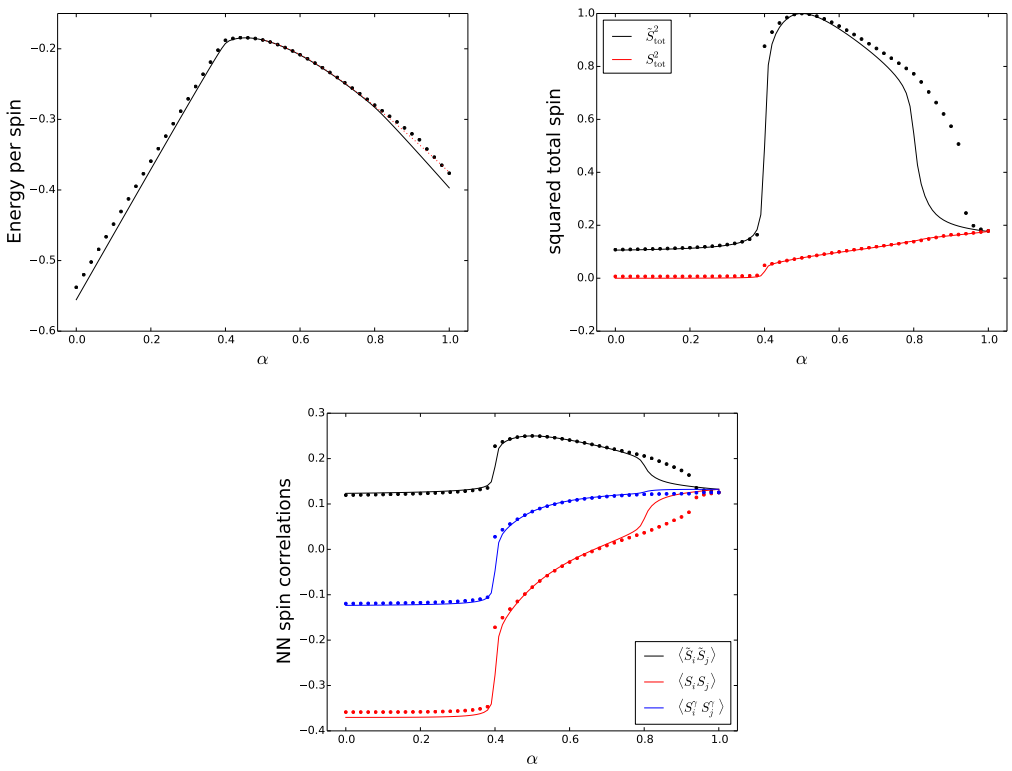

Figure 6.15: Results for a right sweep of the DMET-algorithm with hexagonal shaped clusters, see fig. 6.8c

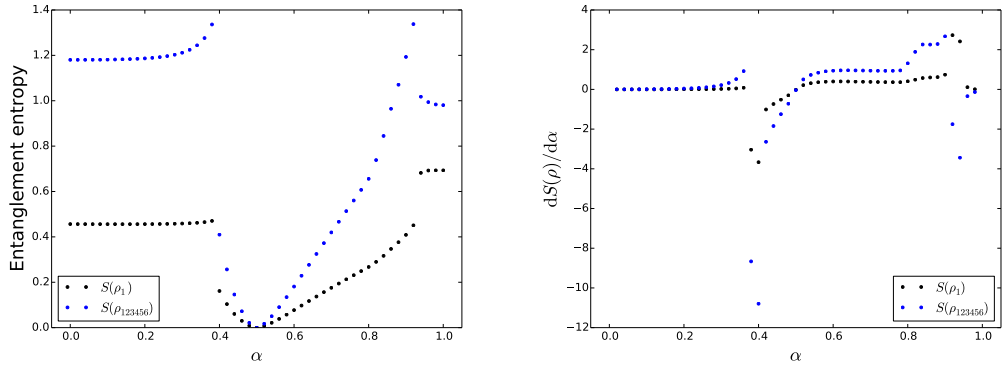

Figure 6.16: Different entanglement entropies calculated from the DMET-algorithm with hexagonal clusters are given in the left figure. In the right figure the first derivative of the entanglement entropies are given.

honeycomb lattice by one extra layer, we get a 54 spin honeycomb lattice. This 54 spin lattice is not coverable with the S-shaped and star shaped clusters. Also, a rotated basis that respect periodic boundary conditions, equivalent with figure 6.3, cannot be found.
When expanding the 54 spin lattice by another extra layer, we get a 96 spin honeycomb lattice.

This lattice is coverable with the three types of clusters, and a rotated basis equivalent with figure 6.3 can also be found. Due to the polynomial scaling of the calculations, the simulation of 96 spins is still feasible with the DMET-algorithm. We execute the calculations with the two most promising clusters, the star shaped cluster and the hexagonal cluster.

For the star shaped cluster, we see almost no difference with the 24 spin system. The results for the squared total spin and the DMET-energy per spin are given in figure 6.17. Some minor changes in energy and properties are noticeable, but no change in the trend is noted and the phase transitions are still observed at the same α-values. The only property that changes considerably is the squared total spin in original and rotated basis. This can be expected since it is clear from second order perturbation theory that the squared total spin in the rotated basis vanishes with increasing lattice size in the Néel AF phase. Furthermore, the squared total spin in the original basis is also dependent of lattice size in the stripy AF phase, as can be seen in eq. B.55. The value of the squared total spin in the original basis at $\alpha = 0.5$ is indeed the expected exact value of $\frac{1}{N/2+1} = \frac{1}{49}$, due to the ground state being exactly representable through the DMET-ansatz. The behaviour of the squared total spin at larger system sizes is thus as expected.

Except for the expected scaling of the squared total spins with increasing system size, we see no real different behaviour of the 96 spin system. It is highly possible that the extra spins introduced when expanding the lattice contribute only in a mean-field kind of way within the DMET framework, as described in ref. [13]. In the original paper of cluster DMET, it is noted that spins situated far from the impurity have energies comparable with results obtained through hierarchical mean-field. When expanding the lattice further, new spins also contribute in a hierarchical mean-field kind of way and do not influence the DMET-energy in the impurity that much. Because of this, it is possible that the study of even larger systems will encompass no extra information.

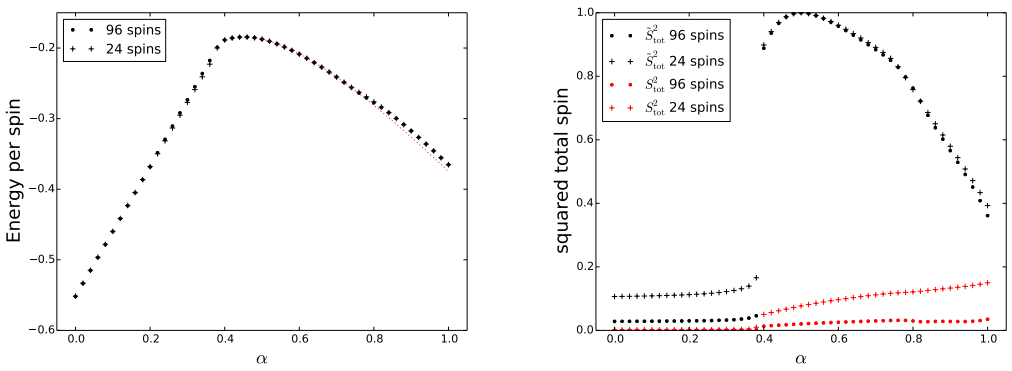

Figure 6.17: Results for a right sweep of the DMET-algorithm with star shaped clusters, the results for a 24 spin system and a 96 spin system are compared. Nearest neighbour spin-spin correlation are not given since there is no noteworthy difference visible between the two system sizes.

A way to avoid that these extra added spins only contribute in a hierarchical mean-field like way, is by enlarging the impurity cluster size. Calculations are executed with the hexagonal cluster on a 96 spin lattice and we study if there is a qualitative and quantitative difference with the smaller 24 spin lattice. The results are given in figure 6.18. We notice some difference

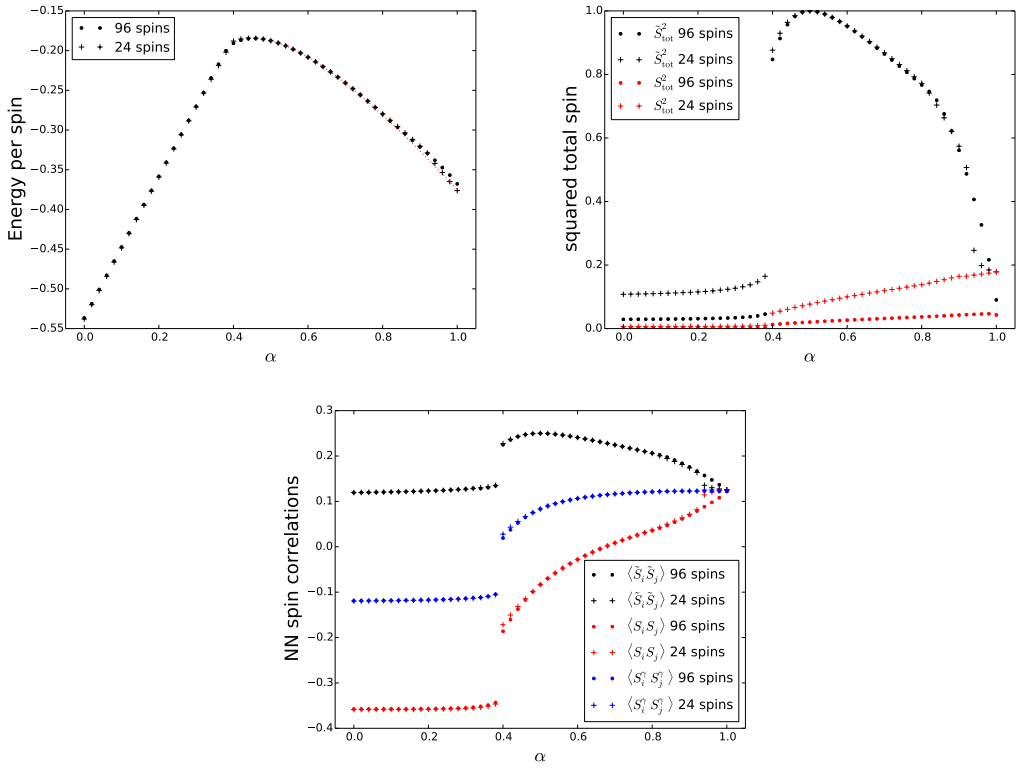

Figure 6.18: Results for a right sweep of the DMET-algorithm with hexagonal clusters, the results for a 24 spin system and a 96 spin system are compared.

in the DMET-energy and also a large change in the behaviour of the squared total spins. The explanation of this last behaviour has been given before. We note at $\alpha \approx 0.92$, the results for the 96 spin system do not show a phase transition towards the spin liquid, in contrary to the 24 spin system. It is clear also that at $\alpha = 1$, the expected spin liquid is not found. At $\alpha = 1$ it is after all expected that eq. 6.8 is satisfied. When increasing the number of spins, the number of parameters to be optimized in the DMET-ansatz also increases. This increase of parameters amplifies the problem of optimization into local minima. It is very probable this causes the DMET-algorithm to be unable to find the spin liquid phase through sweeps in the 96 spin system. Although the phase transition from the stripy AF phase to the spin liquid is not observed anymore, the phase transition between the two AF phases still is. The location of the transition is not changed when enlarging the system; the transition is still observed at $\alpha = 0.4$. This suggests that the transition in the thermodynamic limit will happen around this point and not at $\alpha = \frac{1}{3}$ as given in ref. [70].

7 Conclusion

In this thesis, the cluster density matrix embedding theory (DMET) algorithm introduced by Fan *et al.* [13] has been programmed and used for the investigation of different frustrated spin lattices.

The implemented program has been first used on the $J_1 - J_2$ Heisenberg model on the square lattice. This model encompasses nearest neighbour (NN) and next-nearest neighbour (NNN) interactions between the spins. Three phases can be expected in the range $J_2/J_1 \in [0, 1]$. A Néel antiferromagnetic (AF) phase with long-range order (LRO) is expected at low NNN interaction up to $J_2/J_1 \approx 0.4$, where a transition happens to a nonmagnetic phase that disappears again at $\alpha \approx 0.6$. The last phase is a collinear AF phase with LRO. The exact nature of the nonmagnetic phase is still up to discusion. The most likely candidates are the dimer valence bond crystal (VBC), the plaquette resonating valence bond (RVB) and a quantum spin liquid. This is also the system that is investigated in the original cluster DMET paper [13].

A method for the calculations of local and nonlocal properties has been introduced according to the conventions used in DMET. This method justifies the energy per spin calculation suggested by Fan in ref. [13], but it also allows us to calculate other properties. This method provides us with the opportunity to calculate both the Néel and the collinear order parameters in the square lattice. Random initialisation of the DMET algorithm will give us consistent results most of the time, however, at $J_2/J_1 \in [0.6, 0.8]$ the convergence is inconsistent. Because of this, a sweep is suggested from the ordered phases into the troublesome region. This way we get states that are more optimal than the results found by random initialisation and our calculations are easily reproducible and more insensitive to the initialisation.

The obtained DMET-energy corresponds with the energies found by Fan *et al.* [13] and the order parameters show Néel order up to $J_2/J_1 \approx 0.4$ and collinear order starting from $J_2/J_1 \approx 0.62$. The position of these phase transitions are clearly in correspondence with results from other methods. The Néel order does not disappear completely in the nonmagnetic phase, which is to be expected due to the finite size of the system. Lastly, different entanglement entropies are calculated. The phase transitions can also be detected through these entanglement entropies and the exact nature of the nonmagnetic phase is investigated through these. There is clear evidence against the dimer VBC and some weak evidence in

favour of a weak plaquette RVB. However, since it is clear from the Néel order parameter that we still have some finite size effects, it is also possible that this weak evidence is due to these effects. The exact nature of the nonmagnetic phase, the plaquette RVB and the quantum spin liquid, is left open for discussion.

We also investigate the Kitaev-Heisenberg model on the honeycomb lattice, as introduced in ref. [20]. This model has only nearest neighbour interactions and frustration is introduced through anisotropy in the Hamiltonian. When we look at $\alpha \in [0, 1]$, with α parametrising the anisotropy in the Hamiltonian in correspondence with ref. [20], the system shows three different phases. At low α and thus low anisotropy, the Néel AF phase is found. A stripy AF phase is found at intermediate α and a quantum spin liquid is found at high anisotropy. At $\alpha = 1$ we find the Kitaev model as introduced by Kitaev in ref. [61]. At $\alpha = 0.5$ the system can be solved exactly for arbitrary system size through a basis transformation. Exact diagonalization (ED) has been executed on a 24 spin lattice and the same results as in ref. [20] have been obtained. The phase transitions are detected at $\alpha \approx 0.4$ and at $\alpha \approx 0.8$. However, according to ref. [70], the phase transition between the two AF phases should be expected at $\alpha = \frac{1}{3}$.

Cluster DMET calculations have been executed with different types of clusters. S-shaped, star shaped and hexagonal clusters are proposed, as shown in figure 6.8. First the cluster DMET is executed with these clusters on the 24 spin lattice. This way we can compare with ED calculations. We notice that random initialisation is quite consistent in the AF phases but converges to different minima in the spin liquid. Also, the most found solution in the AF phases is also the energetically most favourable solution. This is thus a first, unwanted, way to detect the transition to the spin liquid. Furthermore an exact solution is found through cluster DMET at $\alpha = 0.5$, as can be expected. Also, we notice no difference between calculations in the original or transformed (rotated) basis, which is also as expected since the DMET-ansatz describes the same Hilbert space in both bases.

Sweeps are again executed to have a good reproducibility of the results. The solutions of the sweeps are again more optimal than the random initialisations DMET-energy-wise. Every cluster has its own advantage. The S-shaped cluster represent the stripy phase better than the star shaped cluster, while the star shaped custer is better at representing the Néel phase. Also when executing a right sweep, the star shaped cluster naturally shows a phase transition at $\alpha = 0.8$, while this is not the case for the S-shaped cluster. Although the star shaped cluster shows a transition at $\alpha = 0.8$, it fails at adequately calculating the properties and energy when comparing it with ED results. Since the DMET-ansatz with the hexagonal cluster can represent a larger Hilbert space than the 4 spin clusters, it is expected that this should give us improved results. However, we note that the star shaped cluster is still better at representing the Néel AF phase. The geometry of the star shaped cluster gives it an advantage that even using the larger hexagonal cluster can not achieve. At the stripy AF phase the hexagonal cluster gives us very good results and at $\alpha \approx 0.8$ both the squared total

spin in the rotated basis and the entanglement entropy give us a hint of some odd behaviour at this point. Although odd behaviour is detected at $\alpha \approx 0.8$, a clear phase transition to the spin liquid is found only later, at $\alpha \approx 0.92$. This is clearly too late and does not qualitatively correspond with the ED. While the phase transition may be detected at the wrong moment with the hexagonal lattice, the properties after this transition are in good correspondence with the exact results.

The 96 spin honeycomb lattice is also studied through cluster DMET calculations. A large change is seen in the squared total spin properties. This is expected since these scale with system size. Only minor changes on the energy per spin and the nearest neighbour spin-spin correlations are found. Phase transitions are found at the same points as in the 24 spin system. A possible explanations for this is that finite size effects for this system are rather small, but it is also possible that the added spins have a contribution that is largely hierarchical mean-field like and do not give us much more information.

Lastly, also a method to calculate spectral functions has been proposed in this thesis, and has already been implemented in the cluster DMET code. However, optimization of the code is still necessary to calculate spectral functions for meaningful system sizes.

Appendices

A Computational details

In this section, we go deeper into the details of solving the eigenvalue problem given by

$$\left\langle \frac{\partial \Psi_0}{\partial \mathrm{pm}^*} \middle| \hat{H} \middle| \Psi_0 \right\rangle = \lambda \left\langle \frac{\partial \Psi_0}{\partial \mathrm{pm}^*} \middle| \Psi_0 \right\rangle . \tag{A.1}$$

We recall that pm are the parameters to be optimized, i.e. a_α with $\alpha \neq \alpha_0$ and $a_{\alpha_0} b^{\alpha_0}_{B_0\beta'}$. The right hand term of the equation is easily found with eq. 4.5 and eq. 4.7 as

$$\left\langle \frac{\partial \Psi_0}{\partial \mathrm{pm}^*} \middle| \Psi_0 \right\rangle = \mathrm{pm}, \qquad \forall \mathrm{pm}. \tag{A.2}$$

The first part of equation A.1 is bit trickier. First of all we note that the investigated Hamiltonian is of the form

$$\hat{H} = \sum_{i,j} J^{xx}_{ij} \hat{S}^x_i \hat{S}^x_j + J^{yy}_{ij} \hat{S}^y_i \hat{S}^y_j + J^{zz}_{ij} \hat{S}^z_i \hat{S}^z_j, \tag{A.3}$$

or

$$\begin{aligned} \hat{H} = \sum_{i,j} & \frac{J^{xx}_{ij} - J^{yy}_{ij}}{4} \hat{S^+_i} \hat{S^+_j} + \frac{J^{xx}_{ij} - J^{yy}_{ij}}{4} \hat{S^-_i} \hat{S^-_j} + \\ & \frac{J^{xx}_{ij} + J^{yy}_{ij}}{4} \hat{S^+_i} \hat{S^-_j} + \frac{J^{xx}_{ij} + J^{yy}_{ij}}{4} \hat{S^-_i} \hat{S^+_j} + J^{zz}_{ij} \hat{S}^z_i \hat{S}^z_j \end{aligned} \tag{A.4}$$

If we can calculate

$$\left\langle \frac{\partial \Psi}{\partial \mathrm{pm}^*} \middle| \hat{S}^\cdot_i \hat{S}^\cdot_j \middle| \Psi \right\rangle , \tag{A.5}$$

then we can also calculate the full first term. To calculate this term we define a new array A, with

$$A[C, \beta, i] = b^i_{C\beta} \qquad C \neq \mathrm{imp}$$

$$A[\mathrm{imp}, \beta, i] = \delta_{i\beta} \qquad \text{otherwise}$$

It is clear then that eq. 4.4 can be written as

$$|\Psi\rangle = \sum_i a_i \bigotimes_{C \in \mathrm{clusters}} \sum_\beta A[C, \beta, i] \, |\beta\rangle_C , \tag{A.6}$$

with C being all the clusters (so impurity and bath clusters).
Secondly, we create the new array B, which gives the terms for a spin operator acting on the wave function. Since the spin operators are local, only the coefficients belonging to the corresponding cluster will change in eq. A.6. B is thus given by

$$\sum_{\beta} B[\text{type},k,\text{C},\beta,\text{i}]\,|\beta\rangle_C = \sum_{\beta} A[C,\beta,i]\hat{S}_k^{\text{type}}\,|\beta\rangle_C\,, \tag{A.7}$$

with i the position of the spin operator relatively in the cluster and type the type of spin operator, i.e. $\hat{S}^z, \hat{S}^+$ or $\hat{S}^-$. A spin operator acting on a wave function can then be written as

$$\hat{S}_k^{\text{type}}\,|\Psi\rangle = \sum_i a_i \bigotimes_{C\neq C'} \sum_{\beta} A[C,\beta,i]\,|\beta\rangle_C \sum_{\beta} B[\text{type},k,C',\beta,i]\,|\beta\rangle_{C'}\,. \tag{A.8}$$

Now if we use these arrays in eq. 4.7, we get

$$|\Psi\rangle = \sum_{i\neq i_0} a_i \bigotimes_{C} \sum_{\beta} A[C,\beta,i]\,|\beta\rangle_C + \sum_{\beta'} a_{i_0} b^{i_0}_{B_0\beta'}\,|\beta'\rangle_{B_0} \bigotimes_{C\neq B_0} \sum_{\beta} A[C,\beta,i]\,|\beta\rangle_C\,. \tag{A.9}$$

Now we make a new array A_f formed by the following rules:

$$A_f[C,\beta,\text{pm}] = A[C,\beta,i] \qquad \text{if pm} = a_i \neq a_{i_0}$$

$$A_f[C,\beta,\text{pm}] = A[C,\beta,i_0] \qquad \text{if pm} = a_{i_0} b^{i_0}_{B_0\beta'} \text{ and } C \neq B_0$$

$$A_f[C,\beta,\text{pm}] = \delta_{\beta\beta'} \qquad \text{if pm} = a_{i_0} b^{i_0}_{B_0\beta'} \text{ and } C = B_0$$

It is clear now that the previous equation can be written as

$$|\Psi\rangle = \sum_{\text{pm}} \text{pm} \bigotimes_{C} \sum_{\beta} A_f[C,\beta,\text{pm}]\,|\beta\rangle_C\,. \tag{A.10}$$

Our goal is to write eq. A.8 in a similar form through the extension of B to B_f. Extension of B follows the same rules as A-extension if $C \neq B_0$. If the spin operator however acts on B_0 we get

$$\begin{aligned}\hat{S}_k^{\text{type}}\,|\Psi\rangle = &\sum_{i\neq i_0} a_i \bigotimes_{C\neq C'} \sum_{\beta} A[C,\beta,i]\,|\beta\rangle_C \sum_{\beta} B[\text{type},k,C',\beta,i]\,|\beta\rangle_{C'} \\ &+ \sum_{\beta'} a_{i_0} b^{i_0}_{B_0\beta'} \hat{S}_k^{\text{type}}\,|\beta'\rangle_{B_0} \bigotimes_{C\neq B_0} \sum_{\beta} A[C,\beta,i]\,|\beta\rangle_C\,.\end{aligned} \tag{A.11}$$

So only the last rule changes for B-extension in correspondence with A-extension to

$$\sum_{\beta} B_f[\text{type},k,\text{B}_0,\beta,\text{pm}]\,|\beta\rangle_C = \sum_{\beta} \delta_{\beta\beta'} \hat{S}_k^{\text{type}}\,|\beta\rangle_C \qquad \text{if pm} = a_{i_0} b^{i_0}_{B_0\beta'} \text{ and } C = B_0 \tag{A.12}$$

Now we can rewrite equation A.8 as

$$\hat{S}_k^{\text{type}}\,|\Psi\rangle = \sum_{\text{pm}} \text{pm} \bigotimes_{C\neq C'} \sum_{\beta} A_f[C,\beta,\text{pm}]\,|\beta\rangle_C \sum_{\beta} B_f[\text{type},k,C',\beta,\text{pm}]\,|\beta\rangle_{C'}\,. \tag{A.13}$$

Through this form, equation A.5 can be calculated easily, more precisely

$$\left\langle \frac{\partial \Psi}{\partial \mathrm{pm}^*} \middle| \hat{S}_i^{\mathrm{type}_1} \hat{S}_j^{\mathrm{type}_2} \middle| \Psi \right\rangle = \sum_{\mathrm{pm}'} \mathrm{pm}' \prod_{C \neq C_1 \neq C_2} \sum_{\beta} A_f[C, \beta, \mathrm{pm}]^* A_f[C, \beta, \mathrm{pm}'] \cdot \sum_{\beta} B_f[\mathrm{type}_1', i, C_1, \beta, \mathrm{pm}]^* A_f[C_1, \beta, \mathrm{pm}'] \cdot \sum_{\beta} A_f[C_2, \beta, \mathrm{pm}]^* B_f[\mathrm{type}_2, j, C_2, \beta, \mathrm{pm}'] \tag{A.14}$$

if the two spin operators act on different clusters, and

$$\left\langle \frac{\partial \Psi}{\partial \mathrm{pm}^*} \middle| \hat{S}_i^{\mathrm{type}_1} \hat{S}_j^{\mathrm{type}_2} \middle| \Psi \right\rangle = \sum_{\mathrm{pm}'} \mathrm{pm}' \prod_{C \neq C'} \sum_{\beta} A_f[C, \beta, \mathrm{pm}]^* A_f[C, \beta, \mathrm{pm}'] \cdot \sum_{\beta} B_f[\mathrm{type}_1', i, C', \beta, \mathrm{pm}]^* B_f[\mathrm{type}_2, i, C', \beta, \mathrm{pm}] \tag{A.15}$$

if they act on the same cluster. type_1' is given so, $\hat{S}_i^{\mathrm{type}_1 \dagger} = \hat{S}_i^{\mathrm{type}_1'}$.
Finding the matrix elements in the restricted basis to solve the eigenvalue equation is straightforward now

$$\left\langle \frac{\partial \Psi}{\partial \mathrm{pm}^*} \middle| \hat{S}_i^{\mathrm{type}_1} \hat{S}_j^{\mathrm{type}_2} \middle| \Psi \right\rangle_{\mathrm{pm},\mathrm{pm}'} = \prod_{C \neq C_1 \neq C_2} A_f[C, :, :]^\dagger A_f[C, :, :] \cdot B_f[\mathrm{type}_1', i, C_1, :, :]^\dagger A_f[C_1, :, :] \cdot A_f[C_2, :, :]^\dagger B_f[\mathrm{type}_2, j, C_2, :, :] \tag{A.16}$$

And equivalently for the other equation. The $A_f^\dagger A_f$, $B_f^\dagger A_f$, $A_f^\dagger B_f$ and $B_f^\dagger B_f$ products are matrix-products, the other products are Hadamard products.
In many cases, the $\prod A_f^\dagger A_f$ terms can be heavily simplified, easing the calculations. Using eq. 4.5, we find the following:

$$A_f[\mathrm{imp}, :, :]^\dagger A_f[\mathrm{imp}, :, :] = \left[\begin{array}{c|c} \begin{matrix} 1 & & \\ & \ddots & \\ & & 0 \end{matrix} & 0 \\ \hline 0 & \begin{matrix} 1 & & 1 \\ \vdots & & \vdots \\ 1 & & 1 \end{matrix} \end{array}\right] \tag{A.17}$$

$$A_f[\mathrm{B}_0,:,:]^\dagger A_f[\mathrm{B}_0,:,:] = \left[\begin{array}{c|c} \begin{array}{cc} 1 & \\ ? & ? \\ ? & 1 \end{array} & ? \\ \hline ? & \begin{array}{cc} 1 & \\ & 0 \\ 0 & \\ & 1 \end{array} \end{array}\right] \tag{A.18}$$

$$A_f[\mathrm{B},:,:]^\dagger A_f[\mathrm{B},:,:] = \left[\begin{array}{c|c} \begin{array}{cc} 1 & \\ ? & ? \\ ? & 1 \end{array} & ? \\ \hline ? & \begin{array}{cc} 1 & 1 \\ 1 & 1 \end{array} \end{array}\right] \qquad \forall B \neq B_0 \wedge \mathrm{imp} \tag{A.19}$$

So, we see, when $\prod A_f^\dagger A_f$ has the matrix product given by equation A.17, the total product reduces to this matrix. When the product also has the matrix product given by eq. A.18, the product reduces to the unity matrix.

It is now clear how to calculate the terms given by eq. A.5 and the first term of eq. 4.9 can be calculated. Now the eigenvalue problem in the reduced basis is ready to be solved. By iterating over the different B_0's and i_0's, we eventually converge to the DMET ground state or a local minimum.

B Perturbation expansion in the Kitaev - Heisenberg model on the honeycomb lattice

B.1 The stripy AF phase

In this chapter, the Kitaev-Heisenberg model is solved through the use of perturbation theory. The splitting of the Hamiltonian happens the same way as in ref. [20], and special thanks goes to G. Khaliullin for the extra explanation given through email.
We start with the perturbation expansion around the stripy AF solution. In the rotated basis (see figure 6.3), the bond interaction is given by eq. 6.5. In this perturbation expansion the unperturbed Hamiltonian ($\hat{H}_0$) is given by an Ising-like Hamiltonian, i.e. only the spin terms in z-direction are coupled. The perturbation ($\hat{V}$) is then composed of the terms in the x- and y-direction. This gives us

$$\hat{H}_{ij}^{(x)} = -(1-\alpha)\hat{\tilde{S}}_i^z\hat{\tilde{S}}_j^z + \lambda\left[(1-3\alpha)\hat{\tilde{S}}_i^x\hat{\tilde{S}}_j^x - (1-\alpha)\hat{\tilde{S}}_i^y\hat{\tilde{S}}_j^y\right] \tag{B.1}$$

$$\hat{H}_{ij}^{(y)} = -(1-\alpha)\hat{\tilde{S}}_i^z\hat{\tilde{S}}_j^z + \lambda\left[-(1-\alpha)\hat{\tilde{S}}_i^x\hat{\tilde{S}}_j^x + (1-3\alpha)\hat{\tilde{S}}_i^y\hat{\tilde{S}}_j^y\right] \tag{B.2}$$

$$\hat{H}_{ij}^{(z)} = (1-3\alpha)\hat{\tilde{S}}_i^z\hat{\tilde{S}}_j^z + \lambda\left[-(1-\alpha)\hat{\tilde{S}}_i^x\hat{\tilde{S}}_j^x - (1-\alpha)\hat{\tilde{S}}_i^y\hat{\tilde{S}}_j^y\right] \tag{B.3}$$

or

$$\hat{H}_{ij}^{(x)} = -(1-\alpha)\hat{\tilde{S}}_i^z\hat{\tilde{S}}_j^z + \lambda\left[\frac{1-2\alpha}{2}\left(\hat{\tilde{S}}_i^+\hat{\tilde{S}}_j^+ + \hat{\tilde{S}}_i^-\hat{\tilde{S}}_j^-\right) - \frac{\alpha}{2}\left(\hat{\tilde{S}}_i^+\hat{\tilde{S}}_j^- + \hat{\tilde{S}}_i^+\hat{\tilde{S}}_j^-\right)\right] \tag{B.4}$$

$$\hat{H}_{ij}^{(y)} = -(1-\alpha)\hat{\tilde{S}}_i^z\hat{\tilde{S}}_j^z + \lambda\left[-\frac{1-2\alpha}{2}\left(\hat{\tilde{S}}_i^+\hat{\tilde{S}}_j^+ + \hat{\tilde{S}}_i^-\hat{\tilde{S}}_j^-\right) - \frac{\alpha}{2}\left(\hat{\tilde{S}}_i^+\hat{\tilde{S}}_j^- + \hat{\tilde{S}}_i^+\hat{\tilde{S}}_j^-\right)\right] \tag{B.5}$$

$$\hat{H}_{ij}^{(z)} = (1-3\alpha)\hat{\tilde{S}}_i^z\hat{\tilde{S}}_j^z - \lambda\frac{1-\alpha}{2}\left[\hat{\tilde{S}}_i^+\hat{\tilde{S}}_j^- + \hat{\tilde{S}}_i^+\hat{\tilde{S}}_j^-\right]. \tag{B.6}$$

The strength of the perturbation is given by λ. When $\lambda = 0$, the system is unperturbed, and

the system at $\lambda = 1$ is the system of interest. The total Hamiltonian is given by

$$\hat{H} = \hat{H}_0 + \lambda \hat{V}. \tag{B.7}$$

At $\lambda = 0$, the ground state can be easily found in the range $\alpha \in [\frac{1}{3}, 1]$. This is also the range of interest for the stripy AF phase. In this range, the ground state of the unperturbed Ising-like system is ferromagnetic. More specific, the ground states are given by $|\uparrow\uparrow \cdots \uparrow\rangle$ and $|\downarrow\downarrow \cdots \downarrow\rangle$. This degeneracy will pose no difficulty for the perturbation expansion, as will be seen in the derivations. From now on, we will work with $\left|n^{(0)}\right\rangle = |\uparrow\uparrow \cdots \uparrow\rangle$ as ground state of the unperturbed Hamiltonian.

First, we calculate the ground state energy through perturbation expansion. The zeroth order energy of the system is given by $E_n^{(0)} = \left\langle n^{(0)}\middle|\hat{H}_0\middle|n^{(0)}\right\rangle$. Every spin has one bond of each type (x-type, y-type and z-type). Summing the energy per type and over all spins will double count all the bonds, so we divide by two. This gives us:

$$E_n^{(0)} = -\left(\frac{1}{8} + \frac{1}{8}\alpha\right) N, \tag{B.8}$$

with N the number of spins. The first order ground state energy is given by $E_n^{(1)} = \left\langle n^{(0)}\middle|\hat{V}\middle|n^{(0)}\right\rangle$. Since $\hat{V}$ consists of ladder operators acting on different spins, this correction vanishes.

The second order correction to the ground state energy is given by

$$E_n^{(2)} = \sum_{k \neq n} \frac{\left|\left\langle k^{(0)}\middle|\hat{V}\middle|n^{(0)}\right\rangle\right|^2}{E_n^{(0)} - E_k^{(0)}}. \tag{B.9}$$

Here $\left|k^{(0)}\right\rangle$ is the orthogonal complement of $\left|n^{(0)}\right\rangle$. The easiest set for $\left|k^{(0)}\right\rangle$ is the set of all configurations where each spin is distinctly up or down, e.g. $|\uparrow\downarrow\downarrow\uparrow \cdots \uparrow\rangle$, with the exception of the ground state. It is clear that most of the $\left\langle k^{(0)}\middle|\hat{V}\middle|n^{(0)}\right\rangle$ terms will be zero. The only exceptions to this are configurations where two spins along a x- or y-bond are flipped in comparison with the ground state. These are depicted in figure B.1 and will be represented by $|X\rangle$ and $|Y\rangle$.

Since $\left\langle \downarrow\downarrow \cdots \downarrow\middle|\hat{V}\middle|n^{(0)}\right\rangle = 0$, the degeneracy of the ground state poses no difficulty. The needed results are given by

$$\left\langle X\middle|\hat{V}\middle|n^{(0)}\right\rangle = \frac{1 - 2\alpha}{2} \tag{B.10}$$

$$\left\langle Y\middle|\hat{V}\middle|n^{(0)}\right\rangle = -\frac{1 - 2\alpha}{2} \tag{B.11}$$

$$E_n^{(0)} - E_k^{(0)} = -2\alpha. \tag{B.12}$$

(a) $|\mathrm{X}\rangle$ **(b)** $|\mathrm{Y}\rangle$

Figure B.1: Terms for which $\langle k^{(0)}|\hat{V}|n^{(0)}\rangle$ does not vanish. The full dots are spin up, the empty dots are spin down.

There are $N/2$ x-bonds and $N/2$ y-bonds in the lattice. This means there are thus $N/2$ different $|X\rangle$ states and $N/2$ different $|Y\rangle$ states. For the second order energy correction and the total energy up to second order, this eventually gives

$$E_n^{(2)} = N\left(-\frac{1}{8\alpha} + \frac{1}{2} - \frac{\alpha}{2}\right) \tag{B.13}$$

$$E_n \approx -\frac{N}{8}\left(5\alpha - 3 + \frac{1}{\alpha}\right) \tag{B.14}$$

To calculate properties of the stripy AF phase up to second order perturbation we need to know the ground state wave function up to second order corrections. The wave function is given by

$$|n(\lambda)\rangle = \left|n^{(0)}\right\rangle + \lambda\left|n^{(1)}\right\rangle + \lambda^2\left|n^{(2)}\right\rangle + \mathcal{O}(\lambda^3) \tag{B.15}$$

with

$$\left|n^{(1)}\right\rangle = \sum_{k\neq n} \frac{\left\langle k^{(0)}\middle|\hat{V}\middle|n^{(0)}\right\rangle}{E_n^{(0)} - E_k^{(0)}}\left|k^{(0)}\right\rangle \tag{B.16}$$

$$\begin{aligned}\left|n^{(2)}\right\rangle = &\sum_{k\neq n}\sum_{l\neq n} \frac{\left\langle k^{(0)}\middle|\hat{V}\middle|l^{(0)}\right\rangle\left\langle l^{(0)}\middle|\hat{V}\middle|n^{(0)}\right\rangle}{\left(E_n^{(0)} - E_k^{(0)}\right)\left(E_n^{(0)} - E_l^{(0)}\right)}\left|k^{(0)}\right\rangle \\ &- \sum_{k\neq n} \frac{\left\langle n^{(0)}\middle|\hat{V}\middle|n^{(0)}\right\rangle\left\langle k^{(0)}\middle|\hat{V}\middle|n^{(0)}\right\rangle}{\left(E_n^{(0)} - E_k^{(0)}\right)^2}\left|k^{(0)}\right\rangle \\ &- \frac{1}{2}\left|n^{(0)}\right\rangle \sum_{k\neq n} \frac{\left\langle n^{(0)}\middle|\hat{V}\middle|k^{(0)}\right\rangle\left\langle k^{(0)}\middle|\hat{V}\middle|n^{(0)}\right\rangle}{\left(E_n^{(0)} - E_k^{(0)}\right)^2}\end{aligned} \tag{B.17}$$

The expectation value of an operator up to second order in λ is then given by

$$\begin{aligned}\langle n(\lambda)|\hat{O}|n(\lambda)\rangle = &\left\langle n^{(0)}\middle|\hat{O}\middle|n^{(0)}\right\rangle + \lambda\left\langle n^{(0)}\middle|\hat{O}\middle|n^{(1)}\right\rangle + \lambda\left\langle n^{(1)}\middle|\hat{O}\middle|n^{(0)}\right\rangle \\ &+ \lambda^2\left\langle n^{(1)}\middle|\hat{O}\middle|n^{(1)}\right\rangle + \lambda^2\left\langle n^{(0)}\middle|\hat{O}\middle|n^{(2)}\right\rangle + \lambda^2\left\langle n^{(2)}\middle|\hat{O}\middle|n^{(0)}\right\rangle + \mathcal{O}(\lambda^3).\end{aligned} \tag{B.18}$$

$\left|n^{(1)}\right\rangle$ can be readily found by the previous results and is given by

$$\left|n^{(1)}\right\rangle = \sum_{|X\rangle}\left(\frac{1}{2} - \frac{1}{4\alpha}\right)|X\rangle - \sum_{|Y\rangle}\left(\frac{1}{2} - \frac{1}{4\alpha}\right)|Y\rangle\,. \tag{B.19}$$

For $\left|n^{(2)}\right\rangle$, we note that $\left\langle n^{(0)}\middle|\hat{V}\middle|n^{(0)}\right\rangle = 0$. The last term is also easy to calculate and is given by

$$\frac{1}{2}\left|n^{(0)}\right\rangle \sum_{k\neq n}\frac{\left\langle n^{(0)}\middle|\hat{V}\middle|k^{(0)}\right\rangle\left\langle k^{(0)}\middle|\hat{V}\middle|n^{(0)}\right\rangle}{\left(E_n^{(0)} - E_k^{(0)}\right)^2} = \frac{1}{2}\left(\frac{1}{2} - \frac{1}{4\alpha}\right)^2 N\left|n^{(0)}\right\rangle. \tag{B.20}$$

For the first term in eq. B.21, we need to find for which states $\left\langle k^{(0)}\middle|\hat{V}\middle|l^{(0)}\right\rangle \neq 0$, where $\left|l^{(0)}\right\rangle = |X\rangle\,, |Y\rangle$. This is possible when $\left|k^{(0)}\right\rangle$ is a state where the spins are flipped on two different x- and/or y-bonds. One bond should correspond with the flipped spins of $\left|l^{(0)}\right\rangle$, andt the other bond should be disconnected from the first. 4 spins are thus flipped in comparison with the ground state. These states will be represented by $|X, X\rangle$, $|Y, Y\rangle$ and $|X, Y\rangle$ depending on the spins flipped. Another type of state where $\left\langle k^{(0)}\middle|\hat{V}\middle|l^{(0)}\right\rangle \neq 0$ is given by $|X\rangle$ and $|Y\rangle$ where one flipped spin migrates to a neighbouring site. This are depicted in figure B.2 and

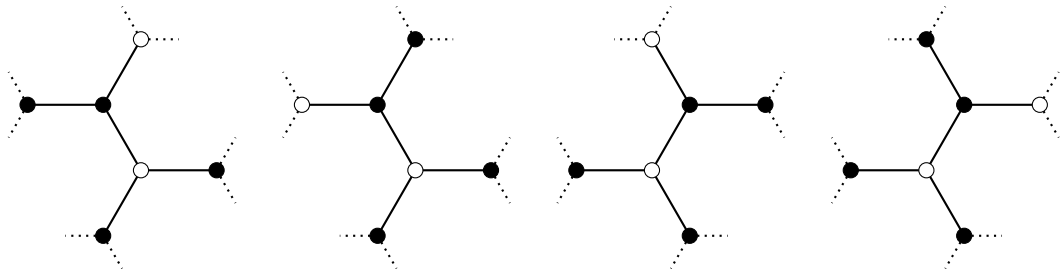

(a) $|\mathrm{X} \to \mathrm{Y}\rangle$ **(b)** $|\mathrm{X} \to \mathrm{Z}\rangle$ **(c)** $|\mathrm{Y} \to \mathrm{X}\rangle$ **(d)** $|\mathrm{Y} \to \mathrm{Z}\rangle$

Figure B.2: Terms for which $\left\langle k^{(0)}\middle|\hat{V}\middle|l^{(0)}\right\rangle$ does not vanish. The full dots are spin up, the empty dots are spin down.

the captions contain their names. This gives us

$$\langle X \to Y|\hat{V}|X\rangle = -\frac{\alpha}{2}$$

$$\langle X \to Z|\hat{V}|X\rangle = -\frac{1-\alpha}{2}$$

$$\langle Y \to X|\hat{V}|Y\rangle = -\frac{\alpha}{2}$$

$$\langle Y \to Z|\hat{V}|Y\rangle = -\frac{1-\alpha}{2} \qquad \text{with}$$

$$E_n^{(0)} - E_k^{(0)} = -(1+\alpha)$$

For the second order correction of the ground state, we find

$$\begin{aligned}\left|n^{(2)}\right\rangle = &\sum_{\substack{|X,X\rangle \\ \left|k^{(0)}\right\rangle \in |Y,Y\rangle \\ |X,Y\rangle}} \cdots \left|k^{(0)}\right\rangle + \sum_{|X\to Y\rangle} -\frac{\alpha(1-2\alpha)}{8\alpha(1+\alpha)}\,|X\to Y\rangle \\ &+ \sum_{|X\to Z\rangle} -\frac{(1-\alpha)(1-2\alpha)}{8\alpha(1+\alpha)}\,|X\to Z\rangle + \sum_{|Y\to X\rangle} \frac{\alpha(1-2\alpha)}{8\alpha(1+\alpha)}\,|Y\to X\rangle \\ &+ \sum_{|Y\to Z\rangle} \frac{(1-\alpha)(1-2\alpha)}{8\alpha(1+\alpha)}\,|Y\to Z\rangle - \frac{1}{2}\left(\frac{1}{2}-\frac{1}{4\alpha}\right)^2 N\left|n^{(0)}\right\rangle.\end{aligned} \tag{B.21}$$

The coefficients for $|X,X\rangle$, $|Y,Y\rangle$ and $|X,Y\rangle$ are not calculated since these terms will be of no importance for the properties to be calculated.

First, we will calculate the NN correlation between the spins. We calculate $\left\langle \hat{\tilde{\mathbf{S}}}_i \cdot \hat{\tilde{\mathbf{S}}}_j \right\rangle$ with i and j two neighbouring sites along a x-, y- or z-bond. To find this expectation value up to second order we use eq. B.18.

Along an x-bond we have

$$\left\langle n^{(0)}\middle|\hat{\tilde{S}}_i^x \hat{\tilde{S}}_j^x\middle|n^{(0)}\right\rangle = 0$$

$$\left\langle n^{(1)}\middle|\hat{\tilde{S}}_i^x \hat{\tilde{S}}_j^x\middle|n^{(0)}\right\rangle = \frac{1}{4}\left(\frac{1}{2}-\frac{1}{4\alpha}\right)$$

$$\left\langle n^{(1)}\middle|\hat{\tilde{S}}_i^x \hat{\tilde{S}}_j^x\middle|n^{(1)}\right\rangle = 0$$

$$\left\langle n^{(2)}\middle|\hat{\tilde{S}}_i^x \hat{\tilde{S}}_j^x\middle|n^{(0)}\right\rangle = 0$$

and thus $\left\langle \hat{\tilde{S}}_i^x \hat{\tilde{S}}_j^x \right\rangle = \frac{1}{2}\left(\frac{1}{2} - \frac{1}{4\alpha}\right)$ up to second order,

$$\left\langle n^{(0)} \middle| \hat{\tilde{S}}_i^y \hat{\tilde{S}}_j^y \middle| n^{(0)} \right\rangle = 0$$

$$\left\langle n^{(1)} \middle| \hat{\tilde{S}}_i^y \hat{\tilde{S}}_j^y \middle| n^{(0)} \right\rangle = -\frac{1}{4}\left(\frac{1}{2} - \frac{1}{4\alpha}\right)$$

$$\left\langle n^{(1)} \middle| \hat{\tilde{S}}_i^y \hat{\tilde{S}}_j^y \middle| n^{(1)} \right\rangle = 0$$

$$\left\langle n^{(2)} \middle| \hat{\tilde{S}}_i^y \hat{\tilde{S}}_j^y \middle| n^{(0)} \right\rangle = 0$$

and thus $\left\langle \hat{\tilde{S}}_i^y \hat{\tilde{S}}_j^y \right\rangle = -\frac{1}{2}\left(\frac{1}{2} - \frac{1}{4\alpha}\right)$ up to second order,

$$\left\langle n^{(0)} \middle| \hat{\tilde{S}}_i^z \hat{\tilde{S}}_j^z \middle| n^{(0)} \right\rangle = \frac{1}{4}$$

$$\left\langle n^{(1)} \middle| \hat{\tilde{S}}_i^z \hat{\tilde{S}}_j^z \middle| n^{(0)} \right\rangle = 0$$

$$\left\langle n^{(1)} \middle| \hat{\tilde{S}}_i^z \hat{\tilde{S}}_j^z \middle| n^{(1)} \right\rangle = \left(\frac{1}{2} - \frac{1}{4\alpha}\right)^2 \left(\frac{N-4}{4}\right)$$

$$\left\langle n^{(2)} \middle| \hat{\tilde{S}}_i^z \hat{\tilde{S}}_j^z \middle| n^{(0)} \right\rangle = -\frac{1}{8} N \left(\frac{1}{2} - \frac{1}{4\alpha}\right)^2$$

and thus $\left\langle \hat{\tilde{S}}_i^z \hat{\tilde{S}}_j^z \right\rangle = \frac{1}{4} - \left(\frac{1}{2} - \frac{1}{4\alpha}\right)^2$ up to second order. Finally, this gives us:

$$\left\langle \hat{\tilde{\mathbf{S}}}_i \cdot \hat{\tilde{\mathbf{S}}}_j \right\rangle = \frac{1}{4} - \left(\frac{1}{2} - \frac{1}{4\alpha}\right)^2 \tag{B.22}$$

$$\left\langle \hat{\mathbf{S}}_i \cdot \hat{\mathbf{S}}_j \right\rangle = -\frac{1}{4} + \left(\frac{1}{2} - \frac{1}{4\alpha}\right) + \left(\frac{1}{2} - \frac{1}{4\alpha}\right)^2 \tag{B.23}$$

Equivalent calculations can be done for the y- and z-bonds. For the y-bond, this gives us

$$\left\langle \hat{\tilde{S}}_i^x \hat{\tilde{S}}_j^x \right\rangle = -\frac{1}{2}\left(\frac{1}{2} - \frac{1}{4\alpha}\right) \tag{B.24}$$

$$\left\langle \hat{\tilde{S}}_i^y \hat{\tilde{S}}_j^y \right\rangle = \frac{1}{2}\left(\frac{1}{2} - \frac{1}{4\alpha}\right) \tag{B.25}$$

$$\left\langle \hat{\tilde{S}}_i^z \hat{\tilde{S}}_j^z \right\rangle = \frac{1}{4} - \left(\frac{1}{2} - \frac{1}{4\alpha}\right)^2 \tag{B.26}$$

$$\left\langle \hat{\tilde{\mathbf{S}}}_i \cdot \hat{\tilde{\mathbf{S}}}_j \right\rangle = \frac{1}{4} - \left(\frac{1}{2} - \frac{1}{4\alpha}\right)^2 \tag{B.27}$$

$$\left\langle \hat{\mathbf{S}}_i \cdot \hat{\mathbf{S}}_j \right\rangle = -\frac{1}{4} + \left(\frac{1}{2} - \frac{1}{4\alpha}\right) + \left(\frac{1}{2} - \frac{1}{4\alpha}\right)^2 \tag{B.28}$$

and for the z-bond

$$\left\langle \hat{\tilde{S}}_i^x \hat{\tilde{S}}_j^x \right\rangle = 0 \tag{B.29}$$

$$\left\langle \hat{\tilde{S}}_i^y \hat{\tilde{S}}_j^y \right\rangle = 0 \tag{B.30}$$

$$\left\langle \hat{\tilde{S}}_i^z \hat{\tilde{S}}_j^z \right\rangle = \frac{1}{4} - 2\left(\frac{1}{2} - \frac{1}{4\alpha}\right)^2 \tag{B.31}$$

$$\left\langle \hat{\tilde{\mathbf{S}}}_i \cdot \hat{\tilde{\mathbf{S}}}_j \right\rangle = \frac{1}{4} - 2\left(\frac{1}{2} - \frac{1}{4\alpha}\right)^2 \tag{B.32}$$

$$\left\langle \hat{\mathbf{S}}_i \cdot \hat{\mathbf{S}}_j \right\rangle = \frac{1}{4} - 2\left(\frac{1}{2} - \frac{1}{4\alpha}\right)^2. \tag{B.33}$$

These results give us

$$\left\langle \hat{\tilde{\mathbf{S}}}_i \cdot \hat{\tilde{\mathbf{S}}}_j \right\rangle = \frac{1}{4} - \frac{3}{4}\left(\frac{1}{2} - \frac{1}{4\alpha}\right)^2 \tag{B.34}$$

$$\left\langle \hat{\tilde{S}}_i^\gamma \hat{\tilde{S}}_j^\gamma \right\rangle = \frac{1}{12} + \frac{1}{6\alpha}\left(\frac{1}{2} - \frac{1}{4\alpha}\right) \tag{B.35}$$

$$\left\langle \hat{\mathbf{S}}_i \cdot \hat{\mathbf{S}}_j \right\rangle = -\frac{1}{12} + \frac{2}{3}\left(\frac{1}{2} - \frac{1}{4\alpha}\right). \tag{B.36}$$

We also calculate the squared total spin in the original basis and the rotated basis. First, we calculate $\left\langle \hat{\tilde{S}}_{\text{tot}}^2 \right\rangle$. It is easily found that

$$\left\langle n^{(0)} \middle| \hat{\tilde{S}}_{\text{tot}}^2 \middle| n^{(0)} \right\rangle = \frac{N(N+2)}{4} \tag{B.37}$$

and

$$\left\langle n^{(1)} \middle| \hat{\tilde{S}}_{\text{tot}}^2 \middle| n^{(0)} \right\rangle = 0. \tag{B.38}$$

Since the operator $\hat{\tilde{S}}_{\text{tot}}^2$ can only migrate flipped spins and not change the total number of up and down spins in the rotated basis. Since the operator has only the possibility to migrate one spin at a time, $\left\langle n^{(1)} \middle| \hat{\tilde{S}}_{\text{tot}}^2 \middle| n^{(1)} \right\rangle$ can also be readily calculated. The only terms that will be nonzero are $\langle X|\hat{\tilde{S}}_{\text{tot}}^2|Y\rangle$ and $\langle Y|\hat{\tilde{S}}_{\text{tot}}^2|X\rangle$, where X and Y are adjacent bonds, $\langle X|\hat{\tilde{S}}_{\text{tot}}^2|X\rangle$ and $\langle Y|\hat{\tilde{S}}_{\text{tot}}^2|Y\rangle$. The results are

$$\langle X|\hat{\tilde{S}}_{\text{tot}}^2|Y\rangle = \langle Y|\hat{\tilde{S}}_{\text{tot}}^2|X\rangle = 1, \tag{B.39}$$

$$\langle X|\hat{\tilde{S}}_{\text{tot}}^2|X\rangle = \langle Y|\hat{\tilde{S}}_{\text{tot}}^2|Y\rangle = \frac{N^2}{4} - \frac{3}{2}N + 4. \tag{B.40}$$

Since there are $\frac{N}{2}$ different x-bonds with each 2 neighbouring y-bonds, there are N $\langle X|\hat{\tilde{S}}^2_{\text{tot}}|Y\rangle$ and N $\langle Y|\hat{\tilde{S}}^2_{\text{tot}}|X\rangle$ terms that are nonzero. There are also $\frac{N}{2}$ $\langle X|\hat{\tilde{S}}^2_{\text{tot}}|X\rangle$ and $\frac{N}{2}$ $\langle Y|\hat{\tilde{S}}^2_{\text{tot}}|Y\rangle$ nonzero terms. This gives us

$$\begin{aligned}\left\langle n^{(1)}\middle|\hat{\tilde{S}}^2_{\text{tot}}\middle|n^{(1)}\right\rangle &= \left(\frac{1}{2}-\frac{1}{4\alpha}\right)^2\left[N\left(\frac{N^2}{4}-\frac{3}{2}N+4\right)-2N\right] \\ &= \left(\frac{1}{2}-\frac{1}{4\alpha}\right)^2\left[\frac{N^3}{4}-\frac{3}{2}N^2+2N\right]\end{aligned} \tag{B.41}$$

Since the squared total spin operator in the rotated basis is not able to change the total number of flipped spins, only the $\left|n^{(0)}\right\rangle$ term will be important in eq. B.21 for second order perturbation. We get

$$\left\langle n^{(0)}\middle|\hat{\tilde{S}}^2_{\text{tot}}\middle|n^{(2)}\right\rangle = -\frac{1}{2}\left(\frac{1}{2}-\frac{1}{4\alpha}\right)^2\frac{N^2(N+2)}{4}, \tag{B.42}$$

and finally the squared total spin in the rotated basis (normalized to a maximal value of 1) is given by

$$\left\langle \hat{\tilde{S}}^2_{\text{tot}}\right\rangle = 1-\left(\frac{1}{2}-\frac{1}{4\alpha}\right)^2\frac{8(N-1)}{N+2} \tag{B.43}$$

Finally, we also want to calculate the expectation value of the squared total spin in the original basis. The calculation for the zeroth order has been discussed in section 6.3 and is given in eq. 6.7. Unnormalized to 1 this gives us

$$\left\langle n^{(0)}\middle|U^\dagger\hat{S}^2_{\text{tot}}U\middle|n^{(0)}\right\rangle = \frac{N}{2}, \tag{B.44}$$

with U the basis transformation from rotated to original basis. For $\left\langle n^{(0)}\middle|U^\dagger\hat{S}^2_{\text{tot}}U\middle|n^{(1)}\right\rangle$, we calculate $\left\langle n^{(0)}\middle|U^\dagger\hat{S}^2_{\text{tot}}U\middle|X\right\rangle$ and $\left\langle n^{(0)}\middle|U^\dagger\hat{S}^2_{\text{tot}}U\middle|Y\right\rangle$. For e.g. $\left\langle n^{(0)}\middle|U^\dagger\hat{S}^2_{\text{tot}}U\middle|X\right\rangle$ only $\left\langle n^{(0)}\middle|U^\dagger 2\hat{\mathbf{S}}_i\cdot\hat{\mathbf{S}}_jU\middle|X\right\rangle$ will play a roll, with i and j the two sites along the x-bond with flipped spins of $|X\rangle$. Along an x-bond $U^\dagger 2\hat{\mathbf{S}}_i\cdot\hat{\mathbf{S}}_jU = \hat{\tilde{S}}^x_i\hat{\tilde{S}}^x_j - \hat{\tilde{S}}^y_i\hat{\tilde{S}}^y_j - \hat{\tilde{S}}^z_i\hat{\tilde{S}}^z_j$ while along an y-bond $U^\dagger 2\hat{\mathbf{S}}_i\cdot\hat{\mathbf{S}}_jU = -\hat{\tilde{S}}^x_i\hat{\tilde{S}}^x_j + \hat{\tilde{S}}^y_i\hat{\tilde{S}}^y_j - \hat{\tilde{S}}^z_i\hat{\tilde{S}}^z_j$. This gives us

$$\left\langle n^{(0)}\middle|U^\dagger\hat{S}^2_{\text{tot}}U\middle|X\right\rangle = 1 \tag{B.45}$$

$$\left\langle n^{(0)}\middle|U^\dagger\hat{S}^2_{\text{tot}}U\middle|Y\right\rangle = -1 \tag{B.46}$$

and

$$\left\langle n^{(0)}\middle|U^\dagger\hat{S}^2_{\text{tot}}U\middle|n^{(1)}\right\rangle = N\left(\frac{1}{2}-\frac{1}{4\alpha}\right). \tag{B.47}$$

Furthermore, we find

$$\begin{aligned}\langle X|U^\dagger \hat{S}^2_{\text{tot}} U|X\rangle &= \frac{N}{2} - 2\left[-2\left(\frac{N}{2}-1\right)\frac{1}{4} + 2\left(\frac{N}{2}-1\right)\frac{1}{4}\right] \\ &= \frac{N}{2}\end{aligned} \tag{B.48}$$

$$\langle Y|U^\dagger \hat{S}^2_{\text{tot}} U|Y\rangle = \frac{N}{2} \tag{B.49}$$

$$\langle X|U^\dagger \hat{S}^2_{\text{tot}} U|Y\rangle = -1. \tag{B.50}$$

The first result is obtained through the result of eq. B.44 and correcting for the wrongly calculated $U^\dagger \hat{\mathbf{S}}_i \cdot \hat{\mathbf{S}}_j U$. The last result again only applies for $|X\rangle$ and $|Y\rangle$ states where the flipped spins neighbour each other. The sign changes compared to eq. B.39 comes from the basis transformation. We find

$$\left\langle n^{(1)}\middle|U^\dagger \hat{S}^2_{\text{tot}} U\middle|n^{(1)}\right\rangle = \frac{N^2}{2}\left(\frac{1}{2}-\frac{1}{4\alpha}\right)^2 + 2N\left(\frac{1}{2}-\frac{1}{4\alpha}\right)^2. \tag{B.51}$$

The last term we need to calculate is $\left\langle n^{(0)}\middle|U^\dagger \hat{S}^2_{\text{tot}} U\middle|n^{(2)}\right\rangle$. Since the operator can only flip 2 spins at a time, it is clear that the first term in eq. B.21 will have no contribution. For $|X \to Y\rangle$ and $|Y \to X\rangle$, $U^\dagger \hat{\mathbf{S}}_i \cdot \hat{\mathbf{S}}_j U$ equals to $-\hat{\tilde{S}}^x_i \hat{\tilde{S}}^x_j - \hat{\tilde{S}}^y_i \hat{\tilde{S}}^y_j + \hat{\tilde{S}}^z_i \hat{\tilde{S}}^z_j$ for i and j the sites of the flipped spins. Written out in ladder operators, $\hat{\tilde{S}}^+_i \hat{\tilde{S}}^+_j$ will vanish for this scalar product. $|X \to Y\rangle$ and $|Y \to X\rangle$ will thus also have no contribution. Only the $|X \to Z\rangle$, $|X \to Z\rangle$ and $\left|n^{(0)}\right\rangle$ terms will contribute. The contribution of the last term is trivial. For $|X \to Z\rangle$, $U^\dagger \hat{\mathbf{S}}_i \cdot \hat{\mathbf{S}}_j U$ equals to $-\hat{\tilde{S}}^x_i \hat{\tilde{S}}^x_j + \hat{\tilde{S}}^y_i \hat{\tilde{S}}^y_j - \hat{\tilde{S}}^z_i \hat{\tilde{S}}^z_j$; for $|Y \to Z\rangle$, $U^\dagger \hat{\mathbf{S}}_i \cdot \hat{\mathbf{S}}_j U$ equals to $\hat{\tilde{S}}^x_i \hat{\tilde{S}}^x_j - \hat{\tilde{S}}^y_i \hat{\tilde{S}}^y_j - \hat{\tilde{S}}^z_i \hat{\tilde{S}}^z_j$ for i and j the sites of the flipped spins. This gives us

$$\left\langle n^{(0)}\middle|U^\dagger \hat{S}^2_{\text{tot}} U\middle|X \to Z\right\rangle = -1 \tag{B.52}$$

$$\left\langle n^{(0)}\middle|U^\dagger \hat{S}^2_{\text{tot}} U\middle|Y \to Z\right\rangle = 1 \tag{B.53}$$

Since there are N different $|X \to Z\rangle$ states and N different $|Y \to Z\rangle$ states, we get

$$\left\langle n^{(0)}\middle|U^\dagger \hat{S}^2_{\text{tot}} U\middle|n^{(2)}\right\rangle = N\frac{(1-\alpha)(1-2\alpha)}{4\alpha(1+\alpha)} - \frac{N^2}{4}\left(\frac{1}{2}-\frac{1}{4\alpha}\right)^2. \tag{B.54}$$

Eventually, the squared total spin in the original basis normalized to a maximal value of 1 is given by

$$\left\langle \hat{S}^2_{\text{tot}}\right\rangle = \frac{1}{N/2+1}\left[1 + 4\left(\frac{1}{2}-\frac{1}{4\alpha}\right) + 4\left(\frac{1}{2}-\frac{1}{4\alpha}\right)^2 + \frac{(1-\alpha)(1-2\alpha)}{\alpha(1+\alpha)}\right]. \tag{B.55}$$

B.2 The Néel AF phase

In this section, the ground state energy of the Néel AF phase is calculated through second order perturbation. We look at the bond interactions in the original basis given in eq. 6.3. The interactions of the spin components in the z-direction are again the unperturbed Hamiltonian, while the other interactions are the perturbation. The bond interactions are thus given by

$$\hat{H}_{ij}^{(x)} = (1-\alpha)\hat{\tilde{S}}_i^z\hat{\tilde{S}}_j^z + \lambda\left[-\frac{\alpha}{2}\left(\hat{\tilde{S}}_i^+\hat{\tilde{S}}_j^+ + \hat{\tilde{S}}_i^-\hat{\tilde{S}}_j^-\right) + \frac{1-2\alpha}{2}\left(\hat{\tilde{S}}_i^+\hat{\tilde{S}}_j^- + \hat{\tilde{S}}_i^+\hat{\tilde{S}}_j^-\right)\right] \tag{B.56}$$

$$\hat{H}_{ij}^{(y)} = (1-\alpha)\hat{\tilde{S}}_i^z\hat{\tilde{S}}_j^z + \lambda\left[\frac{\alpha}{2}\left(\hat{\tilde{S}}_i^+\hat{\tilde{S}}_j^+ + \hat{\tilde{S}}_i^-\hat{\tilde{S}}_j^-\right) + \frac{1-2\alpha}{2}\left(\hat{\tilde{S}}_i^+\hat{\tilde{S}}_j^- + \hat{\tilde{S}}_i^+\hat{\tilde{S}}_j^-\right)\right] \tag{B.57}$$

$$\hat{H}_{ij}^{(z)} = (1-3\alpha)\hat{\tilde{S}}_i^z\hat{\tilde{S}}_j^z + \lambda\frac{1-\alpha}{2}\left[\hat{\tilde{S}}_i^+\hat{\tilde{S}}_j^- + \hat{\tilde{S}}_i^+\hat{\tilde{S}}_j^-\right]. \tag{B.58}$$

At $\lambda = 0$, the ground state can be easily found in the region $\alpha \in [0, \frac{1}{3}]$ and is given by a classical AF solution. The zeroth order wave solution $\left|n^{(0)}\right\rangle$ is thus given by the state where every spin is the opposite of its neighbours. The zeroth order ground state energy is given by

$$E_n^{(0)} = -\frac{N}{8}(3-5\alpha), \tag{B.59}$$

where N is the number of spins. The first order energy correction is given by

$$E_n^{(1)} = \left\langle n^{(0)}\middle|\hat{V}\middle|n^{(0)}\right\rangle = 0 \tag{B.60}$$

The second order correction on the ground state energy is given by eq. B.9. Here $\left|k^{(0)}\right\rangle$ is again the orthogonal complement of $\left|n^{(0)}\right\rangle$. It is again clear that most of the $\left\langle k^{(0)}\middle|\hat{V}\middle|n^{(0)}\right\rangle$ terms will be zero. The only exceptions to this are configurations where two spins along a x-, y- or z-bond are switched in comparison with the ground state. These states will be represented by $|X\rangle$, $|Y\rangle$ and $|Z\rangle$. The following results are found:

$$\left\langle X\middle|\hat{V}\middle|n^{(0)}\right\rangle = \left\langle Y\middle|\hat{V}\middle|n^{(0)}\right\rangle = \frac{1-2\alpha}{2} \tag{B.61}$$

$$\left\langle Z\middle|\hat{V}\middle|n^{(0)}\right\rangle = \frac{1-\alpha}{2} \tag{B.62}$$

$$E_n^{(0)} - E_{|X\rangle}^{(0)} = E_n^{(0)} - E_{|Y\rangle}^{(0)} = -2(1-2\alpha) \tag{B.63}$$

$$E_n^{(0)} - E_{|Z\rangle}^{(0)} = -2(1-\alpha). \tag{B.64}$$

This finally gives us

$$E_n^{(2)} = -\frac{N}{16}(3-5\alpha) \tag{B.65}$$

$$E_n = -\frac{3N}{16}(3-5\alpha). \tag{B.66}$$

Bibliography

[1]W. Metzner and D. Vollhardt, "Correlated lattice fermions in $d = \infty$ dimensions", Phys. Rev. Lett. **62**, 324–327 (1989).

[2]A. Georges and W. Krauth, "Numerical solution of the $d = \infty$ hubbard model: evidence for a mott transition", Phys. Rev. Lett. **69**, 1240–1243 (1992).

[3]A. Georges, G. Kotliar, W. Krauth, and M. J. Rozenberg, "Dynamical mean-field theory of strongly correlated fermion systems and the limit of infinite dimensions", Rev. Mod. Phys. **68**, 13–125 (1996).

[4]D. Zgid and G. K.-L. Chan, "Dynamical mean-field theory from a quantum chemical perspective", The Journal of Chemical Physics **134**, 094115–094115 (2011).

[5]G. Knizia and G. K.-L. Chan, "Density matrix embedding: a simple alternative to dynamical mean-field theory", Phys. Rev. Lett. **109**, 186404 (2012).

[6]G. Knizia and G. K.-L. Chan, "Density matrix embedding: a strong-coupling quantum embedding theory", Journal of Chemical Theory and Computation **9**, PMID: 26587604, 1428–1432 (2013).

[7]G. H. Booth and G. K.-L. Chan, "Spectral functions of strongly correlated extended systems via an exact quantum embedding", Phys. Rev. B **91**, 155107 (2015).

[8]S. Wouters, C. A. Jiménez-Hoyos, and G. K.-L. Chan, "Five years of density matrix embedding theory", ArXiv e-prints (2016).

[9]B.-X. Zheng and G. K.-L. Chan, "Ground-state phase diagram of the square lattice hubbard model from density matrix embedding theory", Phys. Rev. B **93**, 035126 (2016).

[10]J. P. F. LeBlanc, A. E. Antipov, F. Becca, I. W. Bulik, G. K.-L. Chan, C.-M. Chung, Y. Deng, M. Ferrero, T. M. Henderson, C. A. Jiménez-Hoyos, E. Kozik, X.-W. Liu, A. J. Millis, N. V. Prokof'ev, M. Qin, G. E. Scuseria, H. Shi, B. V. Svistunov, L. F. Tocchio, I. S. Tupitsyn, S. R. White, S. Zhang, B.-X. Zheng, Z. Zhu, and E. Gull, "Solutions of the two-dimensional hubbard model: benchmarks and results from a wide range of numerical algorithms", Phys. Rev. X **5**, 041041 (2015).

[11]T. Tsuchimochi, M. Welborn, and T. Van Voorhis, "Density matrix embedding in an antisymmetrized geminal power bath", The Journal of Chemical Physics **143**, 024107 (2015) http://dx.doi.org/10.1063/1.4926650".

[12]B. Sandhoefer and G. Kin-Lic Chan, "Density matrix embedding theory for interacting electron-phonon systems", ArXiv e-prints (2016).

[13]Z. Fan and Q.-l. Jie, "Cluster density matrix embedding theory for quantum spin systems", Phys. Rev. B **91**, 195118 (2015).

[14]J. Qin, Q. Jie, and Z. Fan, "Implementing the density matrix embedding theory with the hierarchical mean-field approach", Computer Physics Communications, – (2016).

[15]S. Wouters, C. A. Jiménez-Hoyos, Q. Sun, and G. Kin-Lic Chan, "A practical guide to density matrix embedding theory in quantum chemistry", ArXiv e-prints (2016).

[16]G. Knizia, "Intrinsic Atomic Orbitals: An Unbiased Bridge between Quantum Theory and Chemical Concepts", Journal of Chemical Theory and Computation **9**, PMID: 26583402, 4834–4843 (2013).

[17]Q. Chen, G. H. Booth, S. Sharma, G. Knizia, and G. K.-L. Chan, "Intermediate and spin-liquid phase of the half-filled honeycomb Hubbard model", Phys. Rev. B **89**, 165134, 165134 (2014).

[18]I. W. Bulik, W. Chen, and G. E. Scuseria, "Electron correlation in solids via density embedding theory", "The Journal of Chemical Physics" **141**, 054113, 054113 (2014).

[19]J. Richter and J. Schulenburg, "The spin-1/2 j1–j2 heisenberg antiferromagnet on the square lattice:exact diagonalization for n=40 spins", The European Physical Journal B **73**, 117–124 (2009).

[20]J. Chaloupka, G. Jackeli, and G. Khaliullin, "Kitaev-Heisenberg Model on a Honeycomb Lattice: Possible Exotic Phases in Iridium Oxides A_2IrO_3", Physical Review Letters **105**, 027204, 027204 (2010).

[21]*The theory of magnetism i* (Springer-Verlag Berin Heidelberg New York Tokyo, 1981).

[22]*Theory of magnetism* (Technische Universität Dresden, Institute for Theoretical Physics, 2015).

[23]C. Lhuillier, "Frustrated Quantum Magnets", eprint arXiv:cond-mat/0502464 (2005).

[24]M. P. Gelfand, R. R. P. Singh, and D. A. Huse, "Zero-temperature ordering in two-dimensional frustrated quantum heisenberg antiferromagnets", Phys. Rev. B **40**, 10801–10809 (1989).

[25]G. Misguich and C. Lhuillier, "Two-dimensional quantum antiferromagnets", eprint arXiv:cond-mat/0310405 (2003).

[26]W. M. C. Foulkes, L. Mitas, R. J. Needs, and G. Rajagopal, "Quantum monte carlo simulations of solids", Rev. Mod. Phys. **73**, 33–83 (2001).

[27]S. Baroni and S. Moroni, "Reptation quantum monte carlo: a method for unbiased ground-state averages and imaginary-time correlations", Phys. Rev. Lett. **82**, 4745–4748 (1999).

[28]J. F. Corney and P. D. Drummond, "Gaussian quantum monte carlo methods for fermions and bosons", Phys. Rev. Lett. **93**, 260401 (2004).

[29]J. A. Barker, "A quantum-statistical monte carlo method; path integrals with boundary conditions", The Journal of Chemical Physics **70**, 2914–2918 (1979).

[30]C. J. Umrigar, K. G. Wilson, and J. W. Wilkins, "Optimized trial wave functions for quantum monte carlo calculations", Phys. Rev. Lett. **60**, 1719–1722 (1988).

[31]R. Darradi, O. Derzhko, R. Zinke, J. Schulenburg, S. E. Krüger, and J. Richter, "Ground state phases of the spin-1/2 J_1-J_2 Heisenberg antiferromagnet on the square lattice: A high-order coupled cluster treatment", Phys. Rev. B **78**, 214415, 214415 (2008).

[32]S. E. Krüger, R. Darradi, J. Richter, and D. J. J. Farnell, "Direct calculation of the spin stiffness of the spin-$\frac{1}{2}$ heisenberg antiferromagnet on square, triangular, and cubic lattices using the coupled-cluster method", Phys. Rev. B **73**, 094404 (2006).

[33]C. Zeng, D. J. J. Farnell, and R. F. Bishop, "An efficient implementation of high-order coupled-cluster techniques applied to quantum magnets", Journal of Statistical Physics **90**, 327–361 (1998).

[34]S. E. Krüger, J. Richter, J. Schulenburg, D. J. J. Farnell, and R. F. Bishop, "Quantum phase transitions of a square-lattice heisenberg antiferromagnet with two kinds of nearest-neighbor bonds: a high-order coupled-cluster treatment", Phys. Rev. B **61**, 14607–14615 (2000).

[35]D. J. J. Farnell, J. Schulenburg, J. Richter, and K. A. Gernoth, "High-order coupled cluster calculations via parallel processing: an illustration for cav4o9", Phys. Rev. B **72**, 172408 (2005).

[36]S. R. White, "Density matrix formulation for quantum renormalization groups", Phys. Rev. Lett. **69**, 2863–2866 (1992).

[37]S. R. White, "Density-matrix algorithms for quantum renormalization groups", Phys. Rev. B **48**, 10345–10356 (1993).

[38]H.-C. Jiang, H. Yao, and L. Balents, "Spin liquid ground state of the spin-(1)/(2) square J_1-J_2 Heisenberg model", Phys. Rev. B **86**, 024424, 024424 (2012).

[39]G. Vidal, "Entanglement renormalization", Phys. Rev. Lett. **99**, 220405 (2007).

[40]U. Schollwöck, "The density-matrix renormalization group in the age of matrix product states", Annals of Physics **326**, 96–192 (2011).

[41]K. A. Hallberg, "New trends in density matrix renormalization", Advances in Physics **55**, 477–526 (2006).

[42]F. Verstraete and J. I. Cirac, "Renormalization algorithms for Quantum-Many Body Systems in two and higher dimensions", eprint arXiv:cond-mat/0407066 (2004).

[43]F. Verstraete, D. Porras, and J. I. Cirac, "Density Matrix Renormalization Group and Periodic Boundary Conditions: A Quantum Information Perspective", Physical Review Letters **93**, 227205, 227205 (2004).

[44]Z. Fan and Q.-l. Jie, "Ordered magnetic phase in a frustrated spin-1/2 heisenberg antiferromagnetic stacked square lattice", Phys. Rev. B **89**, 054418 (2014).

[45]Q. Jie, "Approximating the ground state of fermion systems by multiple determinant states: matching pursuit approach", Phys. Rev. E **77**, 026705 (2008).

[46]L. Isaev, G. Ortiz, and J. Dukelsky, "Hierarchical mean-field approach to the $J1$-$J2$ heisenberg model on a square lattice", Phys. Rev. B **79**, 024409 (2009).

[47]Q. Si and E. Abrahams, "Strong Correlations and Magnetic Frustration in the High T_c Iron Pnictides", Physical Review Letters **101**, 076401, 076401 (2008).

[48]Q. Si and E. Abrahams, "Strong correlations and magnetic frustration in the high Tc iron pnictides", Phys. Rev. Lett. **101**, 076401 (2008).

[49]R. Melzi, S. Aldrovandi, F. Tedoldi, P. Carretta, P. Millet, and F. Mila, "Magnetic and thermodynamic properties of li2vosio4: a two-dimensional $s = 1/2$ frustrated antiferromagnet on a square lattice", Phys. Rev. B **64**, 024409 (2001).

[50]P. W. Anderson, "An approximate quantum theory of the antiferromagnetic ground state", Phys. Rev. **86**, 694–701 (1952).

[51]D. A. Huse, "Ground-state staggered magnetization of two-dimensional quantum heisenberg antiferromagnets", Phys. Rev. B **37**, 2380–2382 (1988).

[52]J. D. Reger and A. P. Young, "Monte carlo simulations of the spin-(1/2 heisenberg antiferromagnet on a square lattice", Phys. Rev. B **37**, 5978–5981 (1988).

[53]S. Liang, "Existence of néel order at T =0 in the spin-1/2 antiferromagnetic heisenberg model on a square lattice", Phys. Rev. B **42**, 6555–6560 (1990).

[54]H. J. Schulz and T. A. L. Ziman, "Finite-size scaling for the two-dimensional frustrated quantum heisenberg antiferromagnet", EPL (Europhysics Letters) **18**, 355 (1992).

[55]P. Chandra and B. Doucot, "Possible spin-liquid state at large s for the frustrated square heisenberg lattice", Phys. Rev. B **38**, 9335–9338 (1988).

[56]J. Oitmaa and Z. Weihong, "Series expansion for the $j1$-$j2$ heisenberg antiferromagnet on a square lattice", Phys. Rev. B **54**, 3022–3025 (1996).

[57]N. Read and S. Sachdev, "Valence-bond and spin-peierls ground states of low-dimensional quantum antiferromagnets", Phys. Rev. Lett. **62**, 1694–1697 (1989).

[58]V. Murg, F. Verstraete, and J. I. Cirac, "Exploring frustrated spin systems using projected entangled pair states", Phys. Rev. B **79**, 195119 (2009).

[59]L. Capriotti and S. Sorella, "Spontaneous plaquette dimerization in the $j1\Gamma21j2$ heisenberg model", Phys. Rev. Lett. **84**, 3173–3176 (2000).

[60]P. Anderson, "Resonating valence bonds: a new kind of insulator?", Materials Research Bulletin **8**, 153 –160 (1973).

[61]A. Kitaev, "Anyons in an exactly solved model and beyond", Annals of Physics **321**, 2–111 (2006).

[62]H.-D. Chen and Z. Nussinov, "Exact results of the Kitaev model on a hexagonal lattice: spin states, string and brane correlators, and anyonic excitations", Journal of Physics A Mathematical General **41**, 075001, 075001 (2008).

[63]M. Freedman, M. Larsen, and Z. Wang, "A modular functor which is universal for quantum computation", eprint arXiv:quant-ph/0001108 (2000).

[64]A. Y. Kitaev, "Fault-tolerant quantum computation by anyons", Annals of Physics **303**, 2–30 (2003).

[65]C. Nayak, S. H. Simon, A. Stern, M. Freedman, and S. Das Sarma, "Non-Abelian anyons and topological quantum computation", Reviews of Modern Physics **80**, 1083–1159 (2008).

[66]T. Einarsson, "Fractional statistics on a torus", Phys. Rev. Lett. **64**, 1995–1998 (1990).

[67]G. Jackeli and G. Khaliullin, "Mott insulators in the strong spin-orbit coupling limit: from heisenberg to a quantum compass and kitaev models", Phys. Rev. Lett. **102**, 017205 (2009).

[68]J. B. Fouet, P. Sindzingre, and C. Lhuillier, "An investigation of the quantum J $_1$ - J $_2$ - J $_3$ model on the honeycomb lattice", European Physical Journal B **20**, 241–254 (2001).

[69]G. Khaliullin, "Orbital Order and Fluctuations in Mott Insulators", Progress of Theoretical Physics Supplement **160**, 155–202 (2005).

[70]J. Oitmaa, "Phase diagram of the heisenberg-kitaev model at $t = 0$", Phys. Rev. B **92**, 020405 (2015).

[71]J. D. Reger, J. A. Riera, and A. P. Young, "Monte carlo simulations of the spin- 1 / 2 heisenberg antiferromagnet in two dimensions", Journal of Physics: Condensed Matter **1**, 1855 (1989).

List of Figures